HUNGRY BLACK HOLES - AGN FUELING AND CENTRAL ENGINES IN THE MILLIMETRE

by

Jacob Sean Elford

A THESIS SUBMITTED TO CARDIFF UNIVERSITY
FOR THE DEGREE OF DOCTOR OF PHILOSOPHY

SEPTEMBER 2024

Acknowledgements

This thesis would not of been possible without the funding from AIMLAC. I am very grateful to them for funding my PhD. I have used data from a number of different telescopes throughout this thesis and I am very grateful for the these facilities:

- Atacama Large Millimeter/submillimeter Array (ALMA)
- Multi-Unit Spectroscopic Explorer (MUSE)
- Chandra.

I am very grateful for the computing facilities at Cardiff University and to Richard Frewin for helping me solve any computing issues I had. I am extremely grateful to the computers PADFOOT and SERPENS who I have used extensively over my PhD. I finally need to thank following software I used throughout this thesis:

- Python, version 3.9 (packages: `gastimator`, `pymakeplots`, `stackarator`, `lts_linefit` Cappellari et al. (2013b),`numpy` Harris et al. (2020), `astropy` Astropy Collaboration et al. (2013, 2018, 2022), `matplotlib` Hunter (2007), `pandas` Wes McKinney (2010); pandas development team (2020), `scipy` Virtanen et al. (2020), `scikit-learn` Pedregosa et al. (2011)
- LaTeX
- CASA (McMullin et al., 2007)
- CARTA (Comrie et al., 2021)

Finally, I am very thankful to the WISDOM team, CARS team and all my co-authors for your help and very useful comments throughout my PhD.

Dedication

> *"It's only astrophysics no one cares."*
>
> -Tim Davis

The number of people who I need to thank could very easily be longer than this thesis. I am so incredibly grateful to so many people that have helped me to get to this point. If have neglected to include you in this dedication I can only apologise but please know that I am so thankful for the help that you have given me.

Firstly, I want to thank my two supervisors Tim Davis and Ilaria Ruffa. You have helped guide me through my PhD and have always been there to support me. You have taught me so much and given me so many great opportunities. I cannot thank you enough for your help over the years. I am so sorry for having to deal with my scatter brain and stupidity throughout my PhD.

I next want to thank Mum, Steve, Morgan, Alfie, Nanny Mona, Nanny, Granddad, Andy and the rest of my family who have always supported me through my studies. I am sorry I don't always stay in contact but I love you all so much and I am so thankful for your support.

I am incredibly grateful to have shared this PhD journey with so many amazing people who without I don't think I would of made it to the end. Thank you all so much for all the great times we have had and the great memories. I want to say that you are all very dear to me and I love you all. I hope we keep in contact. Thank you to Andy Cook for being my twin and sharing the same brain cell. You are one of my best friends and you have supported me so much. Thank you to Helena Faustino Vieira for helping to improve my plots and for making me laugh. You are an amazing friend and many of the plots in this thesis would look horrendous without you. Thank you to Eva Duran Camacho for being such a fun person and always being up for impulsively buying things with me. You are one of my closest friends and you have made my PhD experience so much more fun. Thank you to Terri Pearce for sharing my love of country music and pub quizzes. You are one of my favourite people in the world and I can't imagine going through my PhD without you as my friend. Thank you to Michael Norman for all the smaaaalll gin shots we have had and for the walks home after nights out. You are such a supportive friend and your hypothetical questions always make me laugh. Thank you to Luke Booth and Gerywn Jones for being amazing flat mates and for always being up to chat about F1. Living with you two has been an amazing two years. I also need to thank the legendary toilet chair that was in our flat for 2 years. Thank you to Lottie Braithwaite for sharing my love of baked beans and always being up for a chat. Thank you to Hidde Jense for all the drunken nights and board games. Thank you to Holly Davies for being so kind and for being an amazing DM

in our DnD campaign which I look forward to every week. Thank you to Roger Wesson for being a font of knowledge about Chile and a great quiz master. Thank you to Carys Evans and George Brown (the honorary PhD student) for being some of the kindest people in the world. Thank you to Hannah Ambrose for always suggesting shots when we are at the pub. Thank you to Meryl Kinnear for the great parties. Thank you to Lewis Prole for all the great nights out. Thank you Patrick Ashworth for all the funny stories you have. Thank you to Marc Vina Betran for always being up for talking about football. I also need to thank a number of other people who I have meet during my time in Cardiff. These include Matt Lyons, Vassilis Skliris, Mason Hill, Max Baker, Ffion James, Sam Gavin-Pitt, Jordan Barber, Matt Cusack, Michael Anderson, Gayathri Eknath, Phil Relton, Jaspa Stritt, Patrick Sutton, Sander Vermuelen, Ali James, Bradley Ward, Rhiannon Silva, Vani Lanka, Gethin Robson, Mattia Negrello, Benjamin Beringue, Andy Rigby, Freeke van de Voort, Ana Duarte Cabral, Nico Peretto, Ian Harrison, Serena Giardiello, Andy Hannington, Ant Whitworth, Matt Smith, Paul Clark, Sarah Ragan, Felix Priestly, Steve Eales, Nikki Zabel, James Dawson, Eve North, Matt Bates, Eleonora Parrag, Zoltan Sztranyovszky, Penny Kolitsidou and Matt Walker. The department in Cardiff has been so welcoming with so many friendly people. I will miss coffee in the rest frame Thursday cake, Friday pub and all the different social events.

I next want to the office I was in for the majority of my PhD N/3.27. Even though you are leaky, damp and should probably be abandoned I have loved working here throughout my PhD. I also need to thank Andy, Helena and Eva, the amazing people I shared N/3.27 with. Sharing an office with you made coming into work everyday so much more enjoyable.

I next want to thank Helena, Andy and Roger again for the many games of Shithead and Carcassone. I think we are now up to 164[*] games of Shithead so far and I can't believe I've lost a third of those. I always look forward to playing these games with you. Thank you so much for the many games. You guys mean so much to me and I am really going to miss you.

I next want to thank Terri, Eva and Michael again for my amazing birthday this year. Going to Wycombe to watch the football and going out to Trilogy with you guys was the best birthday I've ever had. It was such a fun weekend and I am so grateful to you. I will treasure you guys forever and I am going to miss you so much.

I next want to thank my friends from outside the PhD who have always been there for me. Thank you to Josh Bright for being my best friend for so many. I am so grateful for your help and support over the years. Thank you to Evan Goodman for always being up for a chat and always being there for me. Thank you to Peter Kirk, Andrew Johns and Becca Watkins for all the great holidays and drunken BBQs. Thank you to Michael Kenna-Allison, Laura Iacconi, Gui Brando, Chris Pattison, Natalie Hogg, Mike Wang and Matthew Hull for inspiring me to do a PhD. Thank you to Gabriel and Jessica Semple for your kindness and support over the years. Thank you to Alexander Jones for the great nights out in Portsmouth and Cardiff.

This thesis could not of been completed without all of this help. I am so incredibly grateful.

---

[*] Likely more than that now

Abstract

The energetic output from active galactic nuclei (AGN) may have a noticeable impact on the different phases of the interstellar medium (ISM) that surrounds it. In this thesis I use high resolution multi-wavelength data of nearby galaxies to understand this connection. I utilise data from the mm-Wave Interferometric Survey of Dark Object Masses (WISDOM) project and the Close AGN Reference Survey (CARS) to directly study the connection between the AGN and the ISM. I find that the amount of cold molecular gas surrounding AGN does not correlate with the current level of AGN activity, which conflicts with previous results. This could indicate that AGN fuelling is not a ubiquitous process. However, I also find that the AGN can impact both the high density molecular gas that surrounds it by heating or destroying it and the lower density gas in the warm ionized medium (WIM). Understanding the underlying accretion mechanism in AGN is also key to understanding the interplay between AGN and their host galaxies. In this thesis I present the newly discovered *millimetre fundamental plane of black hole accretion* which appears to be followed by both high and low accretion rate sources as well as stellar mass black holes in X-ray binaries (XRBs). I find that radiatively inefficient processes such as advection dominated accretion flows (ADAFs) or compact jets may explain this fundamental plane which could have important implication for the underlying accretion process and structure of AGN. In summary, the work presented in this thesis will aide in the study of AGN and how they connect with their host galaxies. This work will also emphasise the need for further multi-wavelength observations of AGN to fully understand the fuelling/feedback picture and the underlying accretion mechanism in these objects.

Publications

FIRST AUTHOR PUBLICATIONS

Elford J.S., et al. 2024, MNRAS, 528, 319

Elford J.S., et al. Submitted (The Close AGN Reference Survey (CARS): A comparison between sub-mm and optical AGN diagnostic diagrams)

Elford J.S., et al. Submitted (The millimetre fundamental plane of black hole accretion for stellar mass black holes)

CO-FIRST AUTHOR PUBLICATIONS

Ruffa I., Davis T. A., *Elford J.S.*, et al. 2023, MNRAS, 528, L76

CO-AUTHOR PUBLICATIONS

Davis T. A., et al. 2022, MNRAS, 512, 1522

Lu A., et al. 2022, MNRAS, 514, 5035

Ruffa I., et al. 2023, MNRAS, 522, 6170

Williams T. G., et al. 2023, MNRAS, 525, 4270

Liang F., et al. 2024, MNRAS, 527, 9343

Zhang H., et al. 2024, MNRAS, 530, 3240

Lu A., et al. 2024, MNRAS, 531, 3888

García-Burillo S., et al. 2024, A&A Accepted

STATEMENT OF AUTHORSHIP

Chapter 4 of this thesis is based on the following published paper: Ruffa I., Davis T. A., *Elford J. S.*, et al (2023) *A fundamental plane of black hole accretion at millimetre wavelengths*, MNRAS, 528, L76.

This was a shared first author paper between IR, TD and JE. JE performed the initially data collection and analysis that formed the ground work of this paper. IR and TD performed further analysis for this paper. The results were interpreted by IR, TD and JE. IR lead the writing of the paper, with input from TD and JE.

Contents

List of Tables

List of Figures

“All we have to decide is what to do with the time that is given to us.”

CHAPTER 1

Introduction

*““I used to do strokes underwater like a f*cking mermaid"*

-Terri Pearce

Our understanding of galaxy evolution was revolutionised when Schmidt (1963) discovered that the discrete radio source 3C 273 was extragalactic instead of being a galactic star. These discrete radio sources were termed quasi-stellar radio sources (quasar) and the field of active galactic radio (AGN) research was born. Studying how AGN interact with their host galaxies is key to understanding galaxy evolution. In this thesis I include my own contribution to the study of AGN to date, investigating how they are fuelled, and how the radiation from the central engine at different wavelengths links to their properties and structure.

1.1 SCIENTIFIC BACKGROUND

1.1.1 GALAXY FORMATION AND EVOLUTION

Galaxies are the fundamental building blocks of the Universe and by studying how these vast collections of gas and stars form and evolve is key to understanding it. Eggen et al. (1962) initially proposed that galaxies form through monolithic collapse where primordial gas in the early Universe formed all parts of a galaxy at the same time. However, the discovery that different parts of galaxies have very different ages appears to rule out this model.

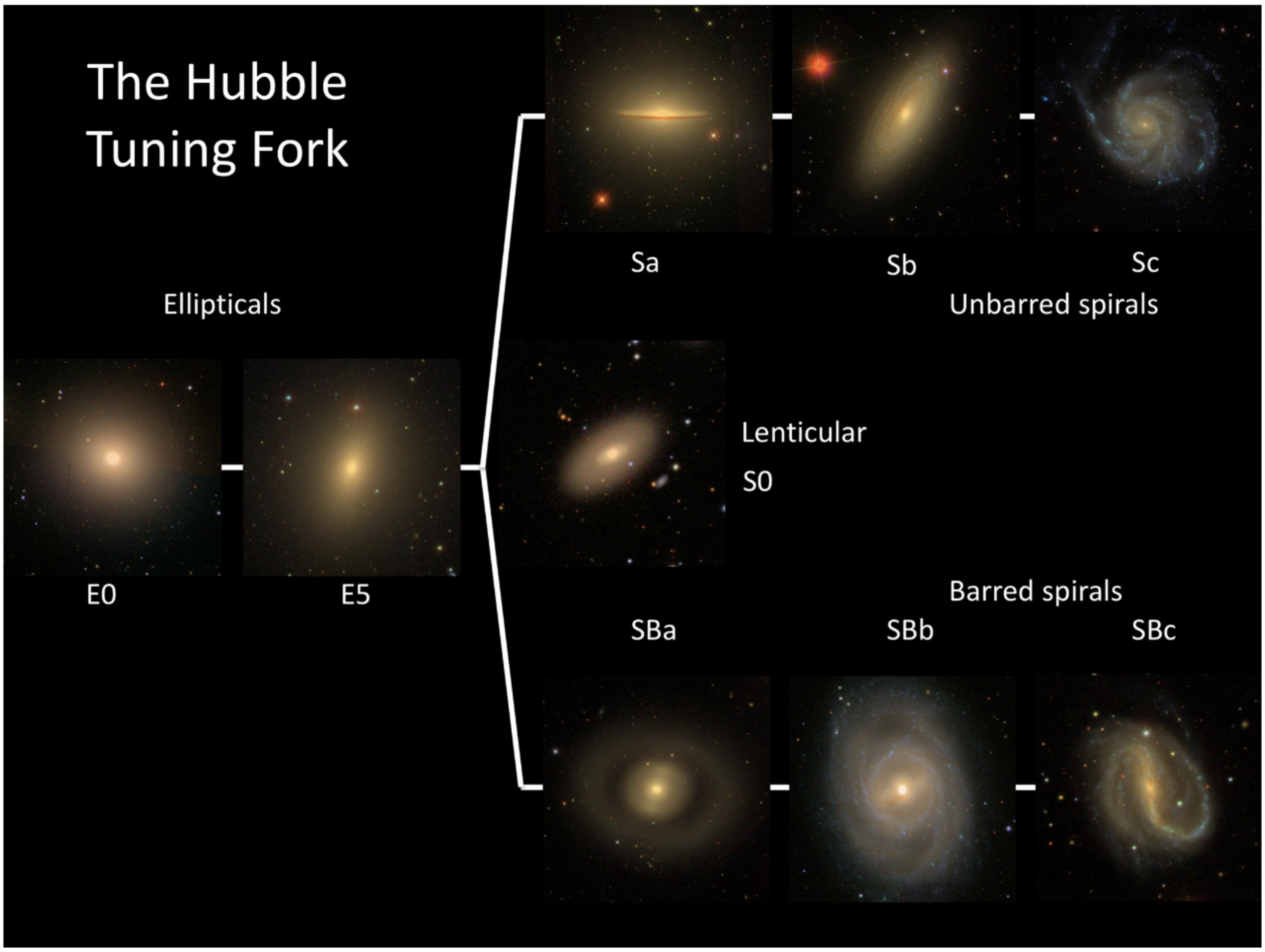

Figure 1.1: The Hubble tuning fork with images taken from the Sloan Digital Sky Survey (York et al., 2000). Taken from Masters et al. (2019)

Our current best theory of the Universe is one with cold dark matter and a non-zero cosmological constant (ΛCDM). In this theory galaxies form through hierarchical mergers. Overdensities in the early Universe are able to collapse to form dark matter halos which serve as the site of galaxy formation. These halos then evolve in a two-stage process as laid out by White & Rees (1978) where these small halos merge to form larger systems whilst also accreting gas from filaments in the cosmic web producing the galaxies we see today.

An early attempt to classify galaxy morphology was proposed by Hubble (1926). In this scheme, known as the Hubble tuning fork, the classification is done by the optical shape or morphology of the galaxy. The galaxies are separated by the size of the central bulge with respect to the stellar disk and whether spiral arms and bars are present. There are *ellipticals* (E) which have no obvious stellar disk and have a smooth light distribution. Then there are *lenticulars* (S0) which have a bright central bulge and an extended stellar disk but do not have any visible spiral structure. Galaxies with spiral arms are called *spiral* galaxies and are sub-classified into un-barred spiral galaxies (S) and barred spiral galaxies (Sb). Galaxies that do not have a regular structure and do not fit in the Hubble classification are called *irregulars*. It was originally believed that this was an evolutionary sequence where ellipticals galaxies collapse to form spiral galaxies. This naming convention has stuck with ellipticals and lenticulars being known as *early-type galaxies* (ETG) and spirals and irregulars being known as *late-type galaxies* (LTG). A example of Hubble's tuning fork is shown in Figure 1.1.

It is now believed that this evolutionary sequence is incorrect with ETGs and LTGs being believed to evolve in very different ways. ETGs are believed to have experienced multiple mergers with the impact of these mergers still being visible (e.g. Toomre, 1977). On the other hand, spiral galaxies have had a less violent evolution which is being driven by bars and spiral structures (e.g. Kormendy, 1979; Kormendy & Kennicutt, 2004). In the hierarchical merging picture it is now believed that LTGs galaxies merge and become ETGs (e.g. Steinmetz & Navarro, 2002) though ETGs could also form through a burst of star formation at high redshift and then passively evolve to the present day (e.g. Partridge & Peebles, 1967; Larson, 1975).

The colour of galaxy is a useful tool when trying to understand its evolution. Younger stellar populations tend to be bluer in colour as more massive stars are blue and have not yet had time to evolve to red giants or to have died. Blue galaxies thus indicate that there is still ongoing star formation. On the the other hand, older stellar populations tend to be redder as they contain less massive stars, and the lower mass stars still present tend to be red in colour. Red galaxies indicate that there is little ongoing star formation taking place. It has been observed that ETGs are redder than LTGs (e.g. Baum, 1959; Strateva et al., 2001; Bell et al., 2004) which suggests that something has caused ETGs to stop forming stars either through morphological quenching (e.g. Martig et al., 2009), having less gas that is able to collapse to form stars (e.g. Serra et al., 2012), being impacted by their environment (Gunn & Gott, 1972) or by the influence of active galactic nuclei (AGN; e.g. Fabian, 2012).

ETGs have been found to be more prevalent in high density environments (i.e. galaxy clusters e.g. Gunn & Gott, 1972; Oemler, 1974; Dressler, 1980; Haynes et al., 1984; Djorgovski & Davis, 1987; Kauffmann et al., 2004; Paulino-Afonso et al., 2019) which may indicate the environment of galaxy may be important in the evolution of LTGs to ETGs. It has been predicted that galaxy being in or entering into a cluster will heavily impact the gas within the galaxy (Gunn & Gott, 1972). It has been found that effects such as ram pressure stripping and galaxy-galaxy harassment can have a significant impact on the evolution of galaxies (see Boselli et al., 2022, for a review). These processes can remove gas from galaxies reducing star formation, however they can also overpressure the gas in these systems, leading to an increase in star formation (e.g. Moore et al., 1996; Zabel et al., 2019). However, in the long term this would lead to galaxy being quenched as the gas is being used up faster.

Finally, secular processes seem to be important to the evolution of galaxies. Secular processes tend to be slow and are mainly driven by structures in the galaxy (e.g. bars and spirals arms, Kormendy & Kennicutt, 2004). These structures can causes resonances and instabilities which can lead to gas inflows and the disruption of stellar orbits by transferring angular momentum. Bars have the ability to move gas inwards which may fuel bursts of star formation and AGN activity (e.g. Pfenniger & Norman, 1990; Combes, 2001; Kormendy & Kennicutt, 2004). These secular processes may then reduce the available fuel for star formation in the disk of the galaxies.

1.1.2 STAR FORMATION IN GALAXIES

Star formation is believed to occur within clouds of cold molecular gas (e.g. Hoyle, 1953; Dieter & Goss, 1966; Spitzer, 1968; Faustino Vieira et al., 2024) in the interstellar medium (ISM; see Section 1.2). These clouds will collapse under gravity to form stars. If effects such as rotation, turbulence, magnetic fields or external pressure are ignored and only gravitation and thermodynamics are considered the mass of a cloud needed for it to collapse under gravity, known as the Jeans Mass (Jeans, 1902), is defined as

$$M_{\mathrm{J}} \simeq \left(\frac{5kT}{G\mu m_{\mathrm{H}}}\right)^{3/2}\left(\frac{3}{4\pi\rho_0}\right)^{1/2} \tag{1.1}$$

where k is the Boltzmann constant, T is the temperature of the cloud, G is the gravitational constant, μ is the mean molecular weight, m_{H} is the mass of hydrogen and ρ_0 is the density of the cloud. If it is assumed that the cloud is in free-fall during its collapse and there are no other forces to counteract the collapse the free-fall time (the time it takes for particles to fall from the edge of the cloud to the centre) can be defined as

$$t_{\mathrm{ff}} = \left(\frac{3\pi}{32}\frac{1}{G\rho_0}\right)^{1/2}. \tag{1.2}$$

In the simplest terms the rate that a galaxy is forming stars (i.e. the star formation rate; SFR) is

$$\mathrm{SFR} = \frac{M_{\mathrm{gas}}}{t_{\mathrm{dep}}} \tag{1.3}$$

where M_{gas} is the mass of the star forming gas reservoir and t_{dep} is the depletion time (i.e. the time it would take for the gas reservoir to be used up by star formation).

To understand the star formation process in galaxies a useful parameter is the star formation rate (SFR) surface density, Σ_{SFR}, which tells us the rate that stars are being formed in a given area. It is found that Σ_{SFR} correlates with the gas surface density Σ_{gas} in a power law of the form

$$\Sigma_{\mathrm{SFR}} \propto \Sigma_{\mathrm{gas}}^{N} \tag{1.4}$$

which is known as the Kennicutt-Schmidt (KS) relation (Schmidt, 1959; Kennicutt, 1989) where N has a value of around 1.4. This relation suggests that the more gas a galaxy has the more star formation should occur. Another useful metric for understanding star formation in galaxies is the star formation efficiency (SFE). The star formation efficiency is defined as

$$\mathrm{SFE} = \frac{\Sigma_{\mathrm{SFR}}}{\Sigma_{\mathrm{gas}}} = \frac{1}{t_{\mathrm{dep}}}. \tag{1.5}$$

By studying what can impact the SFR and what can cause variations in the SFE is key to understanding galaxy evolution.

1.1.3 THE ROLE OF ACTIVE GALACTIC NUCLEI IN GALAXY EVOLUTION

Studies of how the SFR of objects varies with stellar mass (M_*) in the local Universe find a tight relation between the SFR and M_*. This relation has been termed the galaxy main sequence (MS). The MS has been observed to be linear up to a critical mass and then flattens out at higher masses. This tight relation implies that higher mass galaxies have more gas mass and can sustain higher levels of star formation with the scatter in this relation showing the importance of galaxy-galaxy variations. However, there are a large population of galaxies that exist significantly below the MS. These galaxies are forming fewer stars for their mass compared to galaxies of the same mass that fall on the MS. These two populations of galaxies can be seen in Figure 1.2 where the SFR-M_* relation can be seen for the galaxies in the xCOLD GASS survey (Saintonge et al., 2011a,b, 2017) and Sloan Digital Sky Survey (SDSS) sample at $0.01 < z < 0.05$. These galaxies, which are described as being quenched, appear to have had their star formation suppressed and thus fall off the MS. A bimodality, which can be seen in Figure 1.3, is seen in the colours of galaxies with those that follow the MS being blue in colour due to their significant ongoing star formation. On the other hand, quenched galaxies are red in colour due to their low level of star formation. A small fraction of galaxies exist between these two extremes in a region known as the green-valley.

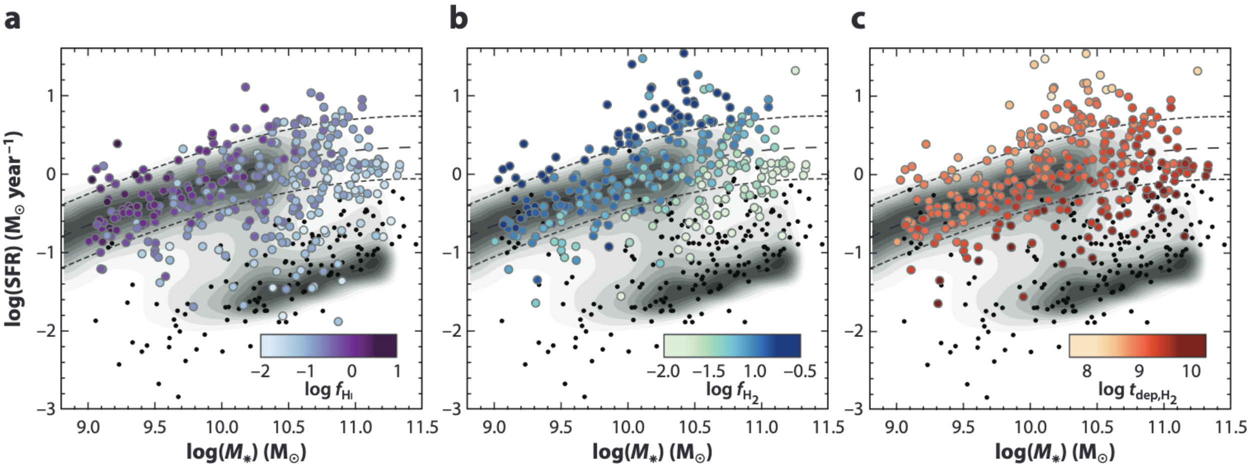

Figure 1.2: The SFR-M_* relation with the point coloured based on the H I fraction in (a), the H_2 fraction in (b) and the depletion time in (c) for the xCOLD GASS sample. The contours are from the SDSS sample at $0.01 < z < 0.05$. The dashed line shows the main sequence (MS) whilst the dotted lines are the 0.4 dex scatter around the main MS. Taken from Saintonge & Catinella (2022)

A leading theory on how these galaxies end up quenched is through feedback from AGN. Other methods that may lead to galaxy quenching are discussed in Section 1.1.1. AGN can impact star formation through winds and jet which can directly remove gas or by injecting energy and turbulence into the star forming gas reservoir which stops the cooling and collapse of this gas into stars. It is also found that AGN (specifically radiative mode AGN; see Section 1.5.3) tend to populate the green-valley between star forming blue galaxies and quenched red galaxies. On the other hand, several studies have shown that the cold gas reservoir of galaxies is unaffected by the AGN they are hosting. Studies have found that both the molecular gas fraction and depletion times are similar in active and in-active galaxies in the same region of SFR-M_* relation.(Saintonge et al., 2017; Rosario et al., 2018; Koss et al., 2021). With similar results being found in HI studies (Ho et al., 2008; Fabello et al., 2011; Ellison et al., 2019). There is growing evidence that AGN quench galaxies by heating up the halo through kinetic mode feedback (see Section 1.5.3) (e.g. Bower et al., 2006; Croton et al., 2006; Somerville et al., 2008, 2012; Henriques et al., 2015; Peng et al., 2015). This stops the accretion of new gas, which replenishes the star forming gas reservoir, leading to massive galaxies falling off the MS whilst also stopping already quenched galaxies from restarting the star formation process (Best et al., 2005).

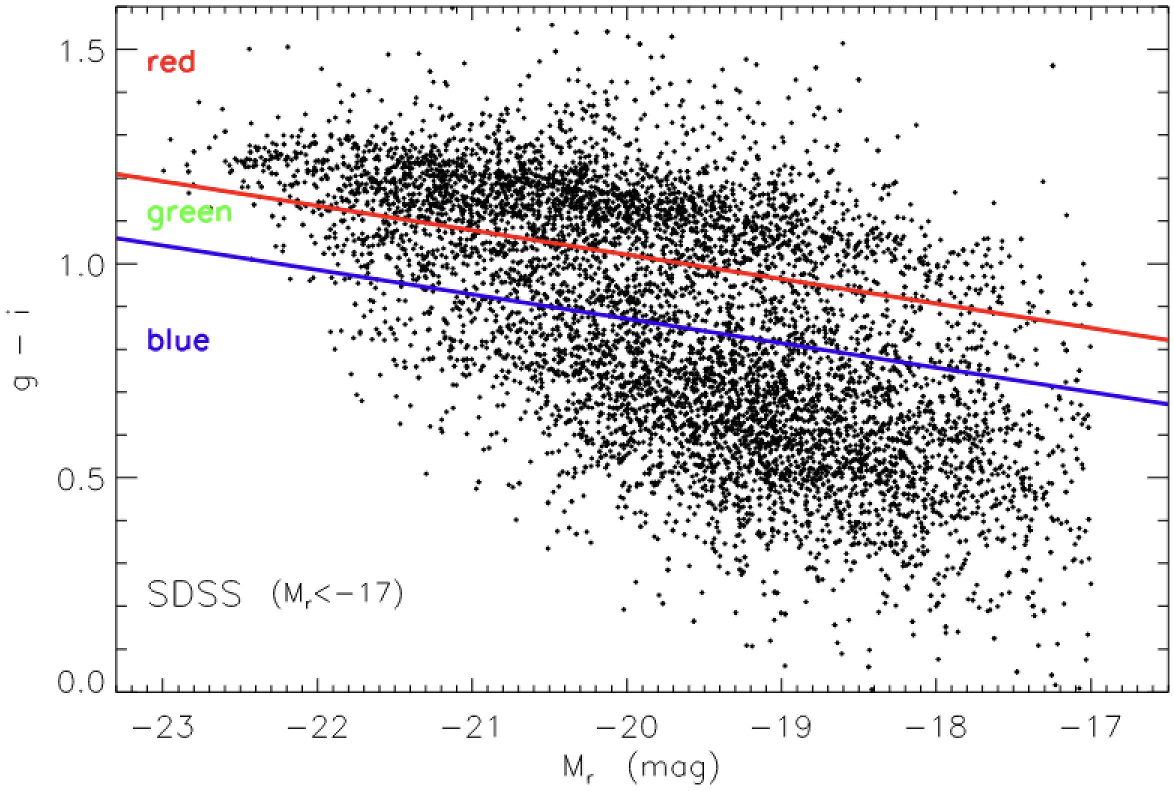

Figure 1.3: Colour-magnitude diagram of the SDSS sample. The lines represent the cuts between the red, green and blue galaxies in the sample. Taken from Papastergis et al. (2013)

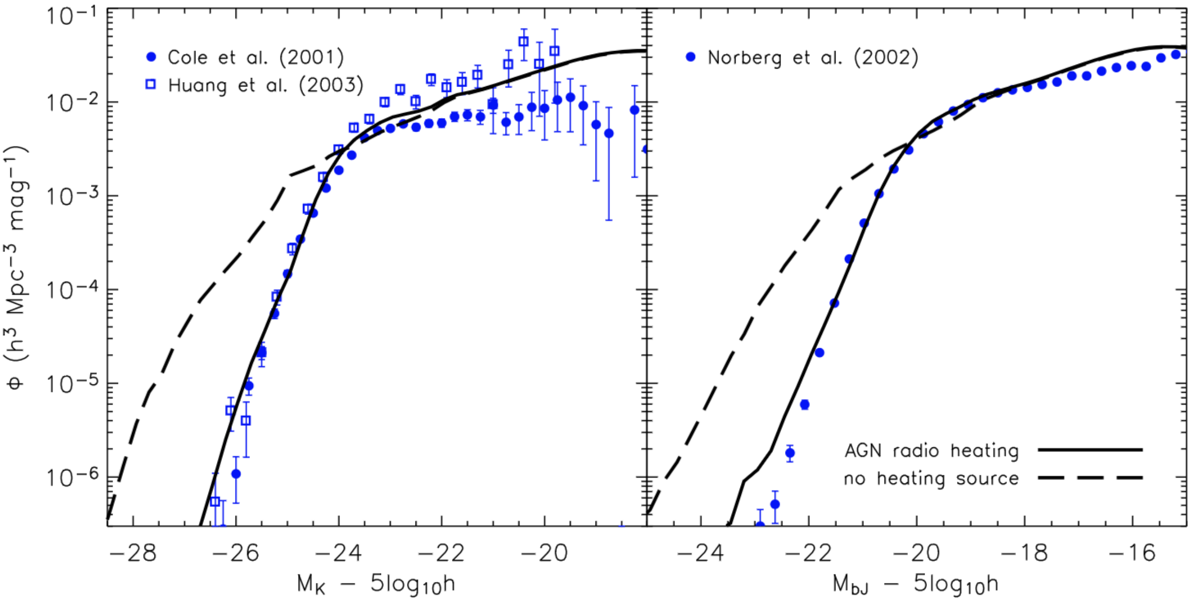

Figure 1.4: Local luminosity function for with the observations being the blue points in the K-band (left panel) and the J-band (right panel). The model with AGN feedback is the solid line and the model without AGN feedback is the dashed line. Taken from Croton et al. (2006).

Models and simulations of galaxy evolution also require AGN feedback to explain the observed properties of massive ($M_* > 10^{10.5}\,\mathrm{M}_\odot$) galaxies (Kauffmann & Haehnelt, 2000; Di Matteo et al., 2005). Semi-analytical models are used to made predictions of observed galaxy properties. In these models the dark matter halo mass function is transformed into a galaxy luminosity function assuming ΛCDM cosmology (see reviews by Baugh, 2006; Benson, 2010). It is found in models with no AGN feedback present the observed and the predicted number of high mass (high luminosity) galaxies do not match where there is steeper cut off at high masses than is predicted by the models with no AGN feedback. AGN feedback is needed to stop galaxies from growing in the most massive haloes and to reproduce the sharp drop off at the high mass (high luminosity) end of the luminosity function. The comparison between the local galaxy luminosity function and those predicted from models is show in Figure 1.4.

Finally, AGN may be important in solving the 'cooling flow problem' (see review by Fabian, 1994). The cooling flow problem is why the most massive and central galaxies in clusters (Brightest Cluster Galaxies, BCGs), which should have large supplies of gas that is being cooled from the surrounding haloes, appear less blue then expected. Clusters of galaxies have haloes of hot ($10^7 - 10^8\,\mathrm{K}$) gas which is cooling by emission of Bremsstrahlung radiation and line emission from high ionised species which allows the gas to cool, contract and inflow onto the central galaxy with the cooling rates that have been observed being $10 - 1000\,\mathrm{M_\odot\,yr^{-1}}$ (e.g. Edge, 2001; Edge & Frayer, 2003). The mechanical feedback from AGN has been shown as a potential solution as to why these BCGs seems to be forming stars at a lower rate then expected from the gas supply available to them. AGN can produce radiative winds and jets that can heat the gas at large scales which prevents it from cooling (e.g. McNamara et al., 2005; McNamara & Nulsen, 2007; Clarke et al., 2009; McNamara & Nulsen, 2012).

It is clear that AGN play an important role in the evolution of galaxies, however, the exact processes in which the AGN can impact their host galaxies and the scales at which AGN can impact their host galaxy is yet to be fully understood.

1.2 PHASES OF THE INTERSTELLAR MEDIUM

The interstellar medium (ISM) is made up of gas and dust which goes on to form stars and planets whilst also being the potential fuel for AGN. To fully understand how AGN and the host galaxy interacts it is important to understand the different phases of the ISM. In the following I will cover each phase of the ISM and what traces each phase.

1.2.1 COLD MOLECULAR MEDIUM

The cold molecular medium of galaxies is where star formation is expected to occur (Schmidt, 1959; Kennicutt, 1998). The cold molecular medium (CMM) has a volume filling factor <1% of the Milky Way, a temperature in the range of 10-50 K and densities of $10^3 - 10^7\,\mathrm{cm^{-3}}$. The most abundant molecule in this phase is molecular hydrogen, $\mathrm{H_2}$, however $\mathrm{H_2}$ cannot be observed in the cold conditions of the CMM as it does not have a permanent dipole moment and the temperatures are too low to excite quadrupole emission. Instead to trace the CMM we use the second most abundant molecule carbon monoxide (CO) which has easily observable rotational transitions in the millimetre regime. The CO(1-0) transition has a critical density of ($\approx 10^3\mathrm{cm^{-3}}$) and so is thought to be a good tracer of the total molecular gas reservoir. However, to convert the observed mass of CO to the mass of the total molecular reservoir a CO-to-$\mathrm{H_2}$ conversion factor (X_{CO}) is needed. The value of X_{CO} seems to vary between different galaxies and appears to be dependent on the metallicity and the strength of the UV radiation field (Boselli et al., 2002; Leroy et al., 2011). The value of X_{CO} may also vary within galaxies (e.g. Sandstrom et al., 2013). Other tracers of the CMM include HCN, HCO^+ and CS which trace the denser molecular gas component as they have a critical density of $> 10^4 \mathrm{cm}^{-3}$.

1.2.2 COLD NEUTRAL MEDIUM

The cold neutral medium (CNM) is made up mostly of hydrogen atoms (H I). It has a filling factor of 2-4%, a temperature of $\sim 100\,\mathrm{K}$ and a density of $\sim 20\,\mathrm{cm}^{-3}$ (Wolfire et al., 2003). It is believed that the CNM is distributed in filaments and sheets but despite only taken a small fraction of the volume of the ISM it makes up a third of the mass of the ISM. The CNM is mostly traced by the absorption lines of H I and [C II] emission lines.

1.2.3 WARM NEUTRAL MEDIUM

The warm neutral medium (WNM) is also made up of mostly hydrogen atoms (H I). It has a filling factor of $\sim 30\%$, a temperature of $\sim 6000\,\mathrm{K}$, and a density of $\sim 0.3\,\mathrm{cm}^{-3}$ (Wolfire et al., 2003). The WNM exists in the region between the H II region and the molecular clouds. The WNM is mostly traced by the emission from H I.

1.2.4 WARM IONIZED MEDIUM

The warm ionized medium (WIM) is primarily made up of ionized hydrogen (H II) and is believed to be photoionized by the UV photons from hot objects (such as (p)AGB, white dwarfs, OB stars or AGN) or shocks. The WIM has a filling factor of $\sim 15\%$, a temperature of $\sim 8000\,\mathrm{K}$ and a density of $\sim 0.3 \mathrm{cm}^{-3}$ (Reynolds, 1984). The WIM can be traced using the Balmer emission lines of hydrogen. H II regions are regions of the warm ionized medium where hydrogen has been ionized by a central star. H II regions can be traced by Hα emission.

1.2.5 HOT IONIZED MEDIUM

The hot ionized medium (HIM) is also primarily made up of ionized hydrogen and is believed to be shocked heated by supernova and shocks. The HIM has a large filling factor (70-80%), a temperature of $\sim 10^6\,\mathrm{K}$ and a low density ($\sim 10^{-3}\,\mathrm{cm}^{-3}$) (McKee & Ostriker, 1977). The HIM can be traced by the absorption features of ions such as O VI in the spectra of background stars whilst the hottest parts of the HIM can produce soft X-ray emission.

1.2.6 INTERSTELLAR DUST

Interstellar dust in found in the CMM, CNM, WNM and WIM phases of the ISM. Dust grains in the ISM absorb ultraviolet light emitted by stars and re-emit it at infrared wavelengths. If the dust is assumed to be optically thin then dust is expected to emit as a modified black body (MBB) which takes the form

$$I_\nu = \frac{\kappa_\nu M}{D^2} B_\nu(T) \tag{1.6}$$

where M is the dust mass, D is the distance to the source, $B_\nu(T)$ is the Planck function

$$B_\nu(T) = \frac{2h\nu^3}{c^2} \frac{1}{e^{\frac{h\nu}{kT}} - 1} \tag{1.7}$$

where T is the temperature, k is the Boltzmann constant, h is Planck's constant and c is the speed of light. Finally κ_ν is mass-opacity coefficient as is defined as

$$\kappa_\nu = \kappa_0 \left(\frac{\nu}{\nu_0}\right)^\beta \tag{1.8}$$

where κ_0 is the value of κ_ν at some reference frequency, ν_0, and β is the dust emissivity index.

Dust can be a useful method of tracing the entire ISM gas mass (e.g. Eales et al., 2012). By fitting the MBB of the dust emission the dust mass surface density ($\Sigma_{\rm dust}$) can be calculated which can then be converted to an ISM gas mass surface density ($\Sigma_{\rm gas}$) using

$$\Sigma_{\rm gas} = \Sigma_{\rm dust} \times {\rm GDR} \tag{1.9}$$

where GDR is the gas-to-dust ratio. Typically a Milky Way value of $\sim\ 100$ is assumed (Bohlin et al., 1978; Hildebrand, 1983). Though for external galaxies the GDR has been shown to vary radially (e.g. Muñoz-Mateos et al., 2009; Smith et al., 2012), with gas density (e.g. Roman-Duval et al., 2017; Clark et al., 2023) and with metallicity (e.g. Rémy-Ruyer et al., 2014; Roman-Duval et al., 2022).

1.3 AN INTRODUCTION TO AGN

It is believed that accretion onto supermassive black holes (SMBHs) gives rise to the emission from the centres of a fraction of galaxies that cannot be attributed to stellar activity.

We term these objects active galactic nuclei (AGN). The efficiency of the accretion on a SMBH is often described by its Eddington ratio.

The Eddington ratio is defined as

$$\lambda_{\mathrm{Edd}} = \frac{L_{\mathrm{bol}}}{L_{\mathrm{Edd}}} \tag{1.10}$$

where L_{bol} is the AGN bolometric luminosity and $L_{\mathrm{\ Edd}}$ is the Eddington luminosity. The AGN bolometric luminosity depends on the accretion rate onto the SMBH as can be defined as

$$L_{\mathrm{bol}} = \dot{M}_{\mathrm{SMBH}} \epsilon c^2 \tag{1.11}$$

where $\dot{M}_{\mathrm{SMBH}}$ is the accretion rate onto the SMBH, ϵ is the mass-energy conversion factor (typically assumed to be 0.1 though this may depend on properties such as the spin of the SMBH) and c is the speed of light. The Eddington luminosity is defined as

$$L_{\mathrm{Edd}} = \frac{4\pi G M_{\mathrm{SMBH}} m_{\mathrm{p}} c}{\sigma_{\mathrm{T}}} \tag{1.12}$$

where G is the the gravitational constant, m_{p} is the proton mass and σ_{T} is the Thompson cross section of the electron. The Eddington luminosity can be simplified to

$$L_{\mathrm{Edd}} = 1.26 \times 10^{38} M_{\mathrm{SMBH}}\,\mathrm{erg\,s^{-1}}. \tag{1.13}$$

In general AGN contain several if not all of the following components (a cartoon of an AGN containing these components is shown in Figure 1.5):

- An actively accreting SMBH
- An optically thick geometrically thin accretion disk or a optically thin geometrically thick advection dominated accretion flow in low accretion rate sources.
- A region of high density, dust free clouds at a distance of 0.01-1pc from the SMBH known as the broad-line region (BLR).
- A dusty torus structure at a distance of 0.1-10pc from the SMBH surrounding the SMBH, accretion disk and BLR.
- A region of low density ionized gas that can exist from just outside the torus to thousands of parsec along the opening of the torus known as the narrow-line region (NLR).
- A collimated outflow of non-thermal plasma know as a radio jet.

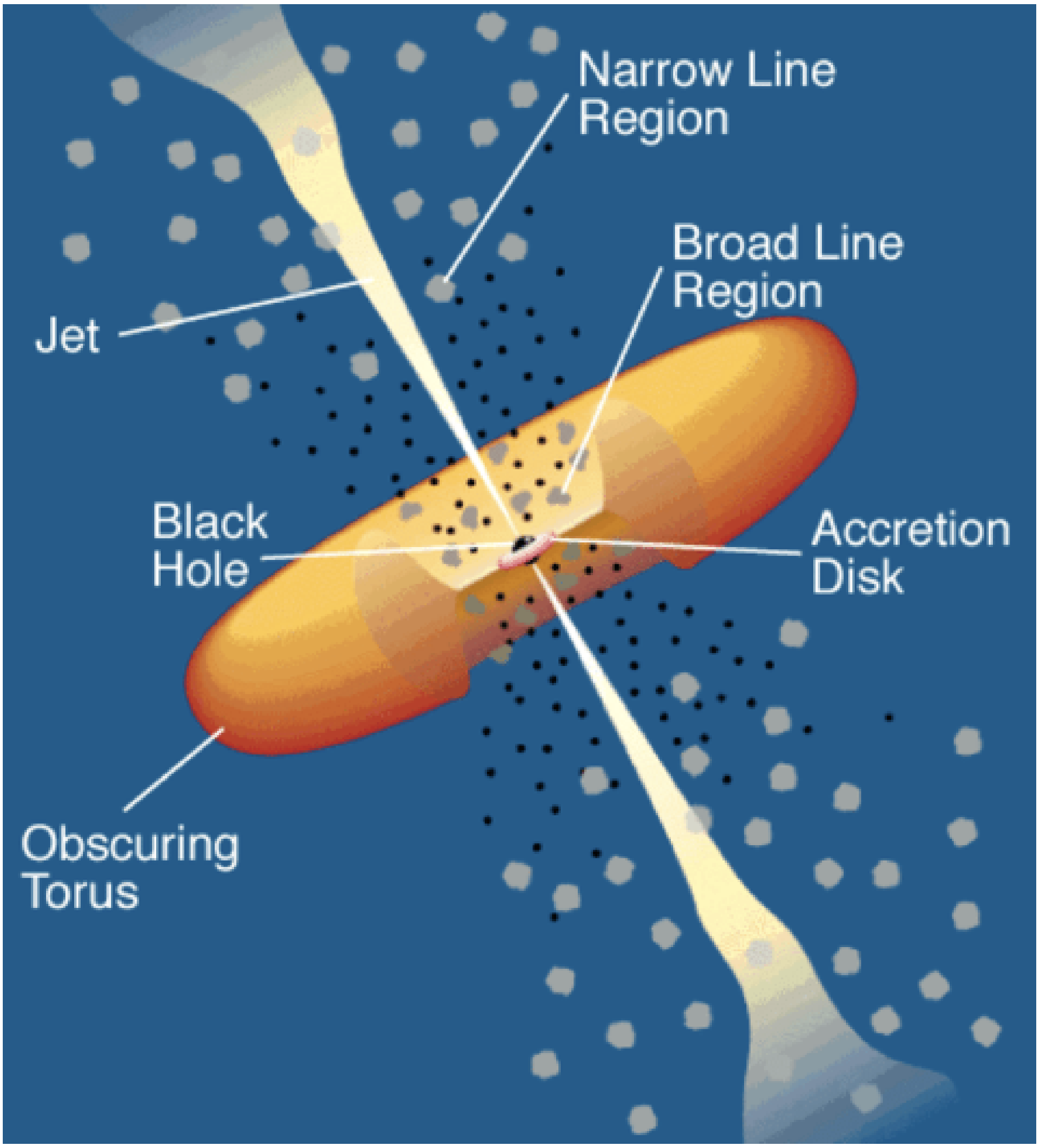

Figure 1.5: A cartoon of an AGN showing its components. Taken from Prandini & Ghisellini (2022).

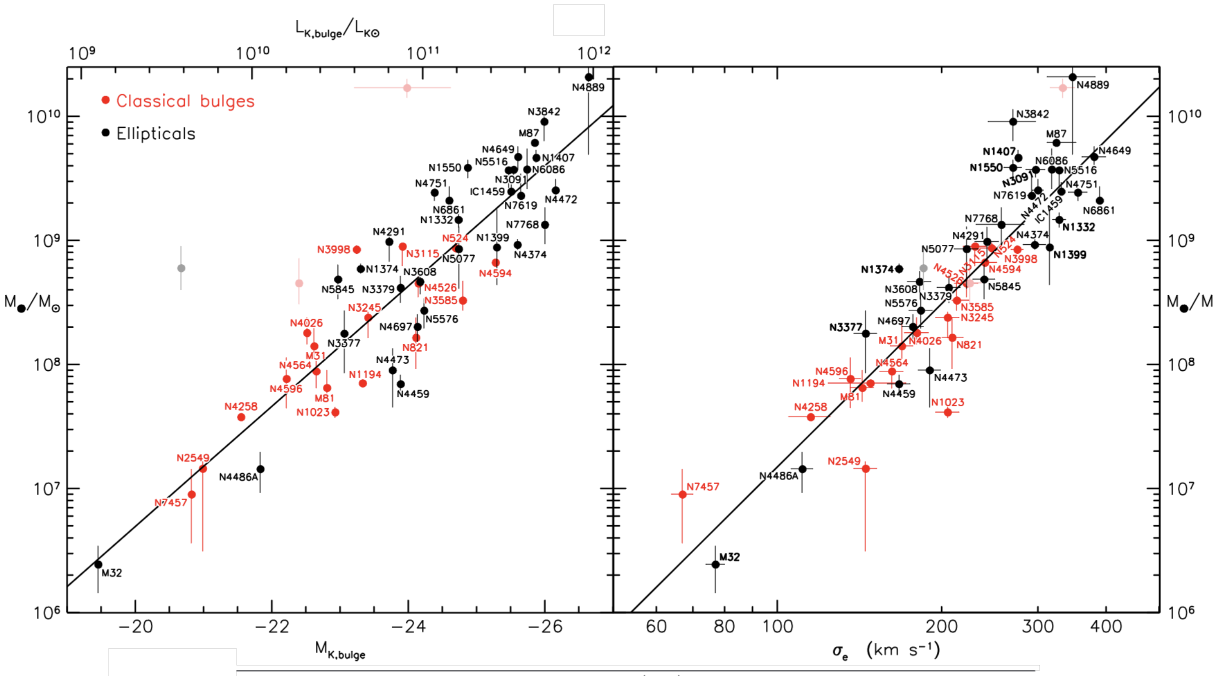

Figure 1.6: The $M_{\rm BH} - L_{\rm bulge}$ and $M_{\rm BH} - M_{\rm bulge}$ correlations (left) and the $M_{\rm BH} - \sigma$ correlation (right). The red points are classical bulges and the black points are elliptical galaxies. The lines represent the least-squares fit to the points. Taken from Kormendy & Ho (2013).

In the following sections I discuss these components.

1.3.1 SUPERMASSIVE BLACK HOLE

It is generally accepted that supermassive black holes (SMBHs; $M_{\rm BH} \simeq 10^6 - 10^{10}\,M_\odot$) exist at the centres of almost all massive ($M_* \gtrsim 10^{9.5}\,M_\odot$). The region of a galaxy where the gravitational potential of the galaxy is dominated by the BH gravitational potential is known as the sphere of influence (SOI). The radius of the sphere of influence is defined as

$$r_{\rm SOI} = \frac{GM_{\rm BH}}{\sigma^2} \tag{1.14}$$

where $M_{\rm BH}$ is the mass of the black hole, σ is the stellar velocity dispersion of the host galaxy bulge and G is the gravitational constant. A number of correlations have been found between the masses of these SMBH and the properties of their host galaxies.

The first correlation between the SMBH and the host galaxy properties that was discovered was the $M_{\rm BH} - L_{\rm bulge}$ correlation. Dressler & Richstone (1988) initially reported that the SMBH in M31 was 5-10 times more massive than the SMBH in M32 which is much closer to the ratio of bulge luminosities (~15) than it is to the ratio of their total luminosities (~70).

This implies that the SMBH mass correlates with the bulge luminosity but not the luminosity of the disk. This correlation was formally proposed by Dressler (1989) and then expanded on by Kormendy (1993). The $M_{\rm BH} - L_{\rm bulge}$ correlation also implies a correlation with bulge mass ($M_{\rm bulge}$). This correlation has been studied using different methods of measuring the bulge mass such using the virial theorem, $M_{\rm bulge} \propto r_{\rm e}\sigma^2$ where $r_{\rm e}$ is the effective radius and σ is the velocity dispersion (Marconi & Hunt, 2003), dynamical modeling (Magorrian et al., 1998; Häring & Rix, 2004) or by assuming a mass-to-light ratio (McLure & Dunlop, 2002). All these methods show a good correlation between the SMBH mass and the mass of the bulge. However, it has been found that the SMBH mass does not correlate with the mass of pseudobulges which have properties closer to disks than of classical bulges (e.g. Kormendy et al., 2011; Sani et al., 2011; McConnell & Ma, 2013). It has also been found that SMBH mass does not correlate with the mass of galaxy disks (e.g. Kormendy & Gebhardt, 2001; Kormendy et al., 2011).

Following on from the discovery of the $M_{\rm BH} - M_{\rm bulge}$ correlation it was also discovered that the SMBH mass also correlates with the velocity dispersion of the galaxy. This $M_{\rm BH} - \sigma$ relation was initially published by Ferrarese & Merritt (2000) and Gebhardt et al. (2000) and found that the correlation was very tight with a scatter of 0.30 dex. Over the years has been expanded to bigger samples, tested if it applies to AGN and tested in the distant Universe. As with the $M_{\rm BH} - M_{\rm bulge}$ relation it seems that pseudobulges differ from the $M_{\rm BH} - \sigma$ relation (e.g. Hu, 2008; Greene et al., 2010; Kormendy et al., 2011; Sani et al., 2011; McConnell & Ma, 2013). The $M_{\rm BH} - L_{\rm bulge}$, $M_{\rm BH} - M_{\rm bulge}$ and $M_{\rm BH} - \sigma$ correlations are shown in Figure 1.6.

The findings of these tight correlations between the SMBH mass and the host galaxy properties could suggest a co-evolution of the two with the findings that pseudobulges do not follow these correlations potentially indicating the origin of this co-evolution. Classical bulges that correlate with SMBH masses are believed to form through major mergers (see Kormendy, 2013, for a review). On the other hand pseudobulges are believed to form through slow secular processes that do not involve major mergers (see Kormendy, 1993; Kormendy & Kennicutt, 2004; Kormendy, 2013, for reviews). This difference in formation could suggest that the mergers that form bulges also rapidly fuels the SMBH that is being hosted (e.g. Hopkins et al., 2006) explaining their co-evolution. Whilst SMBH in disk galaxies, that may host pseudobulges, grow slowly through secular processes and do not co-evolve with their host galaxy (Greene et al., 2008).

AGN are another potential mechanism that could set this co-evolution. It has been shown that SMBH grow mostly during phases when they are active (Soltan, 1982; Marconi et al., 2004; Shankar et al., 2004; Merloni & Heinz, 2008) and soon after these SMBH-host galaxy correlation were found it was suggested that AGN winds interacting with the ISM could explain them (Silk & Rees, 1998; Fabian, 1999; King, 2003; Granato et al., 2004). In this idea the AGN can heat up and eject gas from the nuclear regions of the galaxy which stops the growth of the SMBH but also of the galaxy which in turn gives rise to the observed scaling relations. It has also been found the AGN activity and star formation as a function of redshift have evolved very similarly. They both peak at redshift $z \sim 1-3$ and rapidly decline towards the local universe as can be seen in Figure 1.7 (Delvecchio et al., 2014; Madau & Dickinson, 2014; Aird et al., 2015). This suggests that these two processes are evolving together. Another indicator of this co-evolution is that moderate and high luminosity AGN predominately are found in galaxies with active star formation (Merloni et al., 2010; Rosario et al., 2013; Heinis et al., 2016; Aird et al., 2018; Stemo et al., 2020). This could be explained if the gas that is fuelling star formation is also fuelling the AGN activity.

A full review on SMBH-host galaxy co-evolution can be found in Kormendy & Ho (2013).

1.3.2 ACCRETION DISK

The material that is being accreted onto the SMBH is expected to form a geometrically thin, optically thick accretion disk due to the conservation of angular momentum (e.g. Shakura & Sunyaev, 1973; Sun & Malkan, 1989). It is from this accretion disk that the majority of the thermal emission is expected to be produced. Infalling material loses gravitational potential energy which is converted into electromagnetic radiation through frictional heating of the infalling material. The accretion disk has a radius of ~0.01pc (e.g. Hawkins, 2007) and has a temperature of $10^4 - 10^5\mathrm{K}$ (e.g. Bonning et al., 2007) though in other accreting systems such as X-ray binaries (XRBs) this temperature can reach $10^7\mathrm{K}$.

The accretion disk emission spectrum is a composite black body which contains emission from different regions of the accretion disk with different temperatures. The black body function is

$$B_\nu(T(R)) = \frac{2h\nu^3}{c^2}\frac{1}{e^{\frac{h\nu}{kT(R)}} - 1} \tag{1.15}$$

where ν the frequency, h is the Planck constant, c is the speed of light, k is the Boltzmann constant and $T(R)$ is the temperature of the disk at a radius R from the centre which for the typical accretion disk is

$$T(R) \propto \left(\frac{R}{R_S}\right)^{-3/4} \tag{1.16}$$

where R_S is the inner radius of the accretion disk. The emission from an AGN accretion

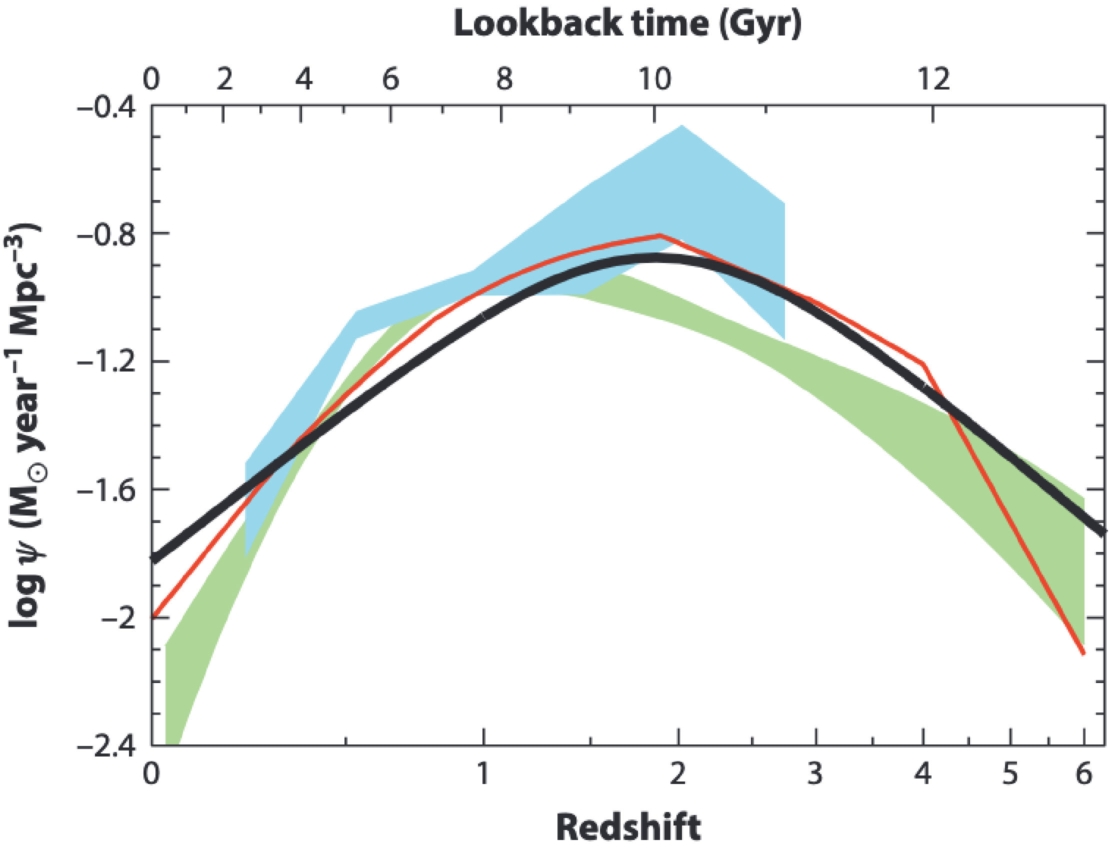

Figure 1.7: Comparison of the best fitting star formation history (black curve) with the black hole accretion history derived from X-rays (red curve and green region) and infrared (blue region). Taken from Madau & Dickinson (2014).

disk is expected to peak in the optical/UV region of the spectrum. An example of the expected accretion disk emission spectra is shown in Figure 1.8.

An optically thin, hot ($\mathrm{T} \sim 10^9\mathrm{K}$) atmosphere of electrons is believed to exist above the accretion disk often called the corona (Haardt & Maraschi, 1993). Details of the corona are not clear but it is believed that photons emitted from the accretion disk can be inverse Compton scattered by electrons in the corona to X-ray energies (Ciotti & Ostriker, 1997).

At low, sub-Eddington, accretion rates the gas has low density and is unable to cool efficiently within an accretion time. The viscous energy is stored in the gas as thermal energy rather than being radiated away and is advected onto the SMBH. This causes the gas to puff up rather than settling down into a thin accretion disk and forms an optically thin, geometrically thick object often called an advection dominated accretion flow (i.e. ADAF; Narayan & Yi, 1995b).

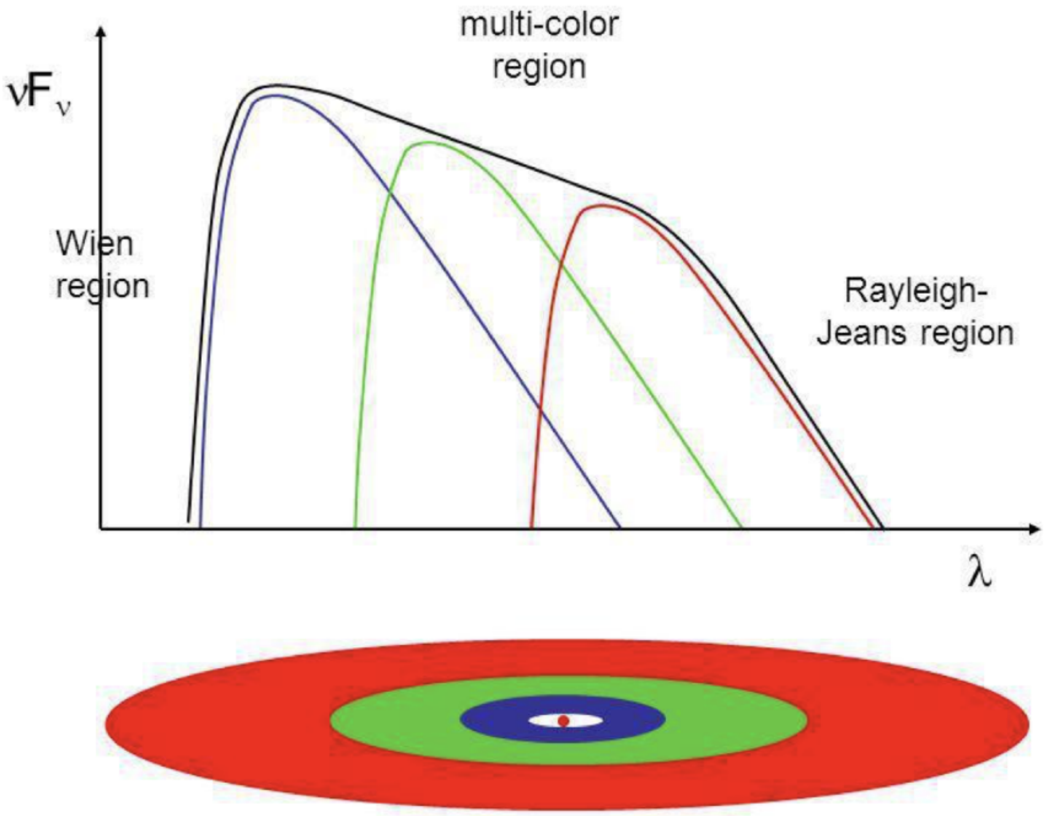

Figure 1.8: Expected SED of an AGN accretion disk. Taken from Disk Thermal Structure lecture by C.P. Dullemond.

1.3.3 BROAD LINE REGION

Beyond the accretion disk at a distance of 0.1-1pc (e.g. Peterson, 1993) exists a region of dense ($\sim 10^{10}\mathrm{cm}^{-3}$) gas clouds moving at high velocities ($\sim 10^3 - 10^4\mathrm{km/s}$) known as the broad line region (BLR). The gas clouds in this region produce broad emission lines (1000-20,000 km/s) due to photo-ionisation from the accretion disk (Davidson & Netzer, 1979) with the width of these lines being due to Doppler broadening from the high velocities of the gas clouds in this region. The most prominent lines produced from this region are the hydrogen Balmer-series lines ($\mathrm{H}\alpha$, $\mathrm{H}\beta$, $\mathrm{H}\gamma$), the hydrogen Lyα and line from ions (Mg II, C III] and C IV).

The size of the BLR has been shown to correlate with the AGN luminosity in the form

$$R_{\mathrm{BLR}} \propto L_{\mathrm{AGN}}^{\alpha} \tag{1.17}$$

where α has a value of ~0.6 (Kaspi et al., 2000, 2005; Bentz et al., 2013). The width of the emission lines can be used to estimate the mass of the SMBH

$$M_{\mathrm{SMBH}} = \frac{R_{\mathrm{BLR}} V_{\mathrm{BLR}}^2}{G} = \frac{R_{\mathrm{BLR}} f \Delta V^2}{G} \tag{1.18}$$

where R_{BLR} is the radius of the BLR, V_{BLR} is the virial velocity, ΔV is the width of the emission lines, f is the virial factor that accounts for the difference between the width of the emission lines and the virial velocity and G is the gravitational constant (Peterson et al., 2004).

1.3.4 TORUS

Surrounding the accretion disk and the BLR is expected to be a geometrically and optically thick dusty torus with a size of 1-10pc. The inner boundary of the torus which is assumed to be the dust sublimation radius R_{sub} is set by the dust sublimation temperature which varies for graphite and silicate grains (Barvainis, 1987). For graphite (C) grains the sublimation temperature is $T_{\mathrm{sub}} \simeq 1800\,\mathrm{K}$ and the mean sublimation radius is

$$\langle R_{\mathrm{sub,C}} \rangle \simeq 0.5 L_{46}^{1/2} \left[\frac{1800}{T_{\mathrm{sub}}}\right]^{2.6} f(\theta)\, pc \tag{1.19}$$

whilst for silicate (Si) grains the sublimation temperature is $T_{\mathrm{sub}} \simeq 1400\,\mathrm{K}$ and the mean sublimation radius is

$$\langle R_{\mathrm{sub,Si}} \rangle \simeq 1.3 L_{46}^{1/2} \left[\frac{1500}{T_{\mathrm{sub}}}\right]^{2.6} f(\theta)\, pc \tag{1.20}$$

where $L_{46} = L_{\rm AGN}/10^{46}{\rm ergs}^{-1}$ and $f(\theta)$ is an angle dependent term that allows for anisotropy of the AGN emission (Netzer & Trakhtenbrot, 2014). For an isotropic radiation source $f(\theta) = 1$ and for a thin disk with an atmosphere of electrons $f(\theta) = [{\rm cos}\theta(1 + 2{\rm cos}\theta)/3]^{1/2}$. These relations assume a mean grain size of $a = 0.05\,\mu{\rm m}$. The outer boundary of the torus may be set by the SMBH sphere of influence, which is roughly 10pc for nearby galaxies, though this is difficult to measure as it might be hard to distinguish the edge of the torus from the nuclear star forming disk. It is believed that this dusty torus can obscure the emission coming from the accretion disk depending on the viewing angle of the observer.

The emission from the accretion disk is absorbed by the dust in the torus and re-emits it as a blackbody at infrared (IR) wavelengths. The temperature of the dust at a given radius is given by

$$T(R) = T_{\rm sub}\left(\frac{R}{R_{\rm sub}}\right)^{\frac{-2}{4+\gamma}} \tag{1.21}$$

where $T_{\rm sub}$ is the sublimation temperature, $R_{\rm sub}$ is the sublimation radius and γ is the infrared power law index which is approximately 1.6 (Barvainis, 1987).

Initially, the structure of this torus was assumed to be smooth and homogeneous (Pier & Krolik, 1992). However, new models such as clumpy torus (Nenkova et al., 2008) or a two-phase torus with clumps and inter clump material (Stalevski et al., 2012) has been proposed that better fit observations.

1.3.5 NARROW LINE REGION

Beyond the torus exists a bi-conical structure of lower density ($\sim\ 10^3{\rm cm}^{-3}$) and lower velocity ($\sim\ 500{\rm km/s}$) gas clouds known as the narrow line region (NLR). The gas in the NLR is photo-ionised by the accretion disk producing narrow emission lines (300-1000 km/s) due to lower velocity of the gas clouds in this region. Due to lower density of the gas in this regions collisions are less frequent allowing for both permitted and forbidden emission lines. The most prominent narrow emission lines from this region are hydrogen Lyα, CIV, CIII], [OIII] (λ4959 and λ5007), [NII] and [SII].

The size of the NLR is set by how far the radiation from the accretion disk can ionize the surrounding gas. It appears that the radius of the NLR, $R_{\rm NLR}$, varies with Peterson et al. (2013) finding $R_{\rm NLR}$ to only be 1-3pc, Vaona et al. (2012) finding $R_{\rm NLR}$ that varies from 200-900pc and Bennert et al. (2006) finding $R_{\rm NLR}$ to reach kpc scales. It has been found that the size of the NLR is related to the luminosity of some of most prominent forbidden lines.

It has been found that

$$R_{\rm NLR} \propto L_{\rm [OIII]}^{\alpha} \tag{1.22}$$

where $L_{\rm [OIII]}$ is the luminosity of the [OIII]$\lambda 5007$ emission line and α has a value of 0.55 and 0.32 for type 1 and type 2 AGN respectively (Bennert et al., 2004).

1.3.6 RADIO JETS

Large scale jets are some of the most prominent features of AGN with roughly 10% of AGN possessing powerful jets. These jets emerge from the pole of the SMBH-accretion disk system and can extend from kpc to Mpc away from the SMBH.

These jets are very luminous at radio wavelengths as the charged particles moving at relativistic velocities along magnetic fields produce synchrotron emission (Begelman et al., 1984).

It is still not clear how these jets are launched from the SMBH. However, one popular theory is that magnetic fields in the accretion disk of a rotating SMBH creates an electric field that can accelerate charged particles to relativistic velocities away from the SMBH (e.g. Blandford, 2001).

1.4 MULTI-WAVELENGTH VIEW OF AGN

AGN emit all across the electromagnetic spectrum with different mechanisms giving rise to the emission in each band. An example of an AGN spectral energy distribution is presented in Figure 1.9. I will briefly cover each band of the electromagnetic spectrum and the emission from the AGN in each of the bands.

1.4.1 RADIO EMISSION

As described in Section 1.3.6 roughly 10% of AGN have powerful radio jets which are luminous in the radio band. The objects that have the ability to launch radio jets have been called radio-loud (RL) AGN and are around 10^3 times brighter than objects that do not possess a radio jet which are often called radio-quiet (RQ) AGN. The origin of the radio emission in RQ AGN is still not clear with star formation, AGN driven winds, free-free emission from photo-ionized gas, low power jets and the innermost accretion disk coronal activity all being potential mechanisms (Panessa et al., 2019).

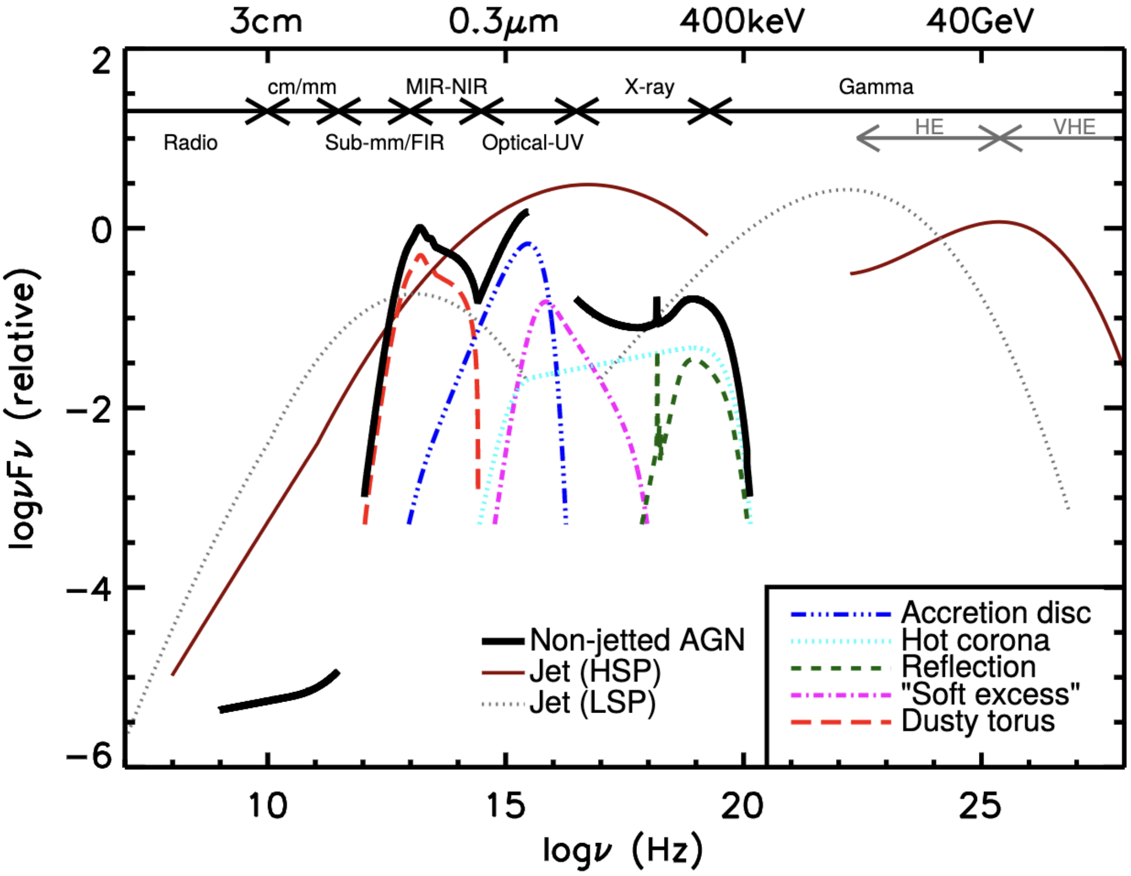

Figure 1.9: Schematic of an AGN SED. The black line represents the total emission of an non-jetted AGN with the coloured curves representing the individual components. The brown solid line and the dotted line represent the SED of a high synchrotron peaked blazar (HSP) and a low synchrotron peaked blazar (LSP) respectively. Taken from Harrison (2014).

1.4.2 MM/SUB-MM EMISSION

The study of AGN at mm/sub-mm wavelengths has only been possible in recent years due to the high-resolution observations needed to separate the AGN emission from the emission of the host galaxy. Inoue & Doi (2018) studied the mm emission in two nearby AGN and found that the mm emission may be due to self-absorbed synchrotron emission from compact regions. Other potential mechanisms include dust heated by the AGN, outflow-driven shocks, and jets (e.g. Jiang et al., 2010; Nims et al., 2015). It has been found by Behar et al. (2020) that there could be a 14 day delay in X-ray emission behind the mm emission. This could suggest that the mm emission and X-ray emission are produced on the scales of a few gravitational radii potentially from a hot corona. The origin of this emission is re-visited in Chapters 4 and 5.

1.4.3 INFRARED EMISSION

The primary IR emission mechanism in AGN is from dust in the surrounding torus that reprocess the emission from the AGN accretion disk into the IR. This emission dominated the AGN SED from $\sim 1\mu\mathrm{m}$ to a few tens of micron. At near-infrared (NIR) wavelengths the emission is dominated by the emission of hot dust ($\sim 1500\mathrm{K}$) from the inner most region of the torus. However, there could also be some contribution from the NIR tail of the "big blue bump" from the central accretion disk (Kishimoto et al., 2007). The MIR emission from AGN tends to be dominated by warm (200-600K) dust surrounding the central accretion disk (Sanders et al., 1988). Finally, it has previously been believed that AGN emit negligibly at FIR wavelengths. However, work (e.g. McKinney et al., 2021) has shown that AGN can heat host galaxy scale dust which emits at FIR wavelengths.

1.4.4 OPTICAL/UV EMISSION

At optical/UV wavelengths the emission is powered by accretion onto the SMBH which gives rise to a power law continuum (see Section 1.3.2 and Figure 1.9). The key feature that appears in the optical/UV SED of AGN is the "big blue bump" which is normally thought to be due to the thermal emission of the accretion disk. The spectra of solar-type stars peak around $\lambda = 500\mathrm{nm}$ and those of O-stars at around $\lambda = 350\mathrm{nm}$. Whilst the big blue bump appears at around $\lambda = 100 - 400\mathrm{nm}$ so cannot be due to stellar activity with AGN hosting galaxies appearing to be more blue then non-active galaxies (Shields, 1978; Malkan & Sargent, 1982).

1.4.5 X-RAY EMISSION

X-ray emission from AGN seems to be near universal can penetrate through large column densities of gas and dust. X-ray emission from AGN is believed to be due to accretion disk photons being inverse Compton scattered to X-ray energies via the accretion disk corona which sits above the accretion disk Ciotti & Ostriker (1997). However, thermal X-ray emission due to the inner regions of the accretion disk can also produce low energy X-rays (e.g. Sobolewska et al., 2004). The jets from AGN may also produce X-rays due to Compton up-scattering of non-thermal photons (e.g. Blundell et al., 2006).

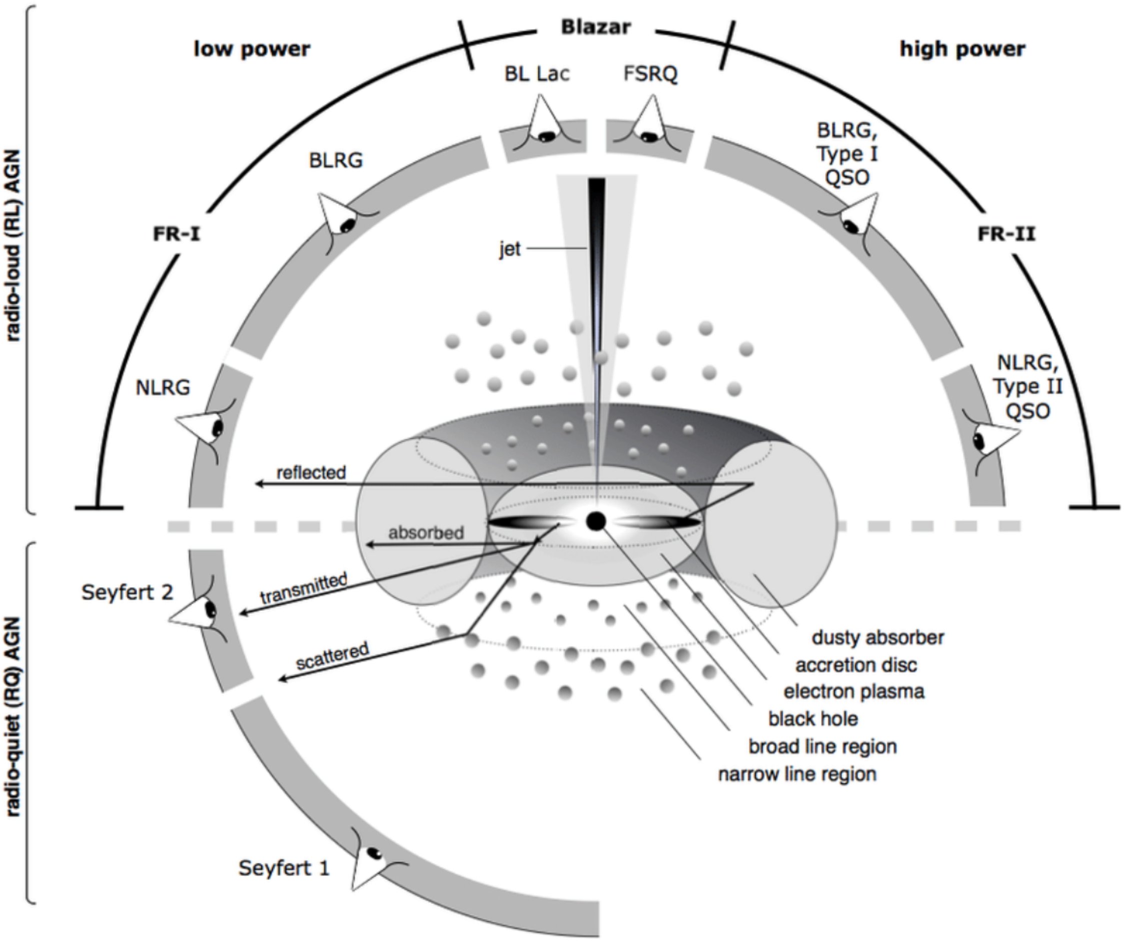

Figure 1.10: Schematic of the radio-loud (top) and radio-quiet (bottom) unified model. Taken from Beckmann & Shrader (2012).

1.4.6 γ RAY EMISSION

Most astronomical objects cannot emit in the γ-ray band including non-jetted AGN. However, blazars (AGN with their jets pointing in the direction of the observer) and some nearby radio galaxies can emit in this band. One potential emission for γ-rays in these sources is through inverse Compton scattering (e.g. Maraschi et al., 1992) between the electrons in the jet and their own synchrotron emission (synchrotron self-Compton) or an external photon field (external self-Compton).

1.5 AGN MODELS

AGN are observed to have a range of properties that have traditionally been combined into the AGN Unified Model (Antonucci, 1993; Urry & Padovani, 1995). In these models the difference in observational properties is explained by the different viewing angles of the observer.

1.5.1 RADIO-QUIET UNIFICATION

In the case of radio quiet AGN they can be split into different classes depending on whether you are viewing the central engine through the dusty torus structure. In type 1 (unobscured) AGN your observations are not impeded by the dusty torus and these objects show broad (1000–20,000 km/s) emission lines arising from the BLR in these objects. In type 2 (obscured) AGN the emission from the BLR is hidden by the dusty torus structure and instead you observe narrow (300-1000 km/s) emission lines. There are objects that have weak or unusual emission lines have been called type 0 AGN and it is believed that these objects are observed when viewing the AGN at a very small angle to the pole so their spectra may be influenced by a jet or outflowing gas along the line of sight. An example of the radio-quiet unified model is shown in the bottom half of Figure 1.10.

The discovery of polarized broad lines in the spectrum of the Type 2 AGN hosting galaxy NGC1068 further supported the idea that the observational differences between type 1 and type 2 AGN are due to obscuration from a dusty torus (Antonucci & Miller, 1985). It is believed the polarized broad lines seen in the spectrum of NGC1068 are produced by the reflection of radiation emitted in the BLR. Cone-shaped ionized matter has been observed in Type 2 AGN hosting galaxies (e.g., NGC5728, Wilson et al., 1993) further supporting that the obscuring material has a toroidal structure.

However, there are some issues with this radio-quiet unification scheme. For example, it has been observed that some changing look AGN can vary from type 1 to type 2 (e.g. LaMassa et al., 2015) and in some rare cases some AGN have been discovered with no broad lines but with no obscuration detected either which could indicate that the BLR is missing in these sources (e.g. Shi et al., 2010).

1.5.2 RADIO-LOUD UNIFICATION

In the radio-loud regime there are a variety of different objects. Fanaroff & Riley (1974) recognized that radio galaxies (galaxies with large lobes emitting at radio wavelengths powered by jets from the AGN) can be separated into two classes based on their luminosity and morphology. FR Is are lower-luminosity and have their peak emission near the nucleus whilst FR IIs are higher-luminosity and have peak emission in their radio lobes. The luminosity split is quite sharp at 178 MHz with FR Is being below and FR IIs being above a threshold luminosity of $L_{178} \approx 2 \times 10^{25} \mathrm{W\,Hz^{-1}}$.

Similar to the radio-quiet regime radio-loud objects can be split into different classes based on the observed optical and UV emission lines. In the radio-loud regime Type 1 AGN, that show both broad and narrow emission lines, are known as broad-line radio-galaxies (BLRG) at low luminosities and radio-loud quasars at high luminosities. Also in the radio-loud Type 1 AGN class are steep spectrum radio quasars (SSRQ) and flat spectrum radio quasars (FSRQ) which vary in the shape of their radio continuum. Radio loud type 2 AGN, that only show narrow emission lines, are called narrow-line radio galaxies (NLRG). Finally, analogous to the Type 0 AGN in the radio-quiet regime in the radio-loud regime there are BL Lacertae (BL Lac) objects which are a subset of blazars which have very unusual spectral features.

Similar to the radio-quiet regime, there have been attempts to unify all these radio-loud object into one unified scheme (Urry & Padovani, 1995). In addition to the dusty torus included in the radio-quiet unification scheme this model needs to include the relativistic jet. At low AGN powers you will find FR I objects and the split between BLRG and NLRG depends on if you are viewing through the dusty torus as in the radio-quiet picture. However, in this model at low AGN power BL Lac objects are Doppler boosted FR I radio galaxies that are being viewed at a very small angle from the relativistic jet. In this case BL Lacs are less luminous then other AGN classes but their emission is being boosted due to relativistic effects. At high AGN powers you will find FR II objects and again the difference between viewing broad lines depends on whether you are viewing through the dusty torus. In this picture FSRQ are objects that are being viewed at a small angle from the relativistic jet. A example of the radio-loud unified model is shown in the top half of Figure 1.10.

This radio-loud unification has some unanswered questions with a major one being what causes the differences between FR I and FR II radio galaxies. One potential idea proposed by Reynolds et al. (1996) is that FR II radio galaxies host a standard thin accretion disk whilst FR I radio galaxies instead host an ADAF. It is also not clear the role that the environment plays in creating FR I and FR II radio galaxies.

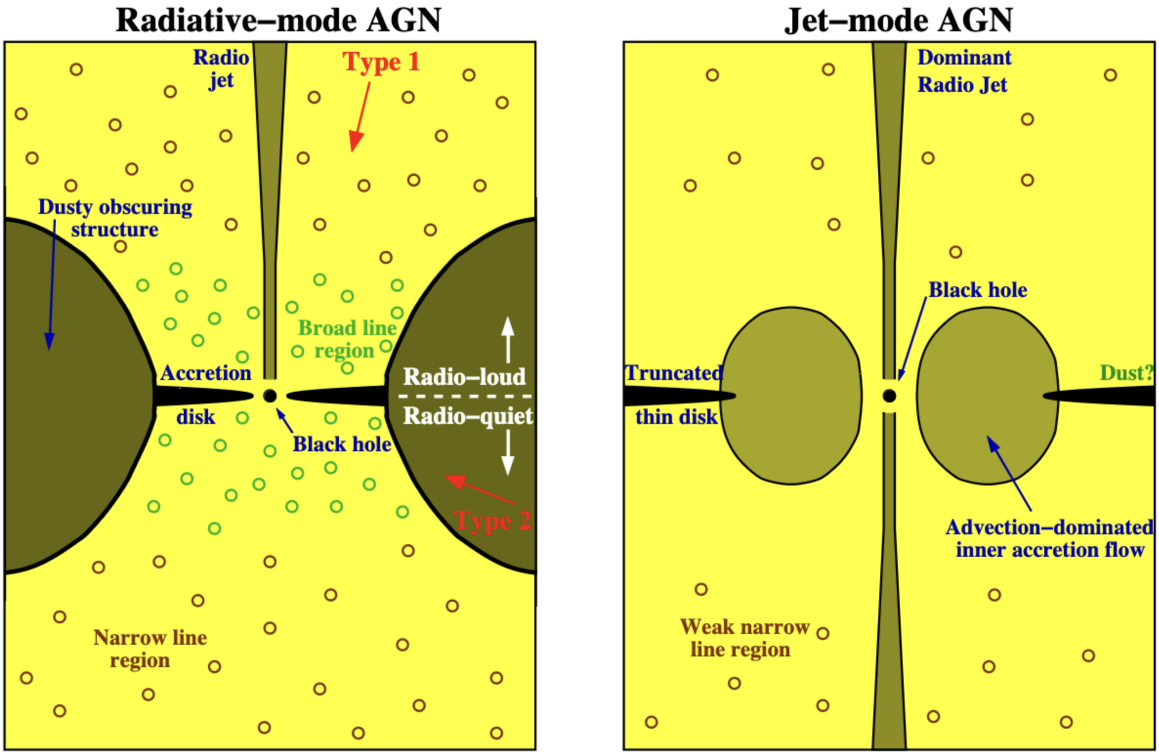

Figure 1.11: Diagram of radiative (left panel) and kinetic (right panel) mode AGN. Taken from Heckman & Best (2014)

1.5.3 RADIATIVE MODE/KINETIC MODE UNIFICATION

In recent years Heckman & Best (2014) found in the local universe ($z < 0.1$) AGN can be split into two separate classes based on their energetic output. These two classes are called radiative and jet (or kinetic) mode AGN. These two classes can be differentiated by their Eddington ratio. A schematic of these two classes of AGN is shown in Figure 1.11.

In radiative-mode AGN the accretion occurs at high rates ($\gtrsim 1\%$ of the Eddington limit) through optically-thick and geometrically-thin disk (Shakura & Sunyaev, 1973). This feedback mode is radiatively efficient, so the dominant energy output is from the conversion of the potential energy of the accreted material onto the SMBH into electromagnetic radiation. Nearby radiative mode AGN with weak or no radio jet emission have historically been called Seyfert galaxies. These objects possess all the characteristics of the "conventional" AGN picture as laid out in the standard unified model (e.g. Antonucci, 1993; Urry & Padovani, 1995), and are typically hosted by later Hubble type galaxies (e.g. Martini et al., 2003). In some cases radiative-mode AGN can launch an outflow of non-thermal plasma (i.e. radio jets) which emit radio synchrotron emission. These objects are often termed radio-loud AGN.

Kinetic-mode AGN produce very little radiation and instead channel the bulk of the energy generated from the accretion of material into collimated outflows of non-thermal plasma (i.e. radio jets). In these objects the geometrically-thin accretion disk is absent or truncated at some inner radii and likely replaced by a geometrically-thick, optically-thin advection dominated accretion flow (i.e. ADAFs Narayan & Yi, 1995b), whereby the material is accreted onto the SMBH at low rates ($<<$1% of the Eddington limit). AGN producing strong kinetic-feedback are instead typically identified as radio galaxies (RGs) and -based on their optical spectra- can be divided into two main classes (Best & Heckman, 2012): high-excitation radio galaxies (HERGs) and low-excitation radio galaxies (LERGs). HERGs show strong high-ionisation emission lines in their optical spectra, produce both radiative and kinetic AGN feedback, and are typically hosted by massive ($M_* \gtrsim 10^{9.5} M_\odot$) early-type galaxies (ETGs). LERGs show no or weak LINER (low-ionisation nuclear emission-line region)-like emission lines in their optical spectra, produce almost exclusively kinetic feedback, and are typically hosted in very massive ($M_* \gtrsim 10^{11} M_\odot$) ETGs. Example optical spectra of HERGs and LERGs are shown in Figure 1.12.

1.6 OBSERVATIONAL FACILITIES

In this thesis I utilise data from a number of different observational facilities. In the following sections I will introduce and describe the three main facility I have used in this work.

1.6.1 ALMA

The Atacama Large Millimetre/sub-millimetre Array (ALMA) is an interferometer that is located in the Atacama Desert in Northern Chile that started observing in 2011. The ALMA Observatory is made of 66 antennae arranged in two arrays. The 12m array is composed of 50 12m dishes whilst the Atacama Compact Array (ACA) is composed of 12 7m dishes and 4 12m dishes which act as a single dish (Total Power or TP Array). The 12m array can be organised to have baselines ranging from 15m up to $\sim$16km. The TP Array antennas have a diameter of 12m whilst the 7m array has baseline ranging from 9 to 30m. The ALMA antennae have or will soon have receivers that can capture light from

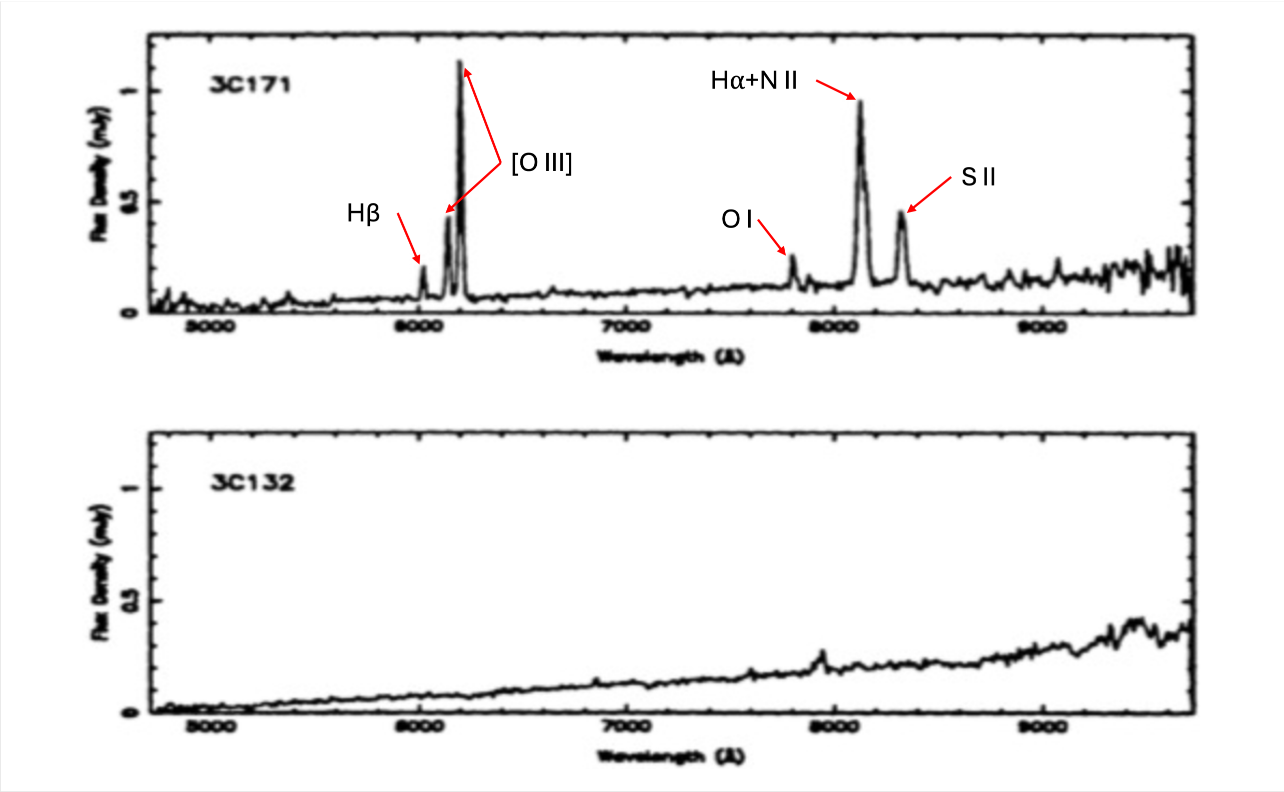

Figure 1.12: Example of HERG (top) and LERG (bottom) optical spectra. Taken from Laing et al. (1994).

Figure 1.13: An image of ALMA in one of its many configurations. Image credit to Juan Carlos Rojas.

10 different bands. These go from band 1 which has a wavelength range of 6-8.6mm (35-50 GHz) up to band 10 which has a wavelengths range of 0.3-0.4mm (787-950 GHz). An image of the ALMA observatory is shown in Figure 1.13.

Being an interferometer ALMA works by combining the signals received at multiple physically separated antennae. The signal received with each pair of antennas is called the visibility. The visibility has a sinusoidal shape with the amplitude of the sinusoid relating to the brightness of the emission observed and the phase of the sinusoid relating to the position of the source on the sky. The angular size of source that can be observed is related to distance between the antennas. For a single dish this angular resolution is defined as

$$\theta = \frac{\lambda}{D} \tag{1.23}$$

where λ is the observed wavelength and D is the diameter of the dish. In the case of an interferometer with multiple dishes the distance between the dishes, d, replaces the diameter of the dish, D. So the smallest angular scale that the can be resolved depends on d_{max}, the maximum distance between antennas

$$\theta_{\mathrm{min}} = \frac{\lambda}{d_{\mathrm{max}}} \tag{1.24}$$

and the largest angular scales that can be resolved depends on d_{min}, the minimum distance between antennas

$$\theta_{\mathrm{max}} = \frac{\lambda}{d_{\mathrm{min}}} \tag{1.25}$$

.

1.6.2 MUSE

The Multi Unit-Spectroscopic Explorer (MUSE) is an Integral Field Unit (IFU) that is installed on the Very Large Telescope (VLT) at the ESO Paranal observatory in Chile that started observing in 2014. The MUSE instrument operates with an 8m mirror and observes in the optical regime ($\lambda = 475 - 935\mathrm{nm}$) and since 2017 it has been fitted with Adaptive Optics (AO) to correct for distortions caused by turbulence in the high layers of the atmosphere. MUSE can operate in two observing modes: the Wide-Field Mode (WFM) with has a spatial resolution of $\sim\ 0.4''$ and the Narrow-Field Mode (NFM) which has a spatial resolution of $\sim 55 - 80\mathrm{mas}$. An image of the MUSE instrument is shown in Figure 1.14

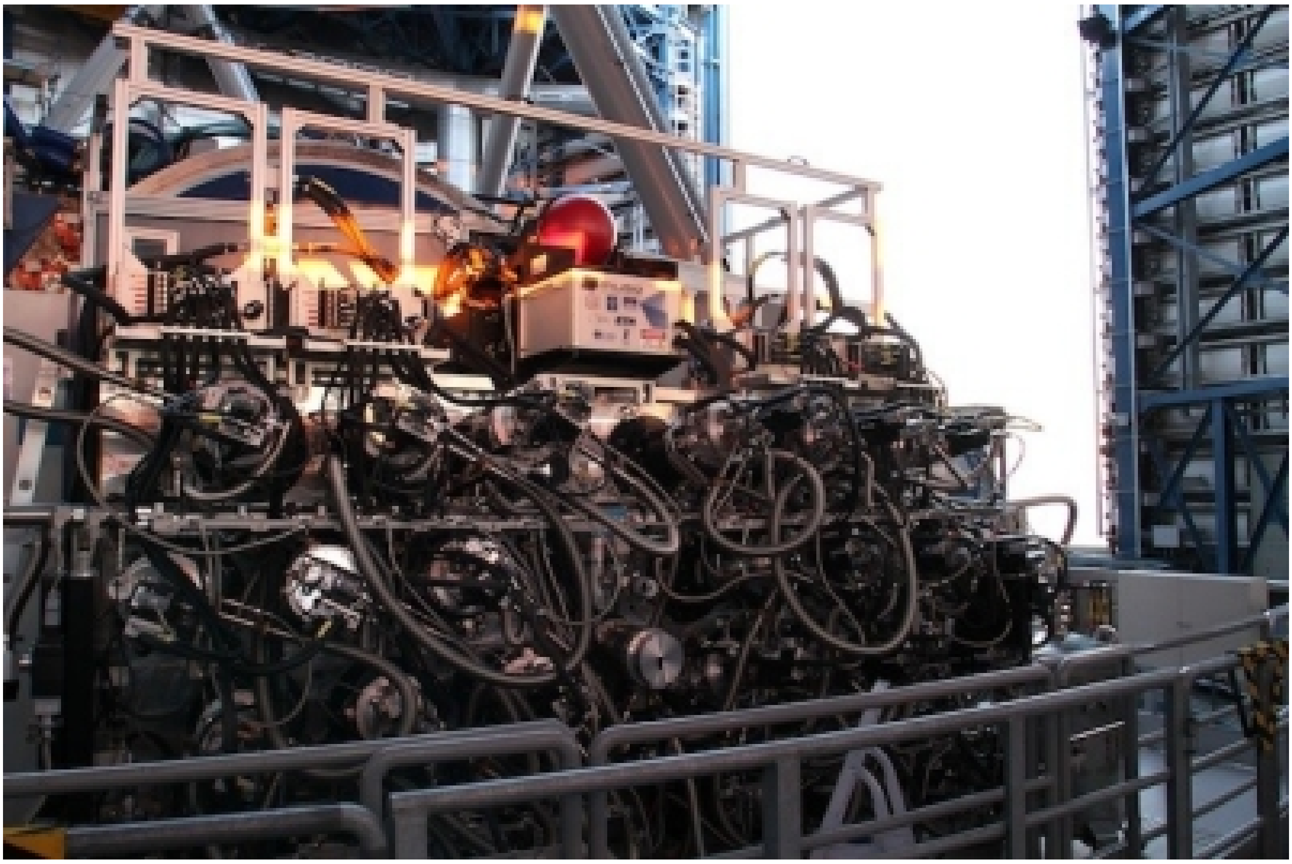

Figure 1.14: The MUSE instrument on the VLT. Image credit to G. Hansali.

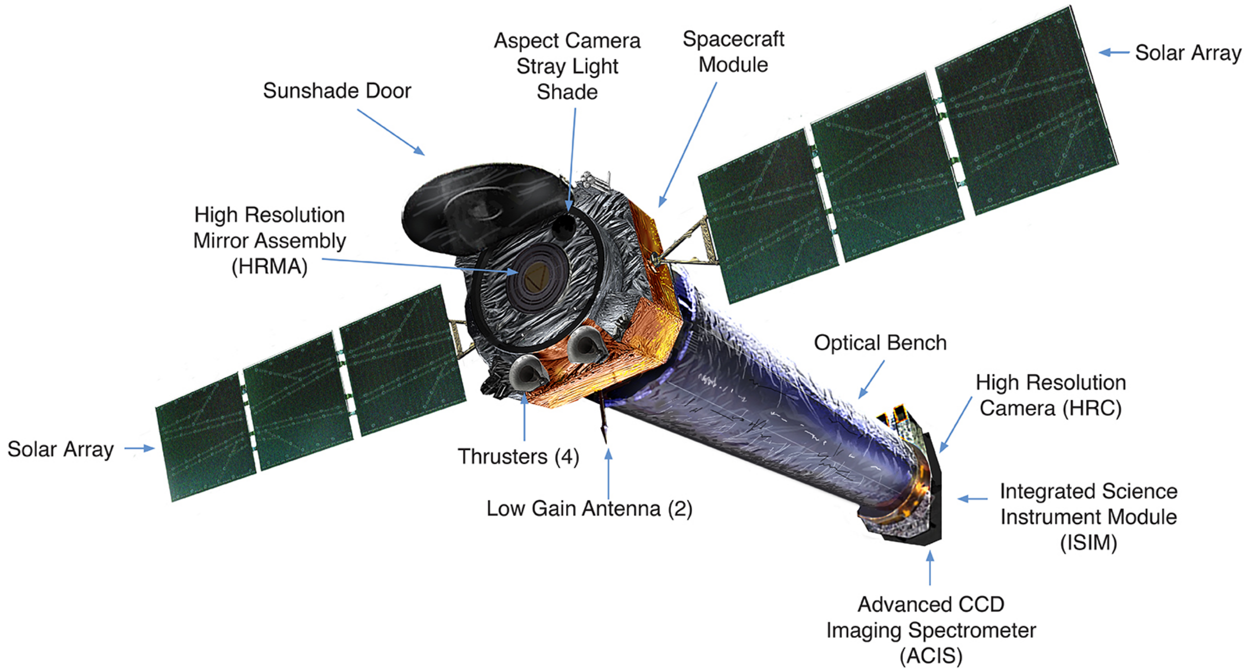

Figure 1.15: A diagram of Chandra and its components. Image credit to NASA/CXC.

1.6.3 CHANDRA

The *Chandra* observatory was launched into orbit in 1999. *Chandra* is fitted with high-resolution optics that provides high angular resolution X-ray observations of $\sim 0.5''$. *Chandra* is fitted with several different instruments. There is the Advanced CCD Imaging Spectrometer (ACIS) with operates in the 0.2-10 keV energy range and is used for spectroscopy and imaging. There is the High Resolution Camera (HRC) which operates in the 0.1-10 keV energy range and is used for high resolution imaging, fast timing measurements, and for observations requiring a combination of both. Finally there are the High Energy Transmission Grating Spectrometer (HETGS) which operates in the 0.4-10 keV energy range and the Low Energy Transmission Grating Spectrometer (LETGS) which operates in the 0.09-3 keV energy range. A diagram of the *Chandra* telescope is shown in Figure 1.15.

1.7 THIS THESIS

In this thesis I am using high resolution multi-wavelength data to study the connection the AGN and their host galaxy in the local Universe. In Chapter 2 I look for correlations between the molecular gas surrounding AGN and the activity from it to understand how the galaxy fuels the AGN. In Chapter 3 I study the AGN excitation mechanism at optical and sub-mm wavelengths to probe how AGN can impact the different phases of the ISM. In Chapter 4 I present a multi-wavelength study of AGN to understand the underlying accretion mechanism and I then extend this study to include stellar mass black holes in Chapter 5. Finally, I summarise the results of this thesis in Chapter 6.

CHAPTER 2

Circumnuclear AGN fuelling

> *“There are many things that I don’t know."*
>
> -Eva Duran Camacho

2.1 INTRODUCTION

One of the largest unanswered questions about AGN is how they interact with their host galaxy and more specifically how the host galaxy can fuel the activity from the AGN. The material that is being accreted onto SMBH which leads to the emission from the AGN must be coming from somewhere. For example, if you take a Seyfert galaxy with an accretion rate of $\sim 0.2\mathrm{M}_{\odot}\,\mathrm{yr}^{-1}$ and a duty cycle of 10^6 years a reservoir of $2 \times 10^5\,\mathrm{M}_{\odot}$ gas would be needed to fuel it (Emsellem, 2003, 2004; Martini, 2004). However, where in the galaxy this gas in coming from and what is causing the gas to lose angular momentum allowing it to be accreted is still unknown.

The central regions of Seyfert galaxies have been often observed to be dominated by cold atomic and molecular gas (e.g. Combes et al., 2013; García-Burillo et al., 2014), suggesting a potential connection with their nuclear activities. The finding by Izumi et al. (2016b) of a positive correlation between the mass of ≈ 100pc-scale circumnuclear disks (CNDs) of dense molecular gas and the black hole mass accretion rate in nearby Seyferts seems to support this hypothesis (see Figure 2.1). More recently, García-Burillo et al. (2021) also found that nuclear activity in these objects can cause deficits in their circumnuclear molecular gas reservoirs, with a negative trend between nuclear 2-10 keV X-ray luminosity and the central gas concentration. In both cases, however, the studies have been conducted

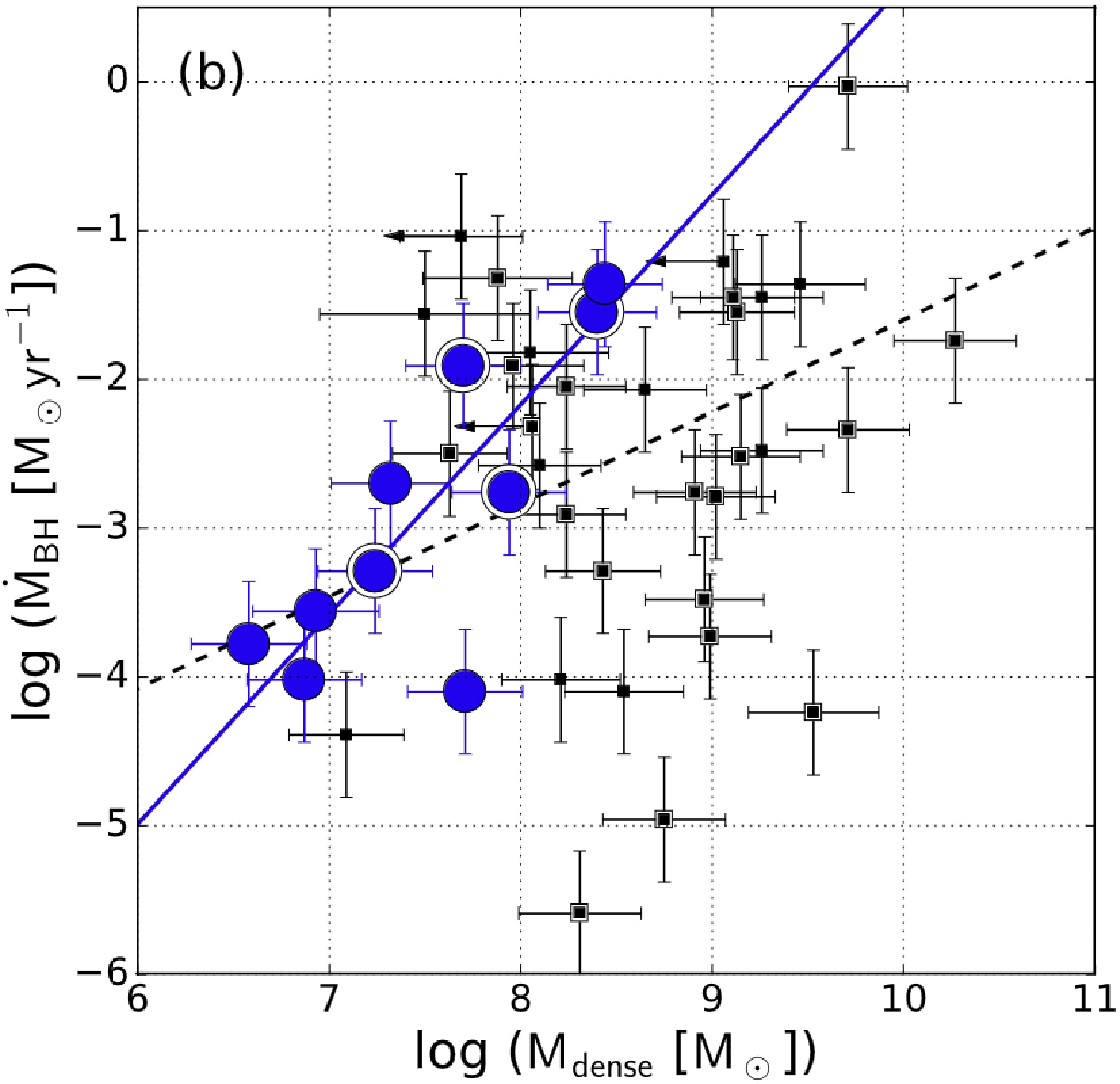

Figure 2.1: Izumi et al. (2016b) relation between the dense gas mass of the circumnuclear disk and the SMBH accretion rate. Blue circles is data taken with interferometers whilst black squares is data taken with single dish telescopes. The blue solid and the black dashed lines show the best fits to these two samples respectively.

on small samples of about 10 AGN of the same type. These samples also span relatively small ranges of AGN luminosities ($L_{\,\text{2-10}\,\mathrm{keV}} \sim 10^{41} - 10^{44}$ erg s^{-1}) and host galaxy properties (almost exclusively barred spirals). It is therefore currently not clear whether or not the inferred cold gas-nuclear activity connection would hold over a broader population of active galaxies.

On the other hand, a long-established scenario suggests that the HERG/LERG dichotomy may be a consequence of different sources for the accreting gas. In this framework, HERGs are fuelled at relatively high rates by cold gas acquired from merging or collisions with gas-rich galaxies (e.g. Best & Heckman, 2012). LERGs are instead powered by the accretion of hot gas from the intergalactic medium (IGM) through Bondi spherical accretion (Bondi, 1952; Hardcastle et al., 2007). This hypothesis was initially supported by studies finding a correlation between jet power and Bondi accretion rate in LERGs (e.g Allen et al., 2006; Hardcastle et al., 2007; Balmaverde et al., 2008). Over the past decade, however, strong evidence has been acquired that cold gas can also play a role in fuelling LERGs, as large masses of cold gas and dust have been often observed at the centres of these objects (i.e. $M_{\mathrm{H}_2} \sim 10^{7} - 10^{10}$ M$_{\odot}$; Prandoni et al., 2010; Ocaña Flaquer et al., 2010; North et al., 2019; Ruffa et al., 2019a,b, 2020). The *total* molecular gas mass of a sample of nearby ETGs (most of which are LERG hosts) have also been observed to weakly correlate with the AGN jet power, providing further evidence that there could be a close connection between the two (Babyk et al., 2019). Models for cold gas SMBH fuelling in typical LERG hosts have also been developed and imply that the observed cold gas reservoirs originate from cooling of the hot X-ray emitting surrounding halos, either directly and smoothly (e.g. Negri et al., 2014) or after chaotic cooling (as predicted in chaotic cold accretion models, CCA; e.g. King & Pringle, 2007; Wada et al., 2009; Nayakshin et al., 2012; Gaspari et al., 2013, 2015, 2017; King & Nixon, 2015). Growing observational evidence provide support to this picture, at least for LERGs located in high-density environments (i.e. in rich groups and clusters). The importance of (chaotic) hot gas cooling in more isolated LERGs is still not clear (e.g. Ruffa et al., 2019b, 2022; Maccagni et al., 2023).

In general, both theoretical studies (e.g. Shlosman et al., 1989) and numerical simulations (e.g. Pizzolato & Soker, 2005, 2010; Wagner et al., 2012; McNamara et al., 2016) have shown that cold gas can play a fundamental role in fuelling nearby AGN (both radiative and kinetic mode), with Ward et al. (2022) finding that AGN are preferentially located in galaxies with high molecular gas fractions. A corresponding comprehensive observational picture, however, is still missing.

The mm-Wave Interferometric Survey of Dark Object Masses (WISDOM) project is exploiting high-resolution CO observations from the Atacama Large Millimeter/submillimeter

Array (ALMA) with the primary aim of measuring SMBH masses in a morphologically-diverse sample of nearby galaxies (e.g. Onishi et al., 2017; Davis et al., 2017, 2018; Smith et al., 2019; North et al., 2019; Smith et al., 2021a,b; North et al., 2021; Lelli et al., 2022; Ruffa et al., 2023). In this chapter, I use WISDOM data with a typical spatial resolution of $\sim$20–30 pc to look for a connection between the *circumnuclear* molecular gas reservoirs observed with ALMA and the SMBH fuelling across a sample with a wide range of nuclear activities (from low/high luminosity Seyferts to LERGs). The main aim is to explore the scenarios described above, testing the cold gas-SMBH fuelling correlations and the scales over which it persists.

This chapter is organised as follows. In Section 2.2, I describe the sample and the multi-wavelength observations used for my analysis. I describe the adopted methodology in 2.3. I present my results in Section 2.4 and discuss them in Section 2.5, before summarising and concluding in Section 2.6.

2.2 OBSERVATIONS

2.2.1 WISDOM SAMPLE

WISDOM ALMA data (with a typical resolution of $\approx 0''.1$ or 30 pc) were originally collected with the intent of measuring SMBH masses. The main selection criterion for WISDOM galaxies was thus to have the SMBH sphere of influence (SOI) spatially-resolvable with ALMA. Therefore, my sample of galaxies is fairly heterogeneous, containing both nearly-quenched ETGs and star-forming spirals with a range of nuclear activities. In particular, here I study data of 35 WISDOM objects, spanning stellar masses $M_{\star}$ from $10^{9.1}$ to $10^{11.8}\mathrm{M}_{\odot}$, and 1.4 GHz radio luminosities $L_{1.4\mathrm{GHz}}$ from $\approx 10^{34}$ to $\approx 10^{41}$ erg s^{-1}. The sample galaxies and their basic parameters are listed in Table 2.1. The AGN properties of my sample sources are discussed in detail below, and comparisons of these with other literature samples are presented in Section 2.4.1.

2.2.2 ALMA OBSERVATIONS AND DATA REDUCTION

Thirty-two sample objects were observed in ^{12}CO(2-1) and 230 GHz continuum using ALMA Band 6, while three (NGC3351, NGC4429, NGC4826) have Band 7 ^{12}CO(3-2) and 345 GHz continuum observations. The ALMA observations used in this work were taken between 2013 and 2020 as part of a large number of projects (see Table 2.1). For each

Table 2.1: Physical parameters of the galaxies sample.

Galaxy (1)	Distance (Mpc) (2)	Jet (3)	Galaxy type (4)	AGN type (5)	$\log(M_\star)$ $(\mathrm{M}_\odot)$ (6)	Mass Ref (7)	log(SFR) $(\mathrm{M}_\odot\ \mathrm{yr}^{-1})$ (8)	Project code (9)	Reference (10)
FRL49	85.7	No	E-S0	Seyfert 2	10.30	L22	0.78	b	Lelli et al. (2022)
FRL1146	136.7	Yes	Sc	Seyfert 1	11.32	M_{K_s}	-	a,b	This work
MRK567	140.6	No	Sc	-	11.26	C17	1.30	a,b	Davis et al. (2022)
NGC0383	66.6	Yes	E-S0	LERG	11.82	MASSIVE	0.00	c,d,e	North et al. (2019)
NGC0404	3.0	No	E-S0	LINER	9.10	S10	-3.04	f	Davis et al. (2020)
NGC0449	66.3	No	SBa	Seyfert 2	10.07	z0MGS	1.19	c,d	Davis et al. (2022)
NGC0524	23.3	No	S0-a	-	11.40	z0MGS	-0.56	e,g,h	Smith et al. (2019)
NGC0612	130.4	Yes	S0-a	LINER	11.76	M_{K_s}	0.85	b,j	Ruffa et al. (2023)
NGC0708	58.3	Yes	E	LERG	11.75	MASSIVE	-0.29	e,h,i	North et al. (2021)
NGC1194	53.2	No	S0-a	Seyfert 2	10.64	z0MGS	-1.74	j	This work
NGC1387	19.9	No	E-S0	LINER	10.67	z0MGS	-0.68	d,e	Boyce, in prep
NGC1574	19.3	No	E-S0	-	10.79	z0MGS	-0.91	c,e	Ruffa et al. (2023)
NGC2110	35.6	No	E-S0	-	10.41	M_{K_s}	-1.41^2	c,k	This work
NGC3169	18.7	Yes	Sa	Seyfert 1	10.84	z0MGS	0.29	e,i	Davis et al. (2022)
NGC3351	10.0	Yes	Sb	LERG	10.28	z0MGS	-1.29^2	e,n	This work
NGC3368	18.0	Yes	Sab	LERG	10.67	z0MGS	-0.29	k	Davis et al. (2022)
NGC3607	22.2	No	E-S0	-	11.34	A3D	-0.54	e,i	Davis et al. (2022)
NGC3862	92.5	Yes	E	LERG	11.68	MASSIVE	-0.63^2	a,e,i,l	This work
NGC4061	94.1	Yes	E	-	11.54	MASSIVE	-0.71	a,e,i,l	Davis et al. (2022)
NGC4261	31.9	Yes	E	LINER	10.80	M_{K_s}	-1.93^2	a,l	Ruffa et al. (2023)
NGC4429	16.5	No	S0-a	-	11.17	A3D	-0.84	e,n	Davis et al. (2018)
NGC4435	16.5	No	S0	-	10.69	A3D	-0.84	e,i	Davis et al. (2022)
NGC4438	16.5	No	Sa	LINER	10.75	z0MGS	-0.3	e,i	Davis et al. (2022)
NGC4501	14.0	Yes	Sb	Seyfert 2	11.00	z0MGS	0.43	e,g	Davis et al. (2022)
NGC4697	11.4	No	E	-	11.07	A3D	-1.08	i	Davis et al. (2017)
NGC4826	7.4	No	SABa	Seyfert 1	10.20	z0MGS	-0.71	e,n	Davis et al. (2022)
NGC5064	34.0	No	Sb	-	10.93	z0MGS	0.11	e,g	Davis et al. (2022)
NGC5765b	114.0	No	SABb	Seyfert 2	11.21	M_{K_s}	1.43	j	Davis et al. (2022)
NGC5806	21.4	Yes	Sb	Seyfert 2	10.57	z0MGS	-0.03	d,e	Davis et al. (2022)
NGC5995	107.5	No	SABa	Seyfert 2	11.41	M_{K_s}	-	b	This work
NGC6753	42.0	No	Sb	-	10.78	z0MGS	0.32	e,g	Davis et al. (2022)
NGC6958	30.6	No	E	-	10.76	z0MGS	-0.58	e,g	Thater, in prep
NGC7052	51.6	Yes	E	LERG^1	11.75	MASSIVE	-0.07	a,l	Smith et al. (2021b)
NGC7172	33.9	No	Sa	Seyfert 2	10.76	z0MGS	0.38	m	Davis et al. (2022)
PGC043387	95.8	No	E	-	11.12	M_{K_s}	-0.48	i	This work

Notes: (1) galaxy name, (2) galaxy distance in Mpc, (3) whether a resolved radio jet is present in radio observations of the galaxy, (4) galaxy morphological type, (5) AGN type or HERG/LERG classification (determined using classification from Figure 2 of Best & Heckman 2012). The radio AGN classification of NGC7052 was taken from Gleisinger et al. (2020). (6) galaxy stellar mass, (7) the reference for the stellar mass: L22 refers Lelli et al. (2022), C17 refers to Cook et al. (2017), S10 refers to Seth et al. (2010), A3D refers to Cappellari et al. (2013b), MASSIVE refers to Veale et al. (2017), and z0MGS to Leroy et al. (2019). M_{K_s} refers to masses estimated from the galaxies K_s-band magnitude using Equation 2 of Cappellari (2013). (8) the star formation rate of the galaxy. The uncertainties on the star formation rates are 0.2 dex for all sources except NGC0404, NGC1194 and PGC043387 which have uncertainties of 0.22, 0.87 and 0.22 dex respectively. ^{2} represents galaxies where the star formation rate was estimated in this work. (9) ALMA Project codes of each source, where a: 2016.2.00046.S, b: 2017.1.00904.S, c: 2015.1.00419.S, d: 2016.1.00437.S, e: 2016.2.00053.S, f: 2017.1.00572.S, g: 2015.1.00466.S, h: 2017.1.00391.S, i: 2015.1.00598.S, j: 2016.1.01553.S, k: 2016.1.00839.S, l: 2018.1.00397.S, m: 2019.1.00363.S and n: 2013.1.00493. (10) reference where the ALMA data were initially presented.

target multiple ALMA observations were used with multiple array configurations. This enabled the observations to reach high angular resolution, while ensuring adequate uv-plane coverage and excellent flux recovery. The spectral configuration always consisted of four spectral windows (SPWs), one centred on the redshifted frequency of the ^{12}CO line (rest frequency 230.5 GHz for the 2–1 transition, 345.8 GHz for 3–2). The other three SPWs were used to observe the continuum. ALMA data were reduced using the Common Astronomy Software Applications (CASA) pipeline (McMullin et al., 2007) version appropriate for each dataset. A standard calibration strategy was adopted for every observation. A single bright object (typically a quasar) was used as both flux and bandpass calibrator, while a second bright object was used as a phase calibrator. More details on the data reduction process can be found in Davis et al. (2022).

Line imaging

In this work I make use of the CO data cubes presented in Davis et al. (2022), or used the same cleaning methods described therein for consistency. The final cleaned cubes have synthesised beam sizes ranging from 0″.054 to 0″.659, corresponding to spatial scales from 0.8 to 291 pc, and noise levels ranging from 0.19 $\mathrm{mJy\ beam^{-1}}$ to 3.70 $\mathrm{mJy\ beam^{-1}}$. Since I am interested only in the gas reservoirs on scales $\lesssim 100$ pc (i.e. those relevant for the SMBH accretion process), I restrict my analysis to the sub-sample of 29 WISDOM galaxies whose ALMA data cubes satisfy such spatial resolution requirement.

2.2.3 ANCILLARY DATA

I gathered a variety of ancillary data to assess the level of nuclear activity in my targets and test its connection with the cold gas reservoirs observed with ALMA. For each source, I thus retrieved 2–10 keV X-ray, 1.4 GHz radio continuum and optical [OIII]λ5007 luminosities from the NASA Extragalactic Database (NED)[*] or other literature sources.

All the ancillary observations used in this work are listed in Table 2.2. In the following, I briefly describe each set of ancillary data and caveats around their use.

X-ray data

I retrieved the nuclear 2–10 keV X-ray luminosities ($L_{X,2-10}$) of the majority of my sources from Bi et al. (2020), who presented a catalogue of nearby galaxies observed with *Chandra*.

---

[*] `https://ned.ipac.caltech.edu/`

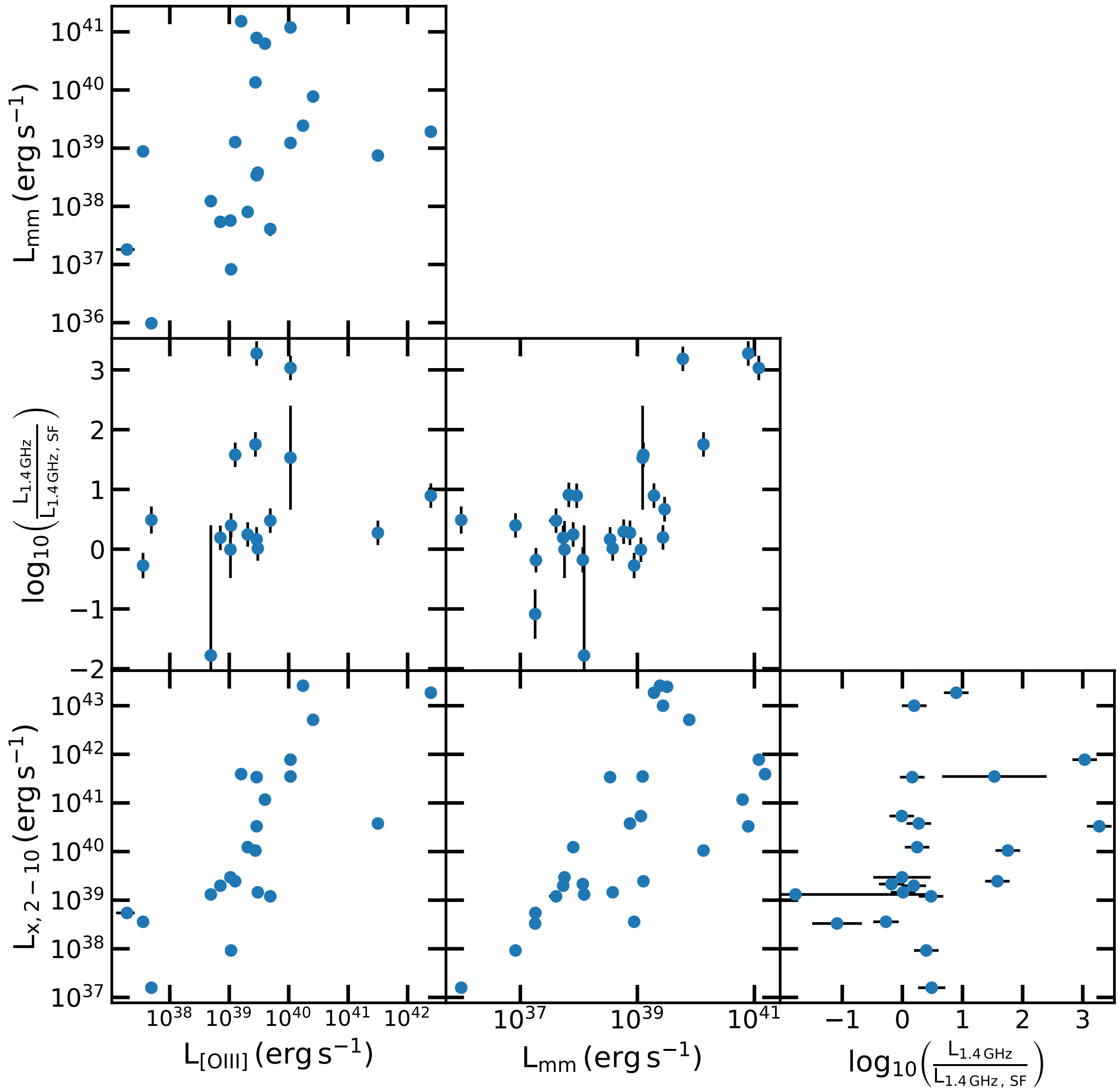

Figure 2.2: Correlations between the nuclear mm continuum luminosity, excess 1.4 GHz factor, 2–10 keV luminosity and the [OIII] luminosity. The Spearman rank coefficients and *p*-value of these correlations are listed in Table 2.6.

Table 2.2: Emission data

Galaxy (1)	$L_{1.4}$ $(\mathrm{erg\,s^{-1}})$ (2)	$\Delta L_{1.4}$ $(\mathrm{erg\,s^{-1}})$ (3)	$E_{1.4}$ (4)	$\Delta E_{\ 1.4}$ (5)	$L_{\mathrm{X,2\text{-}10}}$ $(\ \mathrm{erg\,s^{-1}})$ (6)	$\Delta L_{\mathrm{X,2\text{-}10}}$ $(\mathrm{erg\,s^{-1}})$ (7)	X-ray Source (8)	L_{mm} $(\mathrm{erg\,s^{-1}})$ (9)	ΔL_{mm} $(\mathrm{erg\,s^{-1}})$ (10)	$\log_{10}\left(\frac{L_{[\mathrm{OIII}]}}{\mathrm{erg\,s^{-1}}}\right)$ (11)	$\log_{10}\left(\frac{\Delta L_{[\mathrm{OIII}]}}{\mathrm{erg\,s^{-1}}}\right)$ (12)	K_{s} (mag) (13)	ΔK_{s} (mag) (14)
FRL49	9.06E+38	9.06E+37	0.90	0.205	1.85E+43	1.85E+42	Chandra	1.92E+39	7.85E+37	42.39	0.04	9.8	0.0100
FRL1146	-	-	-	-	2.58E+43	2.58E+42	XMM	2.44E+39	1.41E+38	40.24	0.07	11	0.00800
MRK567	7.48E+38	7.91E+37	0.29	0.205	-	-	-	5.84E+38	-	-	-	11	0.0450
NGC0383	3.59E+40	3.59E+39	3.3	0.205	3.31E+40	3.31E+39	Chandra	7.86E+40	1.26E+38	39.46	0.04	10	0.00700
NGC0404	5.36E+34	6.99E+33	0.49	0.227	1.58E+37	1.58E+36	Chandra	9.76E+35	3.08E+34	37.69	0.04	10	0.00700
NGC0449	5.55E+38	5.78E+37	0.27	0.205	3.78E+40	3.78E+39	XMM	7.47E+38	3.05E+37	41.50	0.04	12	0.0230
NGC0524	2.80E+36	4.61E+35	-0.27	0.212	3.59E+38	3.59E+37	Chandra	8.81E+38	3.56E+36	37.55	0.04	10	0.0730
NGC0612	1.46E+41	1.47E+40	3.0	0.205	7.76E+41	7.76E+40	Chandra	1.19E+41	2.84E+38	40.03	0.04	9.9	0.0990
NGC0708	3.72E+38	3.72E+37	1.6	0.205	2.45E+39	2.45E+38	Chandra	1.27E+39	1.58E+37	39.10	0.04	12	0.0600
NGC1194	1.18E+37	1.18E+36	1.5	0.871	3.50E+41	3.50E+40	XMM	1.23E+39	2.22E+37	40.03	0.04	11	0.0320
NGC1387	2.64E+36	4.22E+35	-0.18	0.212	2.14E+39	2.14E+38	Chandra	1.17E+38	6.03E+36	-	-	10	0.111
NGC1574	-	-	-	-	-	-	-	3.52E+38	3.50E+36	-	-	10	0.0980
NGC2110	6.34E+38	6.76E+37	-	-	5.13E+42	5.13E+41	Chandra	7.72E+39	1.64E+38	40.41	0.04	10	0.0580
NGC3169	5.43E+37	5.43E+36	0.16	0.205	3.39E+41	3.39E+40	Chandra	3.42E+38	1.07E+37	39.46	0.04	10	0.0920
NGC3351	7.08E+36	7.08E+35	-	-	5.46E+38	5.67E+37	ROSAT	1.81E+37	-	37.28	0.15	9.0	0.0150
NGC3368	1.52E+37	1.52E+36	0.19	0.205	1.98E+39	1.98E+38	ASCA	5.40E+37	-	38.85	0.04	9.5	0.0680
NGC3607	5.67E+36	6.57E+35	0.010	0.206	1.45E+39	1.45E+38	Chandra	3.79E+38	2.31E+37	39.48	0.04	9.5	0.0420
NGC3862	8.13E+40	8.13E+39	-	-	3.92E+41	3.92E+40	Chandra	1.52E+41	3.43E+39	39.20	0.04	11	0.0370
NGC4061	5.70E+39	5.70E+38	3.2	0.205	-	-	-	5.98E+39	4.46E+38	-	-	11	0.0400
NGC4261	3.74E+40	4.12E+39	-	-	1.17E+41	1.17E+40	Chandra	6.28E+40	4.43E+38	39.60	0.04	9.0	0.0150
NGC4429	4.59E+34	2.30E+35	-1.8	2.18	1.31E+39	1.31E+38	Einstein	1.23E+38	9.42E+36	38.69	0.04	10	0.0650
NGC4435	2.72E+36	2.72E+36	-0.010	0.478	2.95E+39	2.95E+38	Chandra	5.69E+37	1.92E+36	39.02	0.04	10	0.0590
NGC4438	2.87E+37	2.87E+36	0.48	0.205	1.20E+39	1.20E+38	Chandra	4.08E+37	9.81E+36	39.69	0.04	8.8	0.0150
NGC4501	9.05E+37	9.05E+36	0.25	0.205	1.23E+40	1.23E+39	Chandra	8.01E+37	4.39E+36	39.31	0.04	9.0	0.0150
NGC4697	1.30E+35	1.08E+35	-1.1	0.413	3.31E+38	3.31E+37	Chandra	1.79E+37	1.65E+36	-	-	9.7	0.0660
NGC4826	9.30E+36	9.03E+35	0.40	0.204	9.23E+37	2.05E+37	Chandra	8.27E+36	1.64E+36	39.03	0.04	8.0	0.0150
NGC5064	1.93E+38	1.93E+37	0.89	0.205	-	-	-	9.19E+37	8.53E+36	-	-	11	0.0730
NGC5765b	5.03E+38	5.03E+37	-0.010	0.205	5.37E+40	5.37E+39	Chandra	1.15E+39	2.17E+38	-	-	10.9	0.0700
NGC5806	1.17E+37	1.17E+36	-0.18	0.205	-	-	-	1.85E+37	-	-	-	11	0.0730
NGC5995	5.91E+38	6.36E+37	-	-	2.45E+43	2.45E+42	Chandra	3.22E+39	1.07E+38	-	-	10	0.0390
NGC6753	3.23E+38	3.53E+37	0.91	0.205	-	-	-	6.73E+37	-	-	-	11	0.0990
NGC6958	2.34E+37	2.81E+36	0.67	0.207	-	-	-	2.92E+39	1.51E+37	-	-	10	0.0600
NGC7052	9.21E+38	9.30E+37	1.8	0.205	1.05E+40	1.05E+39	Chandra	1.35E+40	6.23E+37	39.44	0.04	11	0.0420
NGC7172	7.20E+37	7.66E+36	0.20	0.205	1.00E+43	1.00E+42	Chandra	2.74E+39	1.04E+38	-	-	10	0.0560
PGC043387	-	-	-	-	-	-	-	8.02E+38	-	-	-	10.7	0.0110

Notes: (1) Galaxy name, (2) 1.4GHz luminosity, (3) 1.4GHz luminosity uncertainty, (4) Excess radio fraction, (5) Excess radio fraction uncertainty, (6) 2-10 keV X-ray luminosity, (7) (2-10) keV X-ray luminosity uncertainty, (8) The telescope used for the X-ray observation, (9) Nuclear mm luminosity, (10) Nuclear mm luminosity uncertainty, (11) [OIII] luminosity, (12) [OIII] luminosity uncertainty, (13) K_{s}-band magnitude, (14) K_{s}-band magnitude uncertainty.

Ten sample galaxies are not included in this catalogue[†], thus their X-ray data was gathered from NED and comes from a variety of satellites, i.e. Röntgensatellit (*ROSAT*), *EINSTEIN*, Advanced Satellite for Cosmology and Astrophysics (*ASCA*), XMM-*Newton* and *Chandra* (see Table 2.2). For four (NGC3351, NGC3862, NGC4429 and NGC4826) of these ten galaxies, 2–10 keV luminosities were not available, thus I scaled the available measurement (0.2–2 keV for NGC3351 and NGC4429, 0.3–8 keV for NGC3862 and NGC4826) to the 2–10 keV energy band using a power law with an index -0.8 (corresponding to the mean reported by Reeves & Turner 2000). Eight sample galaxies do not have any X-ray data available.

Thanks to the exquisite *Chandra* resolution ($\approx\ 0.5''$ on-axis) and the efforts by the authors to remove as much contamination as possible, the nuclear 2–10 keV luminosities from Bi et al. (2020) are expected to trace only emission from the unresolved AGN core (although some negligible contamination from unresolved nuclear X-ray sources may still occur). In the other ten cases, the spatial resolution of the available X-ray observations does not allow to distinguish between nuclear AGN emission and other types of contribution on larger galaxy scales, thus possible sources of contamination need to be considered.

[†] FRL49, FRL1146, NGC0449,NGC0524, NGC1194, NGC3351, NGC3368, NGC3862, NGC4429 and NGC4826

This includes emission from the diffuse hot atmospheres in and around galaxies (i.e. the circumgalactic medium, CGM). This low-surface brightness emission, however, usually requires very deep X-ray observations to be detected, and is typically dominant in the softer (0.3–2 keV) energy range. As such, I expect CGM contamination to be minimal even in low-resolution 2–10 keV X-ray data. A relatively larger contribution from the CGM may still be present in faint X-ray sources and in the four cases in which the 2–10 keV luminosities was extrapolated from lower energy bands.

Stellar X-ray binaries are another potential source of contamination. The K-band luminosity has been demonstrated to correlate with the luminosity of low mass X-ray binaries (LMXB). I thus use the K_s-band flux to estimate the contribution of LMXB to the 2–10 keV emission using the relations from Kim & Fabbiano (2004) and Boroson et al. (2011). I find that in three of the ten galaxies for which *Chandra* data was not available from Bi et al. (2020) the contributions from LMXBs is minimal (<5%). In the other seven galaxies (NGC0449, NGC0524, NGC3351, NGC3368, NGC3862, NGC4429 and NGC4826) the contribution expected is up to 43%. To estimate the potential contamination from high mass X-ray binaries (HMXB) I used the relation between SFR and X-ray luminosity from Grimm et al. (2003). In this case, I find three galaxies have minimal contributions (<5%), six (NGC0449, NGC0524, NGC3368, NGC3351, NGC4429 and NGC4826) have larger contributions up to 73%, and one (FRL1146) where I do not have information on the SFR I could not calculate the contributions from HMXB. I therefore assume that the 2-10 keV luminosity of most of my targets is dominated by AGN emission from the core. In few individual sources, however, it is possible that I slightly overestimate the AGN luminosity due to the aforementioned uncertainties.

Radio data

I used 1.4 GHz radio observations to probe the type of nuclear activity, and the presence of radio jets in my sources. The data used in this work are mostly from the Very Large Array sky surveys, such as the Faint Images of the Radio Sky at Twenty-Centimeters (FIRST; Becker et al., 1994), and the NRAO VLA Sky Survey (NVSS; Condon et al., 1998). The spatial resolution of these surveys is typically very poor (e.g. $45''$ for the NVSS). While this does not allow me to resolve nuclear radio structures, it does ensures that no radio emission is resolved out and that any associated large-scale radio jet is detected. For the one source (NGC1574) for which 1.4 GHz observations were not available, I scaled the available 5GHz radio data to 1.4 GHz using a power law with a spectral index $\alpha = -0.8$ (for $S \propto \nu^{\alpha}$), as typical for optically-thin radio jet emission (e.g. Komissarov & Gubanov, 1994;

Laing & Bridle, 2013).

It is possible that some of the radio emission detected in my targets is contaminated by star formation within the galaxy (e.g. from supernova remnants). To quantify such putative contribution, I gathered the star formation rates (SFRs) of my sample sources from Davis et al. (2022), when available, as before. For the 6 sample galaxies not included in that work, I estimated the SFRs adopting the following relation:

$$\mathrm{SFR} = \frac{M_{\mathrm{H}_2}}{\tau} \tag{2.1}$$

where M_{H_2} is the total molecular gas mass within the galaxy (calculated as described in Section 2.3.1), and τ is the depletion time, assumed to be 2 Gyr (e.g Leroy et al., 2008). I then estimated the expected 1.4 GHz radio luminosity due to star formation using the following relation (Murphy et al., 2011):

$$\left(\frac{\mathrm{SFR}_\nu}{\mathrm{M}_\odot yr^{-1}}\right) = 10^{-27}\left[2.18\left(\frac{T_e}{10^4 K}\right)^{0.45}\left(\frac{\nu}{\mathrm{GHz}}\right)^{-0.1} + 15.1 \left(\frac{\nu}{\mathrm{GHz}}\right)^{\alpha^{NT}}\right]^{-1}\left(\frac{L_\nu}{\mathrm{erg\,s^{-1}Hz^{-1}}}\right), \tag{2.2}$$

which can be rearranged to:

$$\left(\frac{L_\nu}{\mathrm{erg\,s^{-1}Hz^{-1}}}\right) = 10^{27}\left(\frac{\mathrm{SFR}_\nu}{\mathrm{M_\odot yr^{-1}}}\right)\left[2.18\left(\frac{T_e}{10^4 K}\right)^{0.45}\left(\frac{\nu}{\mathrm{GHz}}\right)^{-0.1} + 15.1\left(\frac{\nu}{\mathrm{GHz}}\right)^{\alpha^{\mathrm{NT}}}\right] \tag{2.3}$$

where ν is the observed frequency, T_e is the electron temperature and α^{NT} is the non-thermal spectral index. I assumed $T_e = 10^4$ K (Murphy et al., 2011) and $\alpha = -0.8$ (Murphy et al., 2011). The relation combines thermal radio emission (calculated from the ionizing photon production rate) and non-thermal radio emission from supernovae, both of which are related directly to the SFR.

From the ratio between the total radio luminosity and that expected from star formation, $\log_{10}(L_{1.4\mathrm{GHz}}/L_{\ 1.4\mathrm{GHz,\ SF}})$, I calculate what I call the radio excess factor ($E_{1.4}$). In galaxies with $E_{1.4}$ significantly larger than zero, the detected radio emission cannot be explained by star formation, and thus likely arises from nuclear activity. The radio excess factor for each galaxy is tabulated in Table 2.2.

Optical line data

[O III]λ5007 is typically the strongest emission line in optical spectra of AGN and arises from gas in the narrow line regions (NLRs) that has been photo-ionised by the AGN radiation. It is then usually considered as a good proxy of the AGN bolometric luminosity (e.g. Heckman & Best, 2014). [O III] has also the advantage to be a more ubiquitous tracer of nuclear activity than the 2-10 keV luminosity, as it is observed in both kinetic- and radiative-mode AGN and does not suffer from obscuration from a dusty torus that may be present (such as that in typical Seyfert-like objects) though it may still suffer from obscuration from dust in the galaxy at larger scales. I therefore collected [OIII]λ5007 luminosities from a variety of instruments/surveys, such as the double spectrograph at the *Hale Telescope* (Ho et al., 1995), *El Leoncito Astronomical Complex* (CASLEO; Bonatto & Pastoriza, 1997; Rodríguez-Ardila et al., 2000), the DOLORES (Device Optimized for the LOw RESolution) spectrograph at *Galileo National Telescope* (TNG; Buttiglione et al., 2009), *Sloan Digital Sky Survey* (SDSS; Zhu et al., 2011), *MPG/ESO telescope* (Tadhunter et al., 1993), the spectrograph on the *Shane Telescope* at Lick Observatory (De Robertis & Osterbrock, 1986; Crawford et al., 1999) and the *CTIO Telescope* (Moustakas et al., 2010). I note that the [OIII]λ5007 line may be contaminated by star formation or old stars, or be affected by extinction arising within the host galaxy. However, star formation is only expected to contribute significantly in higher-redshift galaxies (whereas it should be negligible in nearby objects such as my sample sources; Suzuki et al., 2016). Where available, I additionally gathered Hβ, [N II]λ6583 and Hα luminosities. These are useful to calculate the [OIII]/Hβ and [NII]/Hα ratios which I can use to construct the BPT diagrams of my objects, and thus assess their dominant excitation mechanism (e.g. Baldwin et al., 1981; Kewley et al., 2006). Eighteen of my sample galaxies have all the lines required to construct a BPT diagram, showing that 5 sources fall in the AGN-dominated region (FRL49, NGC0612,NGC1194,NGC2110, NGC5765b), 4 in the LINER region (NGC3368, NGC3862, NGC5995, NGC6753), 8 in the composite region (NGC1387, NGC3351, NGC4061, NGC4261, NGC4826, NGC5064, NGC7172, PGC043387) and 1 (MRK567) in the SF-dominated region. The log([OIII]/Hβ) ratios for 9 other galaxies (FRL1146, NGC0404, NGC0524, NGC3169, NGC3607, NGC4429, NGC4435, NGC4438, NGC4501) have values ranging from -0.44 to 0.71. Depending on their unknown log([NII]/Hα) ratios, they could thus be placed in the star formation, composite, LINER regions or AGN regions.

ALMA nuclear continuum emission

I gathered the ALMA nuclear continuum luminosities from Ruffa et al. (2024), with the mm continuum flux which have been measured from the innermost beam at the position of the AGN in the ALMA continuum map of each galaxy.

Accretion tracer correlations

The correlations between the nuclear mm luminosity, X-ray luminosity, [OIII] luminosity and excess radio factor are shown in Figure 2.2, with the correlation coefficients and p-values listed in Table 2.6. This figure shows that the four tracers of activity mostly correlate with each other despite different contaminants, suggesting I am tracing nuclear activity rather then larger scale emission. This also shows that, even though some of the galaxies in my sample are not formally classified as AGN, low-level nuclear activity seems to be present.

Stellar masses

The stellar masses of the majority of my sample galaxies were taken from Davis et al. (2022), who in turn collected them from the ATLAS^{3D} (Cappellari et al., 2013b) and MASSIVE (Veale et al., 2017) surveys, and the z=0 Multiwavelength Galaxy Synthesis (z0MGS) project (Leroy et al., 2019). The stellar masses for MRK 567 and NGC 0404 were taken from Cook et al. (2017) and Seth et al. (2010), respectively. Where stellar mass measurements were not available in the literature, I estimated them from the K_s-band magnitudes measured in the extended source catalogue of the 2 micron All-Sky Survey (2MASS; Jarrett et al., 2003). I used Equation 2 of Cappellari (2013), with no correction for the emission from the AGN (as this should be small at these frequencies in my low-luminosity sources):

$$\log_{10} M_* \approx 10.58 - 0.44 \times (M_{K_s} + 23) \tag{2.4}$$

where M_* is the stellar mass and M_{K_s} is the K_s-band magnitude.

2.3 METHODOLOGY AND DERIVED QUANTITIES

In this work I search for correlations between *circumnuclear* molecular gas reservoirs and SMBH fuelling across a sample of galaxies with a range of nuclear activities. This requires me to assess both the amount of molecular gas present in the circumnuclear

Table 2.3: CO integrated intensity data

Galaxy	$I_{\rm CO}$	$\Delta I_{\rm CO}$	$I_{\rm CO}$	$\Delta I_{\rm CO}$	$I_{\rm CO}$	$\Delta I_{\rm CO}$	$I_{\rm CO}$	$\Delta I_{\rm CO}$
	(200 pc)		(100 pc)		(75 pc)		(50 pc)	
	$({\rm Jy\,km\ s^{-1}})$	$({\rm Jy\,km\ s^{-1}})$	$({\rm Jy\,km\ s^{-1}})$	$({\rm Jy\,km\,s^{-1}})$	$({\rm Jy\,km\,s^{-1}})$	$({\rm Jy\,km\,s^{-1}})$	$({\rm Jy\,km\,s^{-1}})$	$({\rm Jy\,km\,s^{-1}})$
(1)	(2)	(3)	(4)	(5)	(6)	(7)	(8)	(9)
FRL49	7.75	0.78	2.39	0.24	-	-	-	-
FRL1146	-	-	-	-	-	-	-	-
MRK567	9.58	0.96	3.98	0.4	-	-	-	-
NGC0383	7.60	0.76	2.74	0.27	1.6	0.16	0.64	0.06
NGC0404	39.62	3.96	39.73	3.97	39.07	3.91	36.14	3.61
NGC0449	-	-	-	-	-	-	-	-
NGC0524	11.64	1.16	3.77	0.38	2.48	0.25	1.29	0.13
NGC0612	2.22	0.22	0.58	0.06	0.44	0.05	0.32	0.04
NGC0708	9.24	0.92	3.18	0.32	2.05	0.21	0.95	0.1
NGC1194	2.58	0.26	1.13	0.11	0.76	0.08	-	-
NGC1387	27.95	2.80	6.8	0.68	3.78	0.38	1.62	0.16
NGC1574	3.98	0.40	3.53	0.35	2.89	0.29	1.6	0.16
NGC2110	4.62	0.46	1.21	0.12	-	-	-	-
NGC3169	125.84	12.58	43.18	4.32	26.99	2.7	-	-
NGC3351	104.99	10.50	55.74	5.57	32.78	3.28	18.57	1.86
NGC3368	170.74	17.07	54.79	5.48	35.54	3.55	19.23	1.92
NGC3607	37.39	3.74	15.56	1.56	10.37	1.04	-	-
NGC3862	-	-	-	-	-	-	-	-
NGC4061	1.21	0.12	0.34	0.03	0.21	0.02	-	-
NGC4261	5.91	0.59	5.49	0.55	4.59	0.46	2.98	0.3
NGC4429	17.38	1.74	3.64	0.36	2	0.2	0.64	0.06
NGC4435	35.67	3.57	15.68	1.57	9.91	0.99	5.28	0.53
NGC4438	134.20	13.42	52.63	5.26	32.86	3.29	15.26	1.53
NGC4501	137.79	13.78	63.66	6.37	40.61	4.06	20.26	2.03
NGC4697	1.90	0.19	1.55	0.16	1.23	0.12	0.74	0.07
NGC4826	276.92	27.69	193.02	19.3	148.73	14.87	74.96	7.5
NGC5064	27.91	2.79	9.7	0.97	5.27	0.53	2.58	0.26
NGC5765b	4.70	0.47	-	-	-	-	-	-
NGC5806	19.20	1.92	7.53	0.75	5.46	0.55	3.09	0.31
NGC5995	-	-	-	-	-	-	-	-
NGC6753	57.58	5.76	19.66	1.97	11.8	1.18	5.65	0.56
NGC6958	12.76	1.28	3.76	0.38	2.3	0.23	1.03	0.11
NGC7052	5.06	0.51	2.2	0.22	1.33	0.13	0.55	0.06
NGC7172	47.03	4.70	6.19	0.62	2.85	0.29	1.14	0.11
PGC043387	-	-	-	-	-	-	-	-

Notes: (1) Galaxy name. (2) 200pc radius aperture integrated CO intensity. (3) 200pc aperture CO intensity uncertainty. (4)-(9) follows the same trend for the 100, 75 and 50 pc radius apertures.

regions, and its structure. Furthermore, I need to constrain the SMBH accretion rate in my sources, and the type of nuclear activity. Below I describe the methodology I adopted to determine these quantities.

2.3.1 MOLECULAR GAS MASSES

I adopt the following relation to estimate the molecular hydrogen gas masses ($M_{\rm H_2}$) of my galaxies within different apertures (Bolatto et al., 2013):

$$M_{\rm H_2} = 2{\rm m}_H \frac{\lambda^2}{2k_{\rm B}} X_{\rm CO} D_{\rm L}^2 R \int S_\nu \, dV, \tag{2.5}$$

where $\mathrm{m_H}$ is the mass of the hydrogen atom, λ is the rest wavelength of the observed molecular transition, k_{B} is the Boltzmann constant, X_{CO} is the CO-to-$\mathrm{H_2}$ conversion factor, D_{L} is the luminosity distance, $R \equiv T_{\mathrm{b,ref}}/T_{\mathrm{b,CO(1\text{-}0)}}$ is the line intensity ratio (i.e. the ratio between the ground state and the observed CO line brightness temperature), and $\int S_{\mathrm{v}} dV$ is the integrated flux density of the CO(1-0) line, with units matching those of X_{CO}. This was estimated by integrating the spectrum of the observed CO transition within a given aperture over all the velocity channels of the line. Equation 2.5 can be simplified to

$$\left(\frac{M_{\mathrm{H_2}}}{\mathrm{M_\odot}}\right) = 7847\, J_{\mathrm{upper}}^{-2} X_{\ \mathrm{CO},2\times10^{20}} R \left(\frac{D_{\mathrm{L}}}{\mathrm{Mpc}}\right)^2 \left(\frac{\int S_{\mathrm{v}} dV}{\mathrm{Jy\ kms^{-1}}}\right), \tag{2.6}$$

where J_{upper} is the upper state rotational quantum number of the observed transition (here J_{upper} is 2 or 3) and $X_{\mathrm{CO},2\times10^{20}}$=$\frac{X_{\mathrm{CO}}}{2\times10^{20}\ \mathrm{cm^{-2}(K\ km\ s^{-1})^{-1}}}$. As most of my galaxies are massive and metal-rich, I assume a Milky Way-like CO-to-$\mathrm{H_2}$ conversion factor of $3\times10^{20}\mathrm{cm^{-2}(K\ km\ s^{-1})^{-1}}$ (Strong et al., 1988). I also assume the line ratios to be $T_{\mathrm{b,CO(2-1)}}/T_{\mathrm{b,CO(1-0)}} = 0.7$ and $T_{\ \mathrm{b,CO(3-2)}}/T_{\mathrm{b,CO(1-0)}} = 0.3$ (see e.g. Leroy et al., 2022). For sample galaxies observed with ALMA at adequate spatial resolutions, I estimated the molecular gas mass within three different elliptical apertures of radii 100, 75, and 50 pc matching observed structure. I additionally measure the molecular gas mass in a elliptical aperture with a radius of 200 pc to measure the nuclear molecular gas concentration. The resulting $\mathrm{M_{H_2}}$ are listed in Table 2.4. As mentioned above, the molecular gas masses were all calculated with a fixed $\mathrm{X_{CO}}$ factor. I note, however, that the CO-to-$\mathrm{H_2}$ conversion factors in galaxy centres may vary (Sandstrom et al., 2013), adding uncertainty at a ~0.3 dex level. To aid comparisons with different X_{CO} prescriptions, I provide the CO integrated flux densities measured within the different apertures in Table 2.3. I assume an additional 10% error on my molecular gas masses due to ALMA calibration uncertainties.

To assess the structure of the molecular gas at the centre of each sample galaxy, following García-Burillo et al. (2021), I also calculated the molecular concentration parameter:

$$\frac{\Sigma_{\mathrm{H_2}}^{\mathrm{50pc}}}{\Sigma_{\mathrm{H_2}}^{\mathrm{200pc}}} = 16\left(\frac{M_{\mathrm{H_2}}^{\mathrm{50pc}}}{M_{\mathrm{H_2}}^{\mathrm{200pc}}}\right), \tag{2.7}$$

where $\Sigma_{\mathrm{H_2}}^{x\mathrm{pc}}$ and $M_{\mathrm{H_2}}^{x\mathrm{pc}}$ are the molecular gas surface density and mass, respectively, within a elliptical aperture of radius x pc. I assumed that the gas lies within a flat disk so $\Sigma_{\mathrm{H_2}}^{x\mathrm{pc}}$=$\frac{M_{\mathrm{H_2}}^{x\mathrm{pc}}}{\pi x^2}$.

Table 2.4: Circumnuclear masses for different region sizes.

Galaxy	log $\left(\frac{M_{\mathrm{H}_2}}{\mathrm{M}_\odot}\right)$	Δlog $\mathrm{M}_{\mathrm{H}_2}$	log $\left(\frac{M_{\mathrm{H}_2}}{\mathrm{M}_\odot}\right)$	Δlog $\mathrm{M}_{\mathrm{H}_2}$	log $\left(\frac{M_{\mathrm{H}_2}}{\mathrm{M}_\odot}\right)$	Δlog $\mathrm{M}_{\mathrm{H}_2}$	log $\left(\frac{M_{\mathrm{H}_2}}{\mathrm{M}_\odot}\right)$	Δlog $\mathrm{M}_{\mathrm{H}_2}$	$\mathrm{S}_{\nu,\mathrm{mm}}$	$\sigma\mathrm{S}_{\nu,\mathrm{mm}}$
	(200 pc)		(100 pc)		(75 pc)		(50 pc)			
		(dex)		(dex)		(dex)		(dex)	(mJy)	(mJy)
(1)	(2)	(3)	(4)	(5)	(6)	(7)	(8)	(9)	(10)	(11)
FRL49	8.34	0.04	7.87	0.04	-	-	-	-	0.93	0.038
FRL1146	-	-	-	-	-	-	-	-	0.47	0.0272
MRK567	8.90	0.04	8.52	0.04	-	-	-	-	<0.11	0.0354
NGC0383	8.15	0.04	7.71	0.04	7.48	0.04	7.08	0.04	63	0.101
NGC0404	6.18	0.04	6.18	0.04	6.17	0.04	6.14	0.04	0.38	0.012
NGC0449	-	-	-	-	-	-	-	-	0.60	0.0246
NGC0524	7.42	0.04	6.93	0.05	6.75	0.04	6.47	0.04	5.7	0.023
NGC0612	8.20	0.04	7.62	0.04	7.50	0.04	7.35	0.05	25	0.06
NGC0708	8.12	0.04	7.66	0.04	7.47	0.04	7.13	0.05	1.3	0.0165
NGC1194	7.48	0.04	7.13	0.04	6.95	0.05	-	-	1.6	0.0286
NGC1387	7.66	0.04	7.05	0.04	6.80	0.04	6.43	0.04	1.0	0.0535
NGC1574	6.79	0.04	6.74	0.04	6.66	0.04	6.40	0.04	3.3	0.033
NGC2110	7.35	0.04	6.77	0.04	-	-	-	-	21	0.453
NGC3169	8.26	0.04	7.80	0.04	7.60	0.04	-	-	3.4	0.107
NGC3351	7.66	0.04	7.39	0.04	7.16	0.04	6.91	0.04	<0.45	0.148
NGC3368	8.36	0.04	7.87	0.04	7.68	0.05	7.42	0.04	<0.56	0.202
NGC3607	7.89	0.04	7.51	0.04	7.33	0.04	-	-	2.7	0.164
NGC3862	-	-	-	-	-	-	-	-	64	1.43
NGC4061	7.65	0.04	7.10	0.04	6.90	0.04	-	-	2.4	0.18
NGC4261	7.32	0.04	7.29	0.04	7.21	0.04	7.02	0.04	220	1.53
NGC4429	7.31	0.04	6.64	0.04	6.38	0.04	5.88	0.04	1.1	0.0853
NGC4435	7.61	0.04	7.25	0.04	7.05	0.05	6.78	0.04	0.73	0.0246
NGC4438	8.19	0.04	7.78	0.04	7.58	0.04	7.24	0.04	0.52	0.126
NGC4501	8.06	0.04	7.72	0.04	7.52	0.05	7.22	0.04	1.4	0.0789
NGC4697	6.02	0.04	5.93	0.04	5.83	0.04	5.61	0.04	0.48	0.0444
NGC4826	7.66	0.04	7.55	0.04	7.25	0.04	7.60	0.04	0.38	0.0746
NGC5064	8.13	0.04	7.67	0.04	7.41	0.04	7.10	0.04	0.28	0.0259
NGC5765b	8.41	0.04	-	-	-	-	-	-	0.328	0.0616
NGC5806	7.57	0.04	7.16	0.04	7.02	0.04	6.77	0.05	<0.14	0.0473
NGC5995	-	-	-	-	-	-	-	-	0.99	0.0331
NGC6753	8.63	0.04	8.16	0.05	7.94	0.04	7.62	0.04	<0.14	0.0447
NGC6958	7.70	0.04	7.17	0.04	6.96	0.04	6.61	0.04	11	0.0569
NGC7052	7.75	0.04	7.39	0.04	7.17	0.04	6.79	0.04	18	0.0823
NGC7172	8.36	0.04	7.48	0.04	7.14	0.04	6.74	0.04	8.4	0.32
PGC043387	-	-	-	-	-	-	-	-	<0.31	0.104

Notes: (1) galaxy name. (2) mass measured within a elliptical aperture of 200 pc radius, with its uncertainty in (3). (4)-(9) follow the same pattern, for 100, 75 and 50 pc apertures. (10) nuclear mm continuum flux derived from all my ALMA data, (11) nuclear mm continuum flux uncertainty.

Table 2.5: Derived quantities

Galaxy (1)	$\dot{M}_{\text{X-ray,acc}}$ $(\mathrm{M_\odot\,yr^{-1}})$ (2)	$\Delta\dot{M}_{\text{X-ray,acc}}$ $(\mathrm{M_\odot\,yr^{-1}})$ (3)	$\dot{M}_{\text{[OIII],acc}}$ $(\mathrm{M_\odot\,yr^{-1}})$ (4)	$\Delta\dot{M}_{\text{[OIII],acc}}$ $(\mathrm{M_\odot\,yr^{-1}})$ (5)
FRL49	5.70E-02	5.70E-03	1.29E+00	1.19E-01
FRL1146	8.70E-02	8.70E-03	9.12E-03	1.47E-03
MRK567	-	-	-	-
NGC0383	3.55E-05	3.55E-06	1.51E-03	1.39E-04
NGC0404	2.50E-08	2.50E-09	2.57E-05	2.37E-06
NGC0449	4.10E-05	4.10E-06	1.66E-01	1.53E-02
NGC0524	3.98E-07	3.98E-08	1.86E-05	1.72E-06
NGC0612	1.19E-03	1.19E-04	5.63E-03	5.18E-04
NGC0708	2.48E-06	2.48E-07	6.61E-04	6.09E-05
NGC1194	4.77E-04	4.77E-05	5.63E-03	5.18E-04
NGC1387	2.17E-06	2.17E-07	-	-
NGC1574	-	-	-	-
NGC2110	1.15E-2	1.15E-3	1.91E-02	1.76E-03
NGC3169	4.60E-04	4.60E-05	1.51E-03	1.39E-04
NGC3351	5.88E-07	6.10E-08	1.00E-05	3.46E-06
NGC3368	2.01E-06	2.01E-07	3.72E-04	3.42E-05
NGC3607	1.49E-06	1.49E-07	1.59E-03	1.46E-04
NGC3862	5.43E-04	5.43E-05	8.32E-04	7.67E-05
NGC4061	-	-	-	-
NGC4261	1.39E-04	1.39E-05	2.09E-03	1.93E-04
NGC4429	1.34E-06	1.34E-07	2.57E-04	2.37E-05
NGC4435	2.98E-06	2.98E-07	5.50E-04	5.06E-05
NGC4438	1.24E-06	1.24E-07	2.57E-03	2.37E-04
NGC4501	1.26E-05	1.26E-06	1.07E-03	9.87E-05
NGC4697	3.68E-07	3.68E-08	-	-
NGC4826	1.16E-07	2.56E-08	5.63E-04	5.18E-05
NGC5064	-	-	-	-
NGC5765b	5.96E-05	5.96E-06	-	-
NGC5806	-	-	-	-
NGC5995	8.14E-02	8.14E-03	-	-
NGC6753	-	-	-	-
NGC6958	-	-	-	-
NGC7052	1.07E-05	1.07E-6	1.45E-03	1.33E-04
NGC7172	2.63E-02	2.63E-03	-	-
PGC043387	-	-	-	-

Notes: (1) Galaxy name. (2) X-ray-traced accretion rate. (3) X-ray-traced accretion rate uncertainty. (4) [OIII]-traced accretion rate. (5) [OIII]-traced accretion rate uncertainty.

2.3.2 ACCRETION RATES

To estimate the SMBH accretion rates in each source, I use the following relation (Alexander & Hickox, 2012):

$$\left(\frac{\dot{M}_{\rm BH}}{\rm M_{\odot}\,yr^{-1}}\right) = 0.15\left(\frac{0.1}{\eta}\right)\left(\frac{L_{\rm Bol}}{10^{45}\,\rm erg\ s^{-1}}\right) \tag{2.8}$$

where $L_{\rm Bol}$ is the AGN bolometric luminosity and η is the mass-energy conversion efficiency factor, typically assumed to be 0.1 (e.g. Marconi et al., 2004).

I follow two prescriptions to estimate the AGN bolometric luminosities. The 2–10 keV X-ray luminosity is generally considered a good proxy of the AGN bolometric luminosity in radiative-mode AGN (e.g. Ho, 2008), as X-ray emission in these sources is expected to come from the corona above the accretion disc. In this case, the bolometric luminosity can be calculated by inverting the bolometric correction relation of Marconi et al. (2004):

$$\log_{10}\left(\frac{L_{\rm Bol}}{L_{\rm 2-10keV}}\right) = 1.54 + 0.24\mathcal{L} + 0.012\mathcal{L}^2 - 0.0015\mathcal{L}^3, \tag{2.9}$$

where $\mathcal{L} \equiv \log_{10}\left(\frac{L_{\rm Bol}}{L_{\odot}}\right) - 12$.

In kinetic-mode AGN, the accretion disk is expected to be absent and the 2–10 keV emission may instead arise from inverse Compton up-scattering of non-thermal photons from the radio jet (e.g. Blundell et al., 2006). For this reason, I additionally used the [OIII]λ5007 luminosity as a proxy of $L_{\rm Bol}$, adopting the bolometric correction $L_{\rm bol}/L_{\rm [OIII]} \approx 3500$ (Heckman et al., 2004), to ensure both types of AGN are covered. [OIII]λ5007 is a more ubiquitous tracer of nuclear activity as it is usually the brightest emission-line in optical spectra of AGN and is less contaminated than other emission lines. As illustrated in Table 2.1, a clear AGN classification is missing for some of my sample galaxies (13/35), whereas the majority of them consist on a mix of radiative- and kinetic-mode AGN. For each source, I thus calculate $L_{\rm b\mathit{ol}}$ using both the 2–10 keV and [OIII]λ5007 luminosity as tracers. I show the relation between these two derived bolometric luminosities in Figure 2.3. I note there is reasonably large scatter in the two measures of bolometric luminosity. This is likely due to the mix of radiative- and kinetic-mode objects in my sample, with the X-ray emission not being a good proxy for the bolometric luminosity of the latter (see above). The derived accretion rates are given in Table 2.5

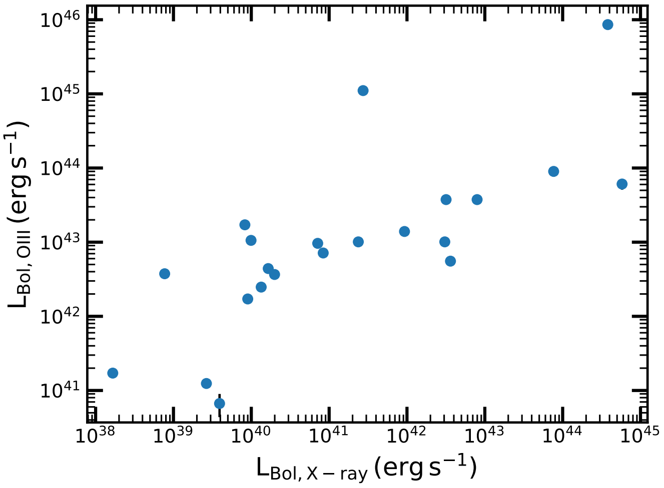

Figure 2.3: $L_{\rm Bol}$ derived from X-ray versus $L_{\rm Bol}$ derived from [OIII]

Table 2.6: Spearman rank coefficients and p-values

	Mass–Luminosity Correlations					
	log $(M_{\rm H_2,100pc}/{\rm M}_\odot)$ (1)		log $(M_{\rm H_2,75pc}/{\rm M}_\odot)$ (2)		log $(M_{\rm H_2,50pc}/{\rm M}_\odot)$ (3)	
	Coefficient	p-value	Coefficient	p-value	Coefficient	p-value
log($E_{1.4}$)	0.32	0.12	0.35	0.11	0.56	0.01
log($L_{\rm X,2-10}$)	0.31	0.16	0.29	0.21	0.29	0.26
log($L_{\rm mm}$)	0.002	0.99	0.14	0.55	0.11	0.66
log($\dot{M}_{\rm acc,X\text{-}ray}$)	0.31	0.16	0.29	0.21	0.29	0.26
log($\dot{M}_{\rm acc,[OIII]}$)	0.27	0.26	0.38	0.13	0.53	0.05
	Luminosity–Luminosity Correlations					
		Coefficient			p-value	
			(4)			
$L_{\rm mm} - L_{\rm X,2-10}$		0.76			3.37E-6	
$L_{\rm mm} - E_{1.4}$		0.57			0.008	
$E_{1.4} - L_{\rm X,2-10}$		0.16			0.56	
$L_{\rm [OIII]} - L_{\rm X,2-10}$		0.78			2.27E-5	
$L_{\rm [OIII]} - E_{1.4}$		0.15			0.60	
$L_{\rm [OIII]} - L_{\rm mm}$		0.52			0.01	

Notes: (1) Spearman rank correlation coefficients and p-value for the 100 pc radius aperture, (2) and (3) same quantities for the 75 and 50 pc radius apertures. (4) lists the Spearman rank correlation coefficients and p-values between the luminosities studied.

	Median values for samples			
	This Work	Garcia-Burillo+21	Izumi+16	Babyk+19
log $\mathrm{L_{bol}(erg\ s^{-1})}$	43.2	43.0	43.3	-
log $\mathrm{M_{BH}(M_\odot)}$	8.04	7.09	7.38	-
log $(\lambda_{\rm edd})$	-2.57	-2.20	-2.17	-
log $\mathrm{P_{jet}(erg\ s^{-1})}$	42.3	-	-	42.3

KS test	
Samples	*p*-values
This Work-GB+21 $(\mathrm{L_{bol}})$	0.015
This Work-Izumi+16 $(\mathrm{L_{bol}})$	0.001
This Work-GB+21 $(\mathrm{M_{BH}})$	0.0003
This Work-Izumi+16 $(\mathrm{M_{BH}})$	7.27×10^{-5}
This Work-GB+21 $(\lambda_{\rm edd})$	0.03
This Work-Izumi+16 $(\lambda_{\rm edd})$	0.003
This Work-Babyk+19 $(\mathrm{P_{jet}})$	0.53

Table 2.7: Median and KS test *p*-values for the samples used in this work

2.4 RESULTS AND ANALYSIS

2.4.1 PROPERTIES OF WISDOM AGN

As discussed above, in this work I aim to investigate previous claims that at circumnuclear scales (<100 pc) accretion rate tracers correlate with the mass and structure of the cold molecular gas mass. As illustrated in Table 2.1, my sample consists on systems with a diverse range of nuclear activities. In order to further place the WISDOM galaxies in context with previous studies, in Figure 2.4 I illustrate the main properties of the AGN in my sample (i.e. bolometric luminosity, black hole mass, Eddington ratio , central velocity dispersion and jet power), compared with those from the works of Izumi et al. (2016b), Babyk et al. (2019) and García-Burillo et al. (2021), with the medians for the samples used and the KS test *p*-values between the sample are shown in Table 2.7. In this work I calculated the jet power using the same method as Babyk et al. (2019). I calculated the radio power using the relation:

$$P_{\nu_0} = 4\pi D_{\rm L}^2 (1+z)^{\alpha-1} S_{\nu_0}\nu_0. \tag{2.10}$$

This was then used to calculate the jet power using this relation from Cavagnolo et al. (2010):

$$\log P_{\rm cav} = 0.75 \log P_{1.4} + 1.91. \tag{2.11}$$

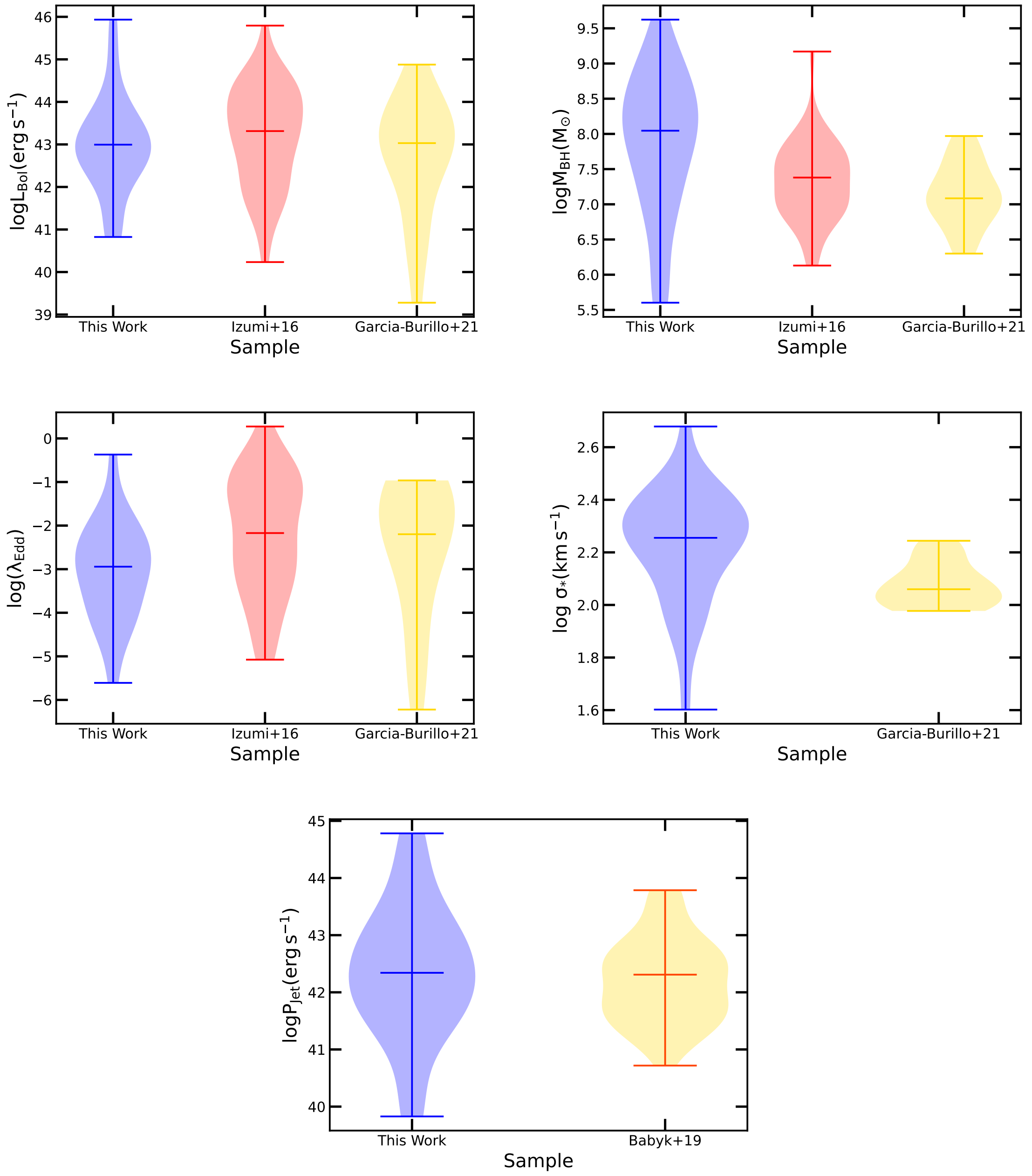

Figure 2.4: Distribution of AGN bolometric luminosity (top left), black hole mass M_{BH} (top right), Eddington ratio $\lambda_{\rm Edd}$ (middle left), velocity dispersion (middle right), and jet power (bottom) of the WISDOM sample. These are compared with the properties of the AGN from the works of Izumi et al. (2016b), Babyk et al. (2019) and García-Burillo et al. (2021) which are discussed further in the text. The horizontal lines represent the median of each distribution.

It is clear from Figure 2.4 that the bolometric luminosities of my AGN are consistent with those of the samples studied by Izumi et al. (2016b) and García-Burillo et al. (2021), and I probe a range of radio jet powers similar to that of the sources analysed by Babyk et al. (2019). On the other hand, the SMBH masses of the AGN in my sample are larger - on average - than those probed in such previous studies, and thus their Eddington ratios are slightly lower (at least when compared with the work of Izumi et al. 2016b).

More generally, Figure 2.4 shows that there is overlap between the main properties of the AGN in my sample and those in the previous reference studies, with the WISDOM objects being also clearly complementary to such works. In the following, I will further discuss potential differences and if/how these may affect my results.

2.4.2 AGN LUMINOSITY – MOLECULAR GAS MASS CORRELATIONS

In Figures 2.5-2.7 I show the obtained circumnuclear $\mathrm{H_2}$ masses plotted against excess 1.4 GHz continuum, 2-10 keV X-ray and nuclear mm-continuum luminosity, respectively. To check for the statistical significance of such relations, I carried out a Spearman rank analysis, where I consider relations with *p*-values$\lesssim 0.05$ as statistically significant. The resulting Spearman rank coefficients and *p*-values are presented in Table 2.6

Excess radio luminosity– molecular mass correlation

I show in Figure 2.5 the correlation between molecular gas mass on sub-kpc scales and excess radio emission. There is no strong correlation between these quantities, as indicated by Spearman rank analysis (reported in the first row of Table 2.6). The correlation coefficient is 0.32 for the 100 pc radius aperture, and increases to 0.35 for the 75 pc and 0.56 for the 50 pc radius aperture, with *p*-values of 0.12, 0.11 and 0.01, respectively. I note that, based on these results, a mild correlation may be present at the 50 pc scale. However, I checked that this is driven by galaxies that are dominated by star formation. When these objects are excluded, the Spearman rank coefficient becomes -0.07, with a *p*-value of 0.82, thus finding no evidence for any correlation.

X-ray luminosity-molecular gas mass correlation

I show in Figure 2.6 the relation between the molecular gas mass on sub-kiloparsec scales and 2-10 keV X-ray luminosity. Also in this case, there is no significant correlation between the two quantities within any aperture size, as supported by the Spearman rank analysis

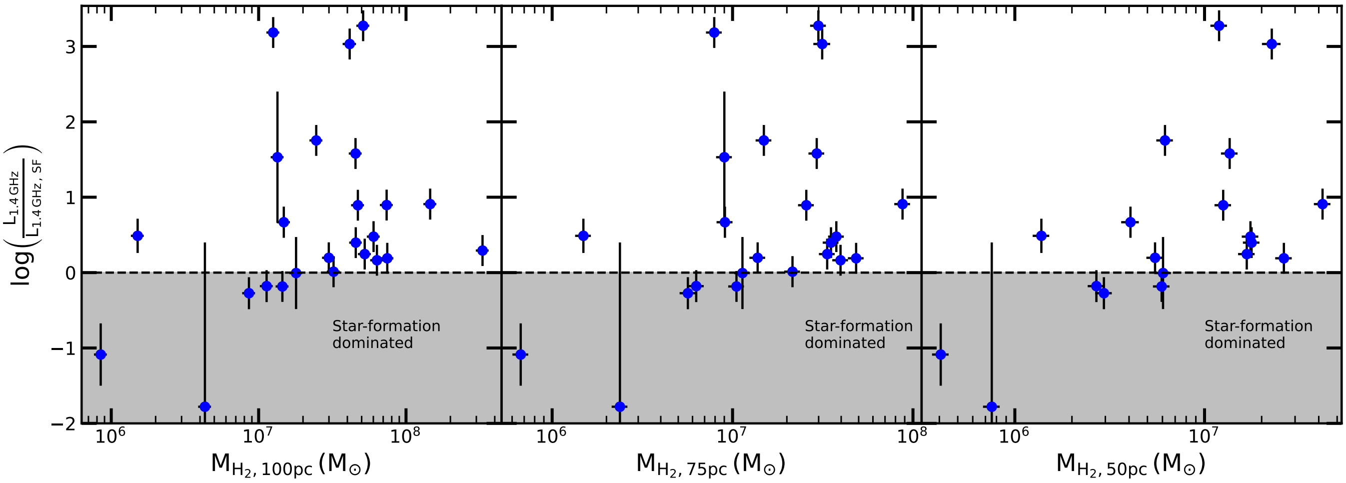

Figure 2.5: Molecular gas mass within an aperture of a given radius (100, 75 and 50 pc, as indicated by the x-axis labels) versus excess 1.4 GHz radio continuum fraction (after the contribution from star formation has been removed).

(reported in the second row of Table 2.6). The correlation coefficients are 0.31 with a *p*-value of 0.16 for the case of the molecular gas mass calculated within a 100 pc radius aperture, 0.29 with a *p*-value of 0.21 for the 75 pc radius aperture, and 0.29 with a *p*-value of 0.26 for the 50 pc radius aperture.

mm continuum luminosity– molecular gas mass correlation

The nuclear millimetre continuum luminosity is another proxy of the nuclear activity. Indeed, excess mm luminosity has been observed in AGN hosting galaxies, with the excess being attributed to the AGN itself (e.g. Behar et al., 2015, 2018; Doi & Inoue, 2016; Wu et al., 2018; Kawamuro et al., 2022). I show in Figure 2.7 the total nuclear millimetre luminosity (calculated on scales $\lesssim 200$ pc) against the molecular gas mass on sub-kiloparsec scales, again finding no correlation between the two. The lack of correlation is supported by the Spearman rank analysis (reported in the third row of Table 2.6). The correlation coefficients are 0.002, 0.14 and 0.11 with *p*-values 0.99, 0.55 and 0.66 for the 100 pc, 75 pc and 50 pc regions, respectively.

2.4.3 ACCRETION RATE–MASS CORRELATION

In Figures 2.8 and 2.9 I investigate relations between the molecular gas mass and AGN accretion rate, as calculated using the 2-10 keV and [OIII] line luminosity proxies. Also in

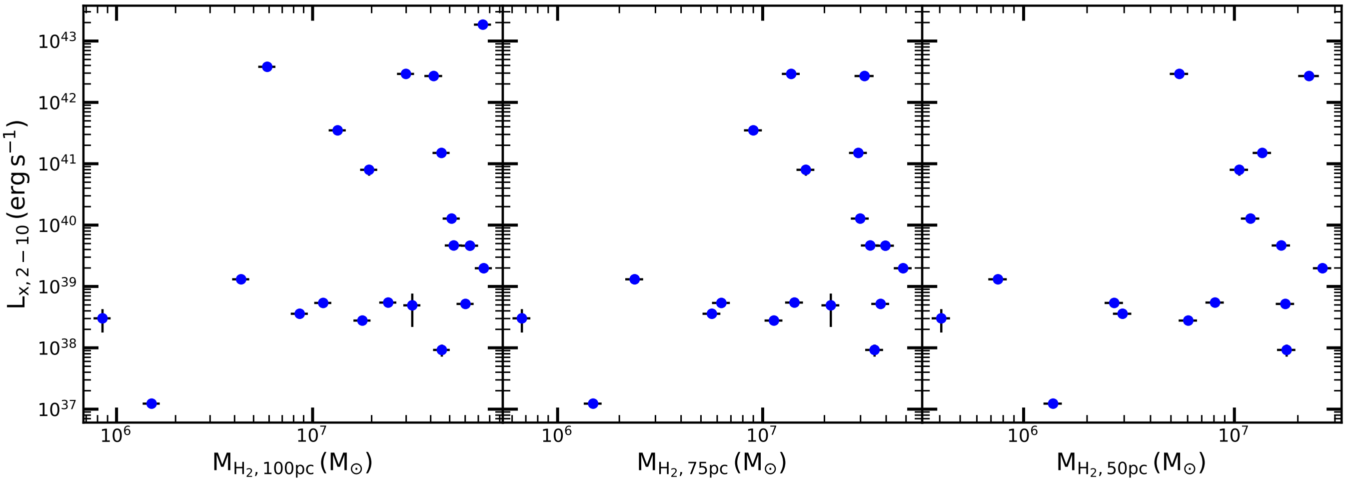

Figure 2.6: As Figure 2.5, but for the 2–10 keV X-ray luminosity.

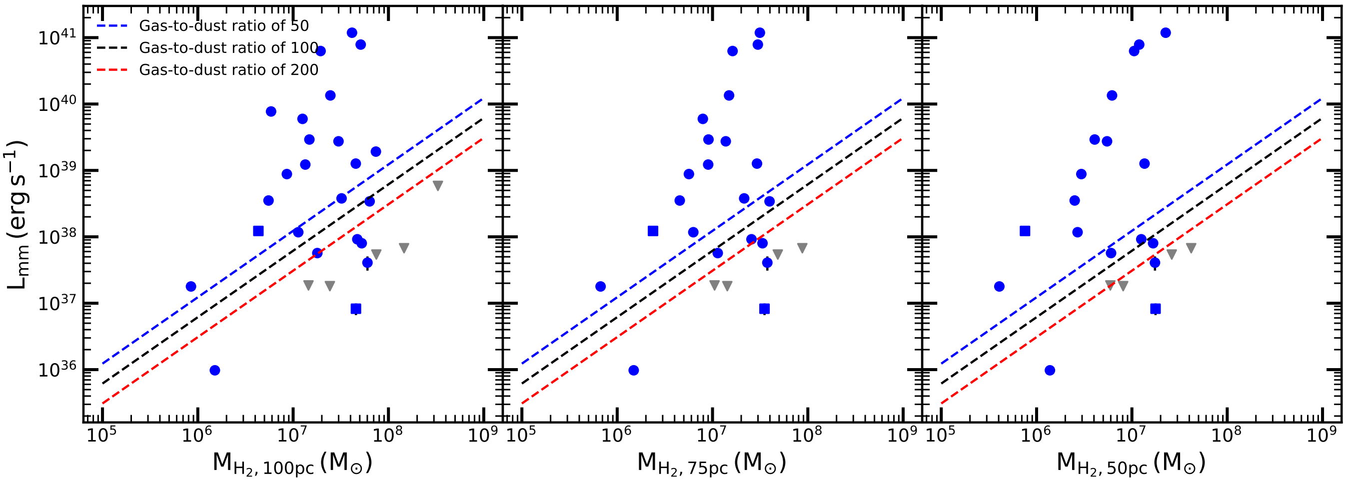

Figure 2.7: As Figure 2.5, but for the nuclear mm-continuum luminosity. Grey triangles are used for the upper limits (calculated as three times the rms noise level) of galaxies undetected in the mm continuum.

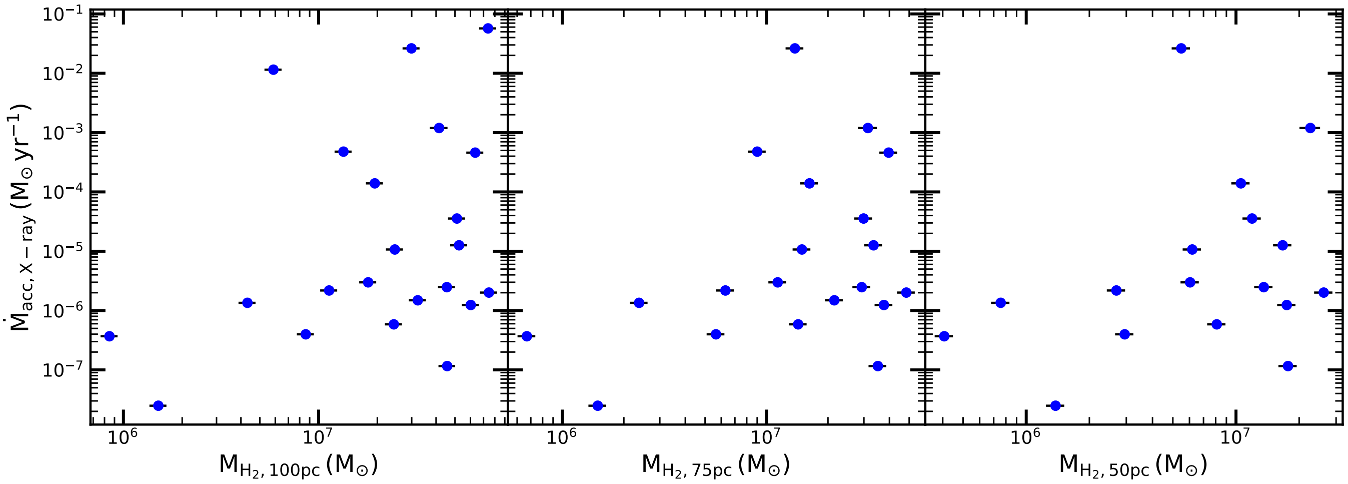

Figure 2.8: As Figure 2.5, but for the X-ray-traced accretion rate.

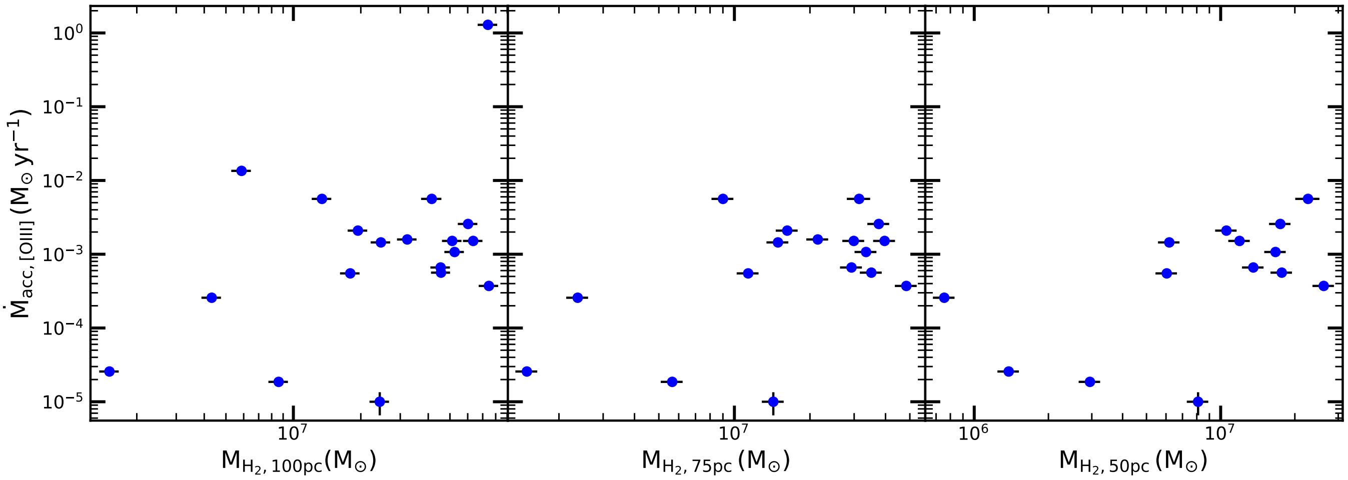

Figure 2.9: As Figure 2.5, but for the [OIII]-traced accretion rate.

this case, I do not find any clear correlation. The corresponding Spearman rank analysis (reported in the fourth and fifth rows of Table 2.6) mostly confirms this scenario.

For accretion rates calculated using the 2-10 keV luminosity as a proxy, a Spearman rank correlation coefficient of 0.31 with a *p*-value of 0.16 is obtained for the 100 pc radius aperture. For the 75 and 50 pc regions, the Spearman rank coefficients are 0.29 and 0.29, respectively, with associated *p*-values of 0.21 and 0.26.

For accretion rates calculated using the [OIII] line luminosity as a proxy, the Spearman rank coefficients are 0.27, 0.38 and 0.53 with p-values of 0.26, 0.13 and 0.05 for the 100 pc, 75 pc and 50 pc regions, respectively. These values imply that - as the aperture size decreases - a mildly significant correlation seems to be present. Whether this is real or coincidental due to the reduced number of data points should be investigated further.

2.5 DISCUSSION

2.5.1 AGN ACTIVITY AND THE CIRCUMNUCLEAR MOLECULAR GAS

As described above, I do not find any strong correlation between the masses of molecular gas in the nuclear regions of my diverse sample galaxies and their AGN activities, as traced in a variety of ways. This is despite multiple authors reporting such correlations when studying specific AGN-selected samples of galaxies (e.g Izumi et al., 2016b; Babyk et al., 2019; Koss et al., 2021). My galaxies were not selected to be AGN, but do cover similar ranges of AGN properties (see Figure 2.4).

My results suggests that the level of nuclear activity in a given galaxy cannot purely depend on the amount of cold gas around its SMBH. This supports recent work by Molina et al. (2023), where no correlation between the CO(2-1) and AGN luminosity has been reported. In this work, Molina et al. (2023) looked at the correlations between the cold molecular gas mass and AGN properties in a sample of radiative-mode AGN at z$\lesssim$0.5, using the 5100Å AGN luminosity as analogy for the AGN bolometric luminosity. In this way, they initially find a weak correlation between CO(2-1) and AGN luminosity, but this then disappears when correcting for the cosmic evolution of the molecular gas content in galaxies. This also clearly highlights that the mechanism(s) driving gas from the wider galaxy scales to the nuclear regions are likely to be different in different types of AGN, and that timescale variations may be important. Below I discuss each of my tracers, and the conclusions that can be drawn from the differences between my results and others in literature.

X-ray emission

As described in Sections 2.4.2 and 2.4.3 (and illustrated in Figures 2.6 and 2.8, respectively), there is no correlation between the cold molecular gas masses in the circumnuclear regions and the X-ray luminosities/X-ray derived accretion rates of my sample galaxies. These results are consistent with those found in other recent works. Rosario et al. (2018) looked at the relationship between the 2–10 keV X-ray luminosity and the CO(2-1) brightness in a sample of Seyfert galaxies with X-ray luminosities that fall within the range of those studied in my work (≈ $10^{41.5}$ to ≈ $10^{43.5}\mathrm{erg\,s^{-1}}$). The authors find no correlation between the two quantities, and ascribe that to the differences between the spatial scale probed by the single dish beam and and that of the SMBH accretion disc. García-Burillo et al. (2021) also studied the correlation between the molecular gas mass on kpc scales (0.4-1.2 kpc) and the X-ray luminosity in a sample of nearby Seyferts with similar $L_{X,2-10}$) ($\approx 10^{39}$ to $\approx 10^{44}\mathrm{erg\,s^{-1}}$) and molecular gas masses ($\approx 10^{6.5}$ to $\approx 10^{9.5}\mathrm{M_{\odot}}$) to the objects studied in this work, finding again no correlation between the two quantities. In this case, the lack of correlation is explained by the different spatial scales and timescales involved with the last steps of the SMBH fuelling process and the kpc-scales molecular gas reservoirs.

These results are in contrast to Izumi et al. (2016b), who reported a positive correlation between the dense ($n_{\mathrm{H_2}} \gtrsim 10^{4-5}\mathrm{cm^{-3}}$) molecular gas mass at ≈ 100 pc scales and the X-ray traced accretion rates (calculated using the same methods adopted here) onto the SMBHs of a small sample of 10 nearby Seyfert galaxies. This was interpreted as supporting the role of CNDs in the AGN fuelling process.

Differences between their results and mine may arise for several reasons. Firstly, as also discussed in Rosario et al. (2018) and García-Burillo et al. (2021) it is believed that in radiative-mode AGN X-ray emission traces recently accreted material, as in these cases X-rays are expected to be produced very close to the central SMBH (e.g. Galeev et al., 1979). In this scenario, X-ray emission can be highly time-variable. However, it would take dynamical timescales of several hundred thousand years for the gas at the scales I am investigating to fall onto the SMBHs. This difference in timescales and spatial scales could explain why I do not find correlation between the circumnuclear gas mass and the X-ray luminosity.

Izumi et al. (2016b) also investigated the correlation between dense molecular gas mass of the CND and accretion rate only in ten Seyfert galaxies, whereas I consider a > 3 times larger sample of galaxies with a varied range of nuclear activities (see Figure 2.4) and AGN types (see Table 2.1). However, even when considering only the Seyferts in my sample, my results remain unchanged.

Furthermore, the correlation reported by Izumi et al. (2016b) involves the dense ($n_{\mathrm{H_2}} \gtrsim 10^{4-5}\mathrm{cm^{-3}}$) molecular gas mass of the CNDs, estimated using the HCN molecule as tracer. Here I instead use the *total* molecular gas mass on circumnuclear scales, which has been estimated via CO emission. However, I still cannot make the Seyfert galaxies in my sample follow the correlation of Izumi et al. (2016b) without requiring extremely low dense-gas fractions that also vary wildly between galaxies, a behaviour currently not observed in these kind of objects (e.g. Jiménez-Donaire et al., 2019).

I also note that the lack of correlation may be also ascribed to contamination from other (unresolved) sources of X-ray luminosity in the galaxies, such as stellar X-ray binaries (see Section 2.2.3). However, even when restricting my analysis only to sources observed at high spatial resolution with *Chandra* (i.e. where the nuclear emission from the AGN can be spatially isolated), I still do not observe any correlation. This suggests that contamination is not driving my results.

Another more speculative possibility that could explain the lack of correlation is that different mechanisms usually give rise to the observed X-ray emission in different AGN types. In radiative-mode AGN such as Seyferts, X-rays are typically produced by inverse Compton up-scattering of photons from the accretion disk by the corona (Ciotti & Ostriker, 1997). Whilst, in kinetic-mode AGN, classic accretion discs are either not present or truncated at inner radii (see Section 2.1), and X-ray emission likely arises from other processes, such as Compton up-scattering of non-thermal photons from the radio jets (e.g. Blundell et al., 2006). These two emission processes may not correlate directly or may differ in how they correlate with the cold molecular gas mass of the circumnuclear regions.

Finally another more speculative possibility is that the Seyfert galaxies observed by Izumi et al. (2016b) may have been caught in a special phase with bright HCN emission, possibly suggesting a bias in the sample selection. Such bright HCN emission may be more common in Seyferts with sizeable dense molecular gas reservoirs, leading also to higher accretion rates than most of those probed by my sample. Further investigation of diverse galaxy samples in central regions < 50 pc in radius and using denser gas tracers will allow me to confirm/discard this hypothesis.

Radio emission

Babyk et al. (2019) reported a correlation between the molecular gas mass up to kpc scales and jet power in a sample of nearby ETGs, most of which are LERGs. I wanted to expand this study probing the gas mass down to circumnuclear scales and in a more diverse sample of galaxies.

If the results reported by Babyk et al. (2019) held at circumnuclear scales, I would have expected to observe at least some correlation between the circumnuclear gas masses of my sample galaxies and the excess 1.4 GHz radio luminosities (as $P_{\rm jet} \propto L_{1.4}$; e.g. Cavagnolo et al. 2010). As discussed in Section 2.4.2 and illustrated in Figure 2.5, I do not find any sign of such correlation in this work. This could be explained if the correlation reported by Babyk et al. (2019) does not have anything to do with the SMBH fuelling, but instead arise because more massive galaxies tend to have more massive SMBHs, thus producing higher-power radio jets (Liu et al., 2006). Babyk et al. (2019) also report a link between the hot X-ray-emitting diffuse gas and the molecular gas content in their sample galaxies. This correlation is explained by the cooling of hot gas which is turned into molecular gas in the galaxy. This cooling of hot gas may then be connected to the radio power in these galaxies and would explain why I do not find a correlation at circumnuclear scales. I note that a result similar to that of Babyk et al. (2019) has been recently reported by Fujita et al. (2023) and Fujita et al. (2024), who studied the correlation between the jet power estimated from X-ray cavities ($P_{\rm cav}$) and the molecular gas mass within 500 pc in a sample of massive elliptical galaxies. This difference in results could be explained by the sample studied by these two works. In these works they study 9 and 13 objects respectively which is significantly smaller then the 35 objects used in my work. They also look for correlations exclusively in elliptical galaxies compared to diverse range of galaxies and activities types study in my work.

Overall, the lack of correlation between the circumnuclear molecular gas mass and radio emission in my sample may suggest that jets are not directly powered by accretion from circumnuclear gas reservoirs, or that such correlation only exists over very long timescales. As discussed above, the dynamical times at the spatial scales probed here are still long compared to most AGN lifetime estimates. While radio jets can extend on large scales (and thus allow me to average AGN activity over longer timescales than direct tracers such as X-ray emission), this timescale mismatch may be too large to lead to any strong correlation.

Optical line emission

As described in Section 2.2.3, I estimated the accretion rate in my sources using also the [OIII] line emission as a tracer, finding again no correlation with the molecular gas mass in the circumnuclear regions (see Section 2.4.3 and Figure 2.9). One could ascribe this lack of correlation to contamination from other sources of [OIII] emission on larger scales (e.g. [OIII] can also be a tracer of star-forming regions). This kind of contamination, however, has been found to be relevant only in higher redshift galaxies (e.g. Suzuki et al., 2016), and should therefore be minimal in nearby galaxies like my sample sources.

This result provides support to the hypotheses formulated above that either the level of nuclear activity in a given galaxy does not exclusively depend on the amount of cold gas around the central SMBH, or temporal variations in the accretion rate wash out any correlation. These results also support the idea that AGN fuelling mechanisms are not ubiquitous and different processes may be at play in different AGN types.

2.5.2 NUCLEAR ACTIVITY AND STRUCTURE OF THE MOLECULAR GAS RESERVOIR

For a sample of nearby Seyfert galaxies, García-Burillo et al. (2021) reported that AGN luminosity (traced by 2-10 keV X-ray emission) correlates strongly with the structure of the molecular ISM (traced by CO) in the central 200 pc. This could be due to AGN feedback impacting the cold molecular gas reservoirs at these scales, and driving the molecular gas away from (and/or heating/destroying it in) the centres of the galaxies.

As discussed in - e.g. - Davis et al. (2018), some of the WISDOM sample galaxies have central molecular gas holes, and so it is possible the same mechanism is occurring here. I test this in Figure 2.10, where I plot the 2–10 keV X-ray luminosity against molecular gas concentration (as defined in Section 2.2) for both my sample and that of García-Burillo et al. (2021). My galaxies span a range of X-ray luminosities and molecular gas concentrations similar to those of García-Burillo et al. (2021), but do not seem to follow the same correlation.

The lack of any correlation in my galaxy sample, which spans a wide range of AGN types and $L_{\rm bol}$ ($10^{41}\ - 10^{46}\,{\rm erg\,s^{-1}}$) and does include a significant number of Seyferts (albeit not selected to be especially active), suggests two possibilities:

1. The central structure of the molecular gas in galaxies is set by secular (non AGN-driven) process(es). The correlation of García-Burillo et al. (2021) could then arise if these processes correlate with the SMBH mass (or another variable SMBH mass correlates with, such as spheroid mass/velocity dispersion), and thus the maximum AGN power possible. Some putative processes that could cause nuclear holes in the cold gas distributions (such as shear; see Davis et al. 2018) could naturally follow such a scaling.
2. The central structure of the molecular gas in my galaxies has been impacted by AGN feedback, but the black hole is now in a phase of lower activity. If this was the case, a galaxy would be expected to obey the García-Burillo et al. (2021) correlation until its AGN episode dies off, then decrease in X-ray luminosity while presenting its feedback-affected molecular gas structure for some time, before further inflows reset the cycle.

Comparing the WISDOM sample to the galaxies studied in García-Burillo et al. (2021), it seems that secular processes are the more likely scenario. My sample contains more early-type hosts, but other galaxy and AGN properties are similar. It is unclear why the SMBH and its energy output (set on sub-parsec scales) would care about the large-scale

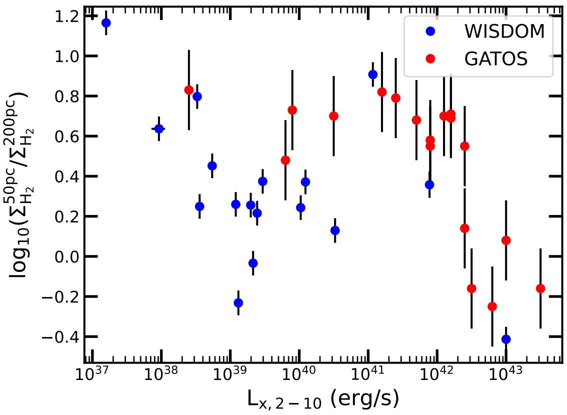

Figure 2.10: 2-10 keV X-ray luminosity versus nuclear molecular gas concentration. Blue data points are for the sample analysed in this work, red data points are from García-Burillo et al. (2021). The galaxies in my sample do not obey the trend reported in such previous work. This suggests that either the impact of AGN feedback is still detectable in a galaxy when it has gone into a lower activity phase, or the structure of the nuclear molecular gas is not determined by AGN processes.

galaxy properties, thus implying that the central molecular gas concentration is set by secular processes rather than by the nuclear activity. On the other hand, the parameter space explored in García-Burillo et al. (2021) could represent the turnover point between secular processes and AGN feedback, with the turnover happening at X-ray luminosities around 10^{42} erg s^{-1}. My points would then fit this model with the sample AGN with X-ray luminosities lower than 10^{42} erg s^{-1} and a range of molecular gas concentrations set by secular processes. The few galaxies in my sample with X-ray luminosities higher than 10^{42} erg s^{-1} instead follow the relation found in García-Burillo et al. (2021). Determining which of these possibilities is at work in my sample galaxies is interesting, but will require further observations and simulations of molecular gas at the centres of active galaxies of all luminosities. This will be explored further in future works.

2.6 CONCLUSIONS

I have searched for correlations between the cold molecular gas masses on the circumnuclear regions of a sample of 35 nearby galaxies and AGN activity tracers at radio, X-ray, optical and sub-mm wavelengths. I find that the molecular gas masses of my sample sources, measured within a range of elliptical apertures with radii from 50 to 100 pc, do not correlate with any of the adopted tracers.

The sample analysed in this study includes galaxies with a range of nuclear activities and global properties, and I am unable to reproduce any of the results found for other AGN-specific sub-samples. This suggests the level of nuclear activity in a given galaxy cannot purely be due the amount of cold gas fuel reservoir around the central SMBH. The fuelling mechanism of active galaxies is not ubiquitous and may vary between AGN types, and timescale variations are likely very important.

I also probed the molecular concentration of the circumnuclear gas discs in my sample galaxies to assess whether they had been impacted by AGN feedback. There is no evidence of a relation between structure on circumnuclear scales and current accretion rate, in contrast to results found for some nearby Seyfert galaxies selected to be in an active phase and despite my objects spanning the same range in circumnuclear properties. This could indicate that these galaxies were previously in a more active phase that impacted the circumnuclear gas, or that these molecular concentrations arise naturally within circumnuclear gas discs and are not related to AGN processes.

Further observations and theoretical studies are clearly needed to make further progress to determine the link between circumnuclear gas reservoirs and nuclear activity. For instance, dense gas may be better linked to the direct reservoirs for accretion, and expanded sample sizes may help to overcome timescale issues.

CHAPTER 3

A comparison between AGN diagnostic diagrams

“Oh I just did some Python."

-Andy Cook

3.1 INTRODUCTION

Baldwin et al. (1981) first proposed the use of the [NII]/Hα and the [OIII]/Hβ line ratios as a diagnostic tool to separate objects into whether their WIM is being ionized by star formation or by AGN. In this diagram AGN have higher ratios as they can produce higher-energy photons which can cause more heating the NLR of their host galaxies leading to an increase in the emission lines. This shows that AGN can efficiently excite the lower density gas in the WIM. An example of a BPT diagram is shown in Figure 3.1. However, what it is not yet clear whether AGN can also excite dense gas in the CMM in a similar way and if the emission lines from this excitation can be used to identify AGN effectively.

Thanks to latest-generation (sub-)millimetre interferometers such as the Atacama Large Millimeter/submillimeter Array (ALMA), the cold component of the ISM in galaxies has been now probed using a variety of different molecular gas tracers, including CO, HCN, HCO^+ and CS. CO is the workhorse for molecular gas studies in galaxies, as it is the most abundant molecule after H_2 and has excitation temperatures that make it easily excited even at low temperatures (i.e. $T_{\mathrm{ex}} = 5.53$ K for the ground $J = 1 \rightarrow 0$ transition; e.g. Bolatto et al., 2013). A number of studies have detected different CO transitions in the nuclear regions of AGN host galaxies (e.g. García-Burillo et al., 2014; Moser et al., 2016; Oosterloo et al., 2017; Ruffa et al., 2019a; Koss et al., 2021; Ruffa et al., 2022; Lelli

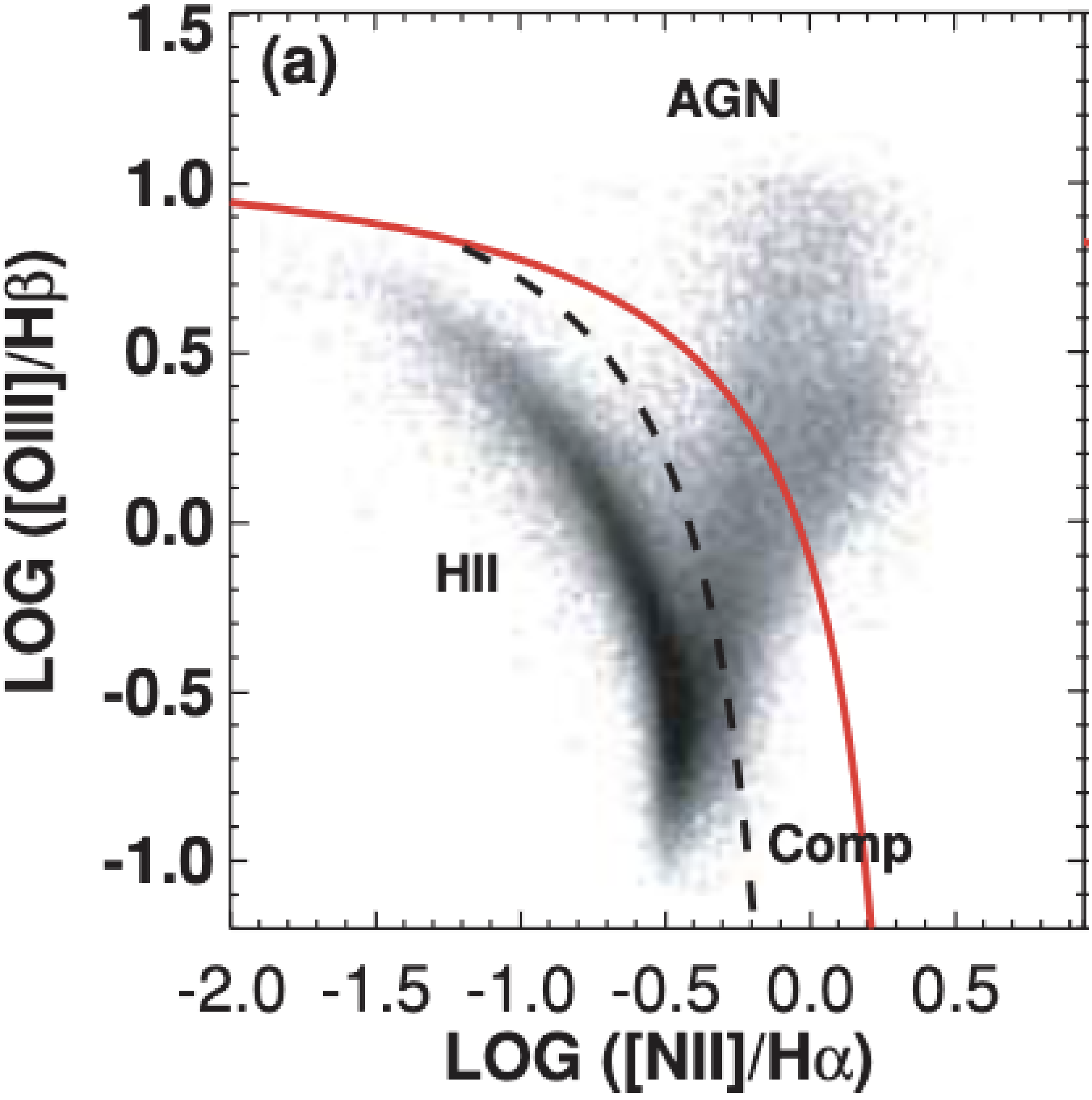

Figure 3.1: An example BPT diagram taking from Kewley et al. (2006). The dashed and solid lines represent the different star formation boundaries.

et al., 2022; Elford et al., 2024). HCN, HCO$^+$ and CS are instead the most used tracers of the dense molecular gas component, as their critical density (i.e. the density at which collisional excitation balances spontaneous radiative de-excitation) is $n_{\rm crit} > 10^4$ cm^{-3} (e.g. García-Burillo et al., 2014). Gao & Solomon (2004b,a) studied the HCN(1-0) line in a large sample of nearby normal star-forming (spiral) and starburst galaxies and found a tight correlation between their infrared (IR; tracing star formation) and HCN luminosities. This has been interpreted as implying that the dense molecular gas is directly associated with active star forming regions, rather than being simply a tracer for the total molecular gas. Similar correlations have been also later found by Tan et al. (2018), but using both the HCN(4-3) and the $\rm HCO^+$(4-3) transitions as dense molecular gas tracers.

Dense cold gas tracers have been detected also in AGN host galaxies (e.g. Baan et al., 2008; Krips et al., 2008; Juneau et al., 2009; García-Burillo et al., 2014; Moser et al., 2016; Ruffa et al., 2018; Imanishi et al., 2020; Li et al., 2021; Ruffa et al., 2022), and their ratios often used as a tool to probe the relative contribution of star formation and AGN to the excitation of the ISM. For instance, a high intensity of HCN(1-0) with respect to $\rm HCO^+$(1-0) and/or CO(1-0) has been proposed as a feature unique to AGN. This is because the X-ray dissociation regions (XDRs) around radiatively-efficient AGN penetrate deep into the surrounding medium and destroy HCO+ molecules more efficiently than the analogous photodissociation regions (PDRs) in starburst areas (e.g. Jackson et al., 1993; Sternberg et al., 1994; Tacconi et al., 1994; Kohno et al., 2001; Usero et al., 2004; Kohno, 2005; Imanishi et al., 2007; Krips et al., 2008; Davies et al., 2012; Ruffa et al., 2018). Furthermore, Izumi et al. (2013) found that the HCN(4-3)/$\rm HCO^+$(4-3) and HCN(4-3)/CS(7-6) integrated intensity ratios are higher in AGN than in starburst galaxies. They thus proposed a diagnostic diagram based on these line ratios, which has been dubbed the "*submm-HCN diagram*" (then expanded in Izumi et al., 2016a). However, more work needs to be done to test how results from the *submm-HCN diagram* compare to other methods of studying excitation/ionisation from AGN (e.g. by using the optical BPT diagrams; Baldwin et al. 1981) and fully understand the connection between nuclear activity and dense gas tracers.

The Close AGN Reference Survey (CARS; Husemann et al. 2017, 2019) is utilising facilities such as the multi-unit spectroscopic explorer (MUSE; Bacon et al., 2010, 2014) and ALMA to study 41 of the most luminous type 1 (i.e. unobscured) AGN at redshifts $0.01 < z < 0.06$. In this chapter, I present new ALMA observations of the CO, HCN, $\rm HCO^+$ and CS molecular gas transitions in 5 AGN of the CARS sample, which were selected to span the full range of AGN luminosity ($\log L_{\rm AGN} = 42.9 - 45.4\ {\rm erg}\, s^{-1}$) and stellar masses ($8.85 < {\rm M}_* < 11.2\, M_\odot$) of the sample. I study the position of these sources on the Gao and

Solomon relations between the IR and HCN luminosities. I also make use of the *submm-HCN diagram* to examine its prediction for the cold gas excitation mechanism in these 5 objects. I then compare their classification in the sub-mm to the one in the optical using the classic BPT diagnostic diagram, that I create from the MUSE data available for the CARS sample.

The chapter is organised as follows: in Section 3.2, I describe the sample and the observations used for my analysis. I describe the methodology and results in Section 3.3. I discuss my results in Section 3.4, before summarising and concluding in Section 3.5.

3.2 OBSERVATIONS

In this study I use both interferometric data from ALMA and integral field unit (IFU) data from MUSE, all obtained as part of CARS. Full details about this survey can be found in Husemann et al. (2017). In short, the CARS targets are drawn from the Hamburg-ESO Survey (HES, Wisotzki et al. 2000), which is a purely flux-limited ($B_J \lesssim 17.3$) catalog of 415 luminous type 1 (unobscured) AGN based on *B*-band optical photometry and slitless spectroscopy. Applying a redshift cut of $z \leq 0.06$, the HES catalog leads to a sample of 99 AGN. From these, a representative sub-sample of 41 objects was randomly selected and observed first in CO(1-0) with the IRAM-30m telescope (Bertram et al., 2007), and then with MUSE (Husemann et al., 2017).

3.2.1 ALMA

The 5 CARS targets of this study are HE0108-4743, HE0433-1028, HE1029-1831, HE1108-2813 and HE1353-1917 (see Table 3.1 for a summary of their main properties). ALMA band 7 observations of the dense molecular gas component in these objects were taken in 2018, targeting the HCN(4-3), $\mathrm{HCO^+}$(4-3) and CS(7-6) lines (Project Code: 2017.1.00258.S).

The spectral configuration of the ALMA observations consisted of 4 spectral windows (SPWs), three centred on the redshifted frequencies of the three targeted lines (354.505 GHz, 356.734 GHz and 342.883 GHz for HCN(4-3), HCO+(4-3) and CS(7-6), respectively) and one used to map the continuum. For three of the five targets (i.e. HE0433-1028, HE1108-2813 and HE1353-1917), previous ALMA band 3 observations of the ^{12}CO(1-0) and ^{13}CO(1-0) lines are also available (Project Code: 2016.1.00952.S). The spectral configuration of the CO observations consisted of 4 SPWs: 2 centred on the redshifted frequency of the two targeted lines (115.271 GHz and 110.201 GHz for ^{12}CO(1-0) and ^{13}CO(1-0), respectively),

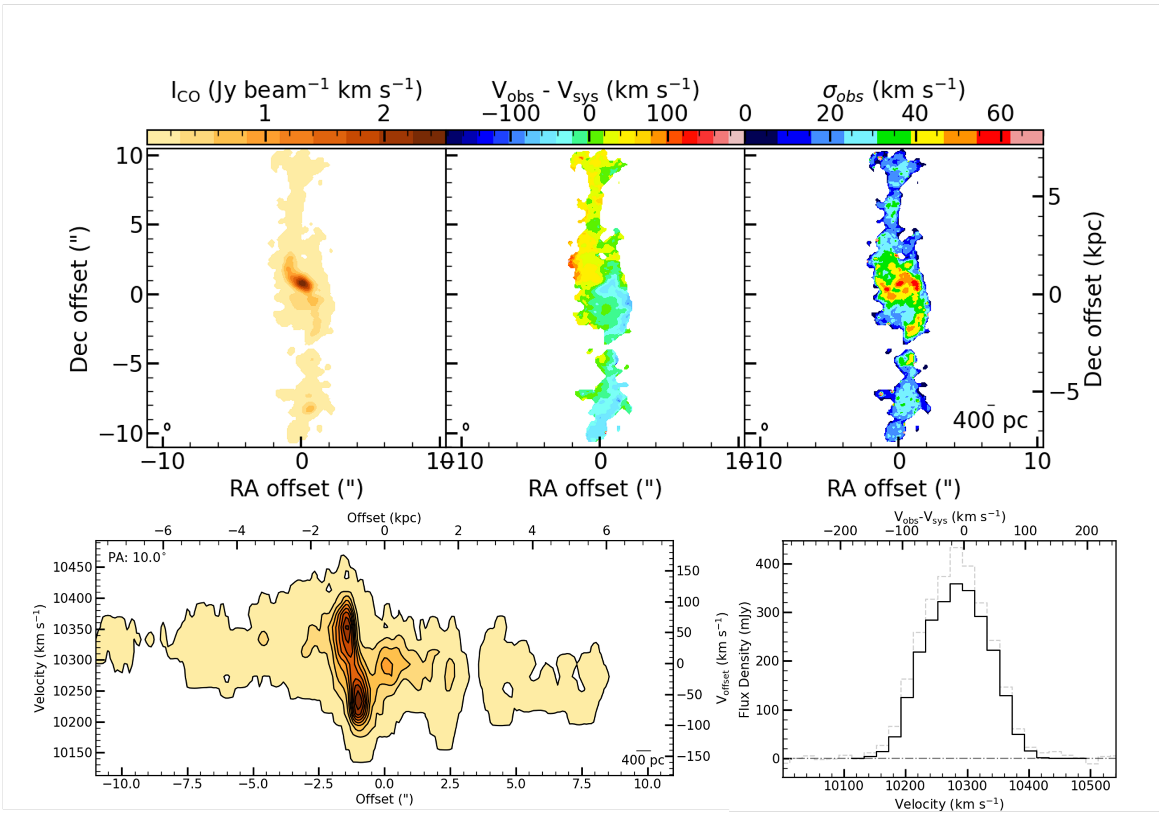

Figure 3.2: Data products of the ^{12}CO(1-0) ALMA observations of HE0433-1028. The moment 0 (integrated intensity), moment 1 (mean line-of-sight velocity) and moment 2 (mean line-of-sight velocity dispersion) maps are shown in the top-left, top-middle and top-right panels, respectively. The position-velocity diagram (PVD) is shown in the bottom-left and the integrated spectrum in the bottom-right panels. The synthesised beam is shown in the bottom-left corner of each moment map, and a scale bar in shown in the bottom-right corner of the moment 2 map and the PVD. The bar above each moment map illustrates the colour scale.

and the other two used to observe the continuum. For both sets of data a standard calibration strategy was adopted: a single bright quasar was used as both flux and bandpass calibrator, a second one as a phase calibrator. All data sets were calibrated using the the Common Astronomy Software Applications (CASA) pipeline, version 5.1.1 (McMullin et al., 2007). The obtained calibrated datasets were then combined (where needed) and imaged using the same CASA version.

3.2.2 LINE IMAGING

Continuum emission was measured over the full line-free bandwidth and subtracted from the data in the *uv*-plane using the CASA task `uvcontsub`. The line data was then imaged using the `CASA` task `tclean` with Briggs weighting and a robust parameter of 0.5, which allows to obtain the best trade-off between sensitivity and resolution. The resulting 3D (RA, Dec, velocity) data cubes were produced with channel widths of $20\,\mathrm{km\,s^{-1}}$ and a pixel size which approximately Nyquist samples the synthesized beam. The HCN(4-3) and HCO^{+}(4-3) lines were clearly detected in three out of five sources (i.e. HE0433-1028, HE1029-1831 and HE1108-2813). ^{12}CO(1-0) was also clearly detected in all the sources in which it was targeted (i.e. HE0433-1028, HE1108-2813 and HE1353-1917). CS(7-6) and ^{13}CO(1-0) were not detected in any of the targets. The achieved angular resolution and 1σ root mean square (rms) noise levels (measured in line-free channels) for each target and each molecular line are listed in Table 3.2

Continuum imaging

For each target, the continuum SPWs and the line-free channels of the line SPWs were used to produce the continuum maps using the CASA task `tclean` in multi-frequency synthesis (mfs) mode, and Briggs weighting with robust parameter of 0.5. This resulted in synthesised beam sizes in the range $0''.704 - 0''.863$ (corresponding to physical scales of $373 - 633$ pc) for the band 7 continuum maps, and $0.''447 - 0.''587$ ($284 - 426$ pc) for those in band 3. The corresponding 1σ rms noise levels are in the ranges $45.2 - 560$ $\mu\mathrm{Jy\ beam}^{-1}$ (band 7) and $11.4 - 20.8\ \mu\mathrm{Jy\ beam}^{-1}$ (band 3). A single unresolved, point-like continuum source is detected at all frequencies and for almost all the targets. The only exception is the band 7 continuum map of HE0433-1028, where two point-like sources are observed: one coincident with the galaxy nucleus and the second one lying $\sim\ 4''$ (~ 3 kpc) to the South of it. An overlay between the CO and band 7 continuum detections of this object allows me to verify that this second continuum source is also well within the CO disk (illustrated in Figure 3.2). However, due to the quite large separation of the two continuum detections and the second one not being detected in any other observation of this object, I conclude that this latter is likely a background galaxy. All the continuum fluxes and associated uncertainties are reported in Table 3.3.

3.2.3 MUSE

IFU data of the five targets was obtained with the MUSE instrument at the Very Large Telescope (VLT; Bacon et al., 2010, 2014) under programs 094.B-0345(A) (HE0108-4743, HE0433-1028, HE1029-1831 and HE1108-2812) and 095.B-0015(A) (HE1353-1917). Here I use the extracted fluxes of the $\mathrm{H}\alpha$, $[\mathrm{OIII}]\lambda5007$, $\mathrm{H}\beta$ and $[\mathrm{NII}]\lambda6583$ lines. Full details on

Table 3.1: Basic parameters of my galaxy sample.

Galaxy (1)	z (2)	$\log L_{\rm AGN}$ $({\rm erg\,s^{-1}})$ (3)	$\log M_{\star}$ $(M_{\odot})$ (4)	SFR $({\rm M_{\odot}\,yr^{-1}})$ (5)	PA ∘ (6)
HE0108-4743	0.024	43.6	9.77	$4.3^{+0.2}_{-0.2}$	90
HE0433-1028	0.036	44.8	10.80	$19.4^{+0.2}_{-0.2}$	10.0
HE1029-1831	0.041	44.3	10.49	$27.1^{+0.8}_{-1.3}$	90.0
HE1108-2813	0.024	44.0	10.29	$12.4^{+0.4}_{-0.4}$	7.0
HE1353-1917	0.035	44.1	10.99	$2.8^{+0.1}_{-0.1}$	29.1

Notes: (1) galaxy name and its redshift based on the stellar continuum in the observed . IFU data in (2). (3) AGN luminosity estimated from the Hβ luminosity with the stellar mass of the object inferred from SED modelling in (4). (5) star formation rate with associated errors taken from Smirnova-Pinchukova et al. (2022). (6) is the position angle of the object estimated from the CO moment 1 map for HE0433-1831 and HE1108-1813, taken from Husemann et al. (2019) for HE1353-1917 or taken from the NASA Extragalactic Database (NED)[2].

[2] `https://ned.ipac.caltech.edu/`

Table 3.2: Main properties of the presented ALMA observations.

Galaxy (1)	$\theta_{\rm HCN}$ (arcsec) (2)	$\theta_{\rm HCO+}$ (arcsec) (3)	$\theta_{\rm CS}$ (arcsec) (4)	$\theta_{\rm CO}$ (arcsec) (5)	$\theta_{\rm ^{13}CO}$ (arcsec) (6)	$\sigma_{\rm HCN}$ $({\rm mJy\ beam^{-1}})$ (7)	σ $_{\rm HCO+}$ $({\rm mJy\ beam^{-1}})$ (8)	$\sigma_{\rm CS}$ $({\rm mJy\ beam^{-1}})$ (9)	$\sigma_{\rm CO}$ $({\rm mJy\ beam^{-1}})$ (10)	$\sigma_{\rm ^{13}CO}$ $({\rm mJy\ beam^{-1}})$ (11)
HE0108-4743	0.731	0.727	0.759	-	-	0.624	0.686	0.646	-	-
HE0433-1028	0.899	0.900	0.936	0.406	0.417	1.26	1.29	1.43	0.492	0.455
HE1029-1831	0.735	0.735	0.763	-	-	0.673	1.38	1.00	-	-
HE1108-2813	0.789	0.789	0.818	0.520	0.528	0.831	0.883	0.837	0.895	0.744
HE1353-1917	0.694	0.692	0.719	0.533	0.557	0.466	0.499	0.547	0.374	0.351

Notes: (1) galaxy name. (2) - (6) the geometric mean of the major and minor axis of the beam for HCN, HCO^{+}, CS, CO and ^{13}CO observations and corresponding 1σ rms noise levels in (7)-(11).

the MUSE observations and data reduction can be found in Husemann et al. (2022). In this work, I make use of the reduced MUSE data products, which are also publicly-available in the CARS archive[*].

3.3 METHODS AND RESULTS

3.3.1 ALMA DATA PRODUCTS

Integrated intensity (moment 0), mean line-of-sight velocity (moment 1) and velocity dispersion (moment 2) maps of the HCN, HCO^{+}, CS and CO detections were produced from the continuum-subtracted data cubes using the masked moment technique (Dame,

---

[*] `https://cars.aip.de/`

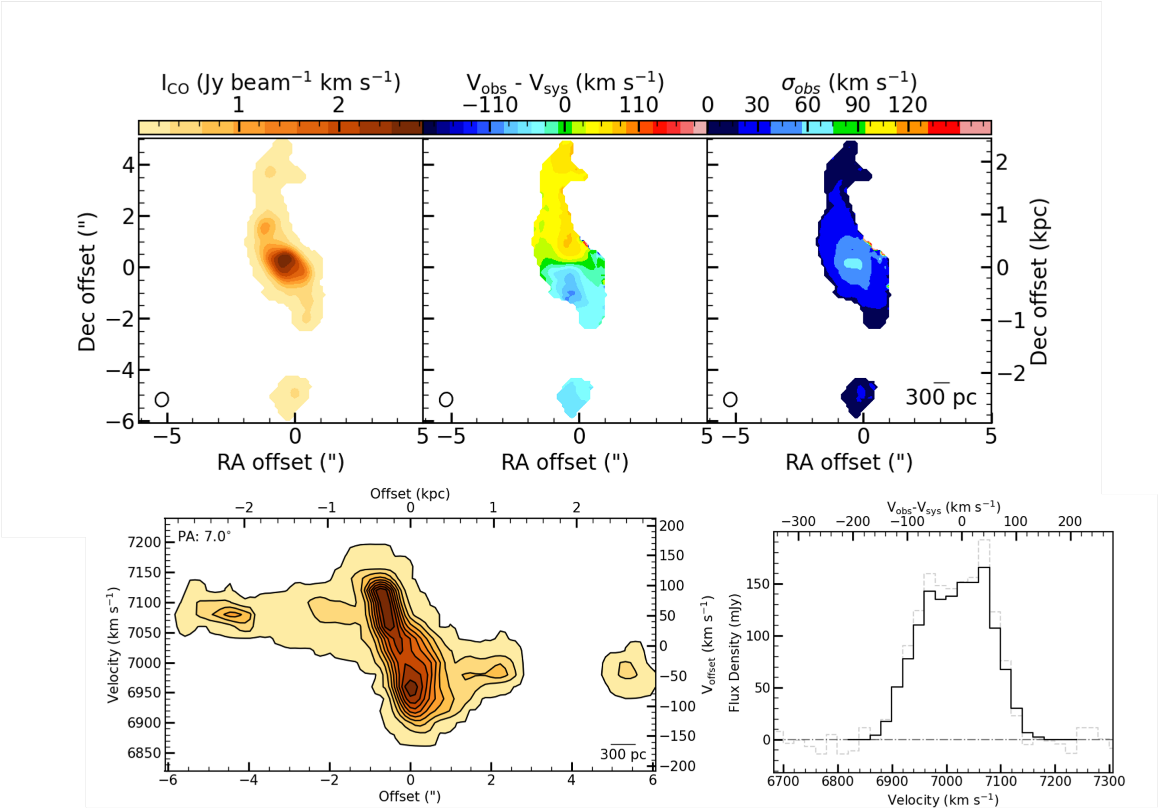

Figure 3.3: As in Figure 3.2, but for HE1108-2813. The spectrum is extracted within a box of $5.0'' \times 13.5''$.

Table 3.3: Main properties of the ALMA continuum detections.

Galaxy (1)	$S_{\rm cont,\ 339}$ (mJy) (2)	$\Delta S_{\rm cont,\ 339}$ (mJy) (3)	$S_{\rm cont,\ 104}$ (mJy) (4)	$\Delta S_{\rm cont,\ 104}$ (mJy) (5)
HE0108-4743	1.05	0.0534	-	-
HE0433-1028 (Main source)	2.25	0.122	0.727	0.0146
HE0433-1029 (Secondary source)	1.89	0.122	-	-
HE1029-1831	5.56	0.0700	-	-
HE1108-2813	5.46	0.560	0.117	0.0208
HE1353-1917	0.318	0.0452	0.185	0.0114

Notes: (1) galaxy name. (2) - (3) integrated flux densities of the band 7 continuum maps (reference frequency: 339 GHz) and corresponding uncertainties. (4) - (5) integrated flux densities of the band 3 continuum maps (reference frequency: 104 GHz) and corresponding uncertainties.

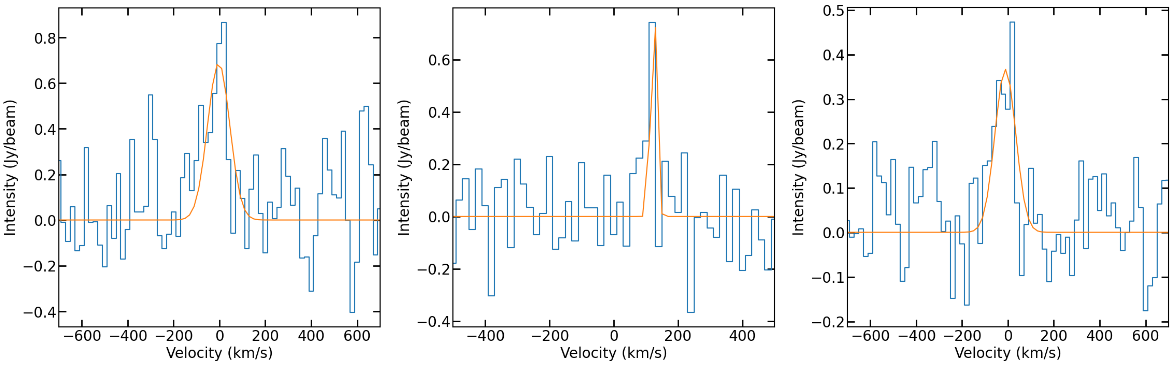

Figure 3.4: Stacked spectra of the HCN (4-3) line in HE0433-1028 (left), HE1029-1831 (middle) and HE1108-2813 (right). The orange lines shows the best-fitting Gaussian profiles.

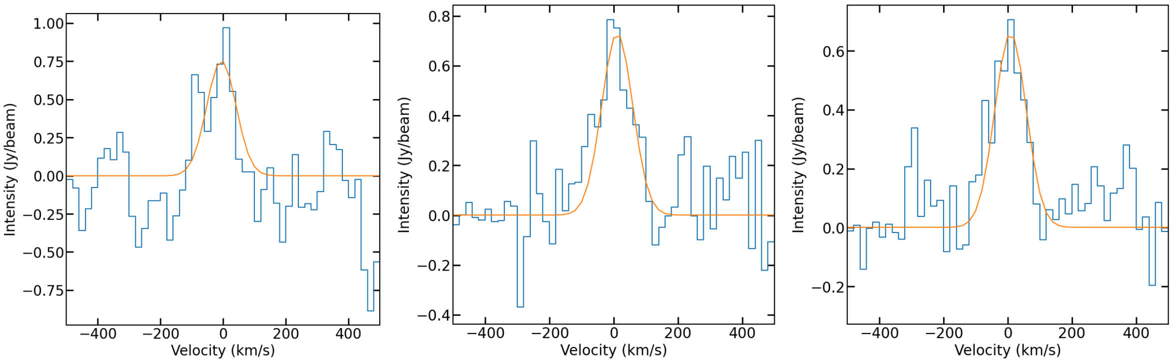

Figure 3.5: Stacked spectra of the HCO+ (4-3) line in HE0433-1028 (left), HE1029-1831 (middle) and HE1108-2813 (right). The orange lines shows the best-fitting Gaussian profiles.

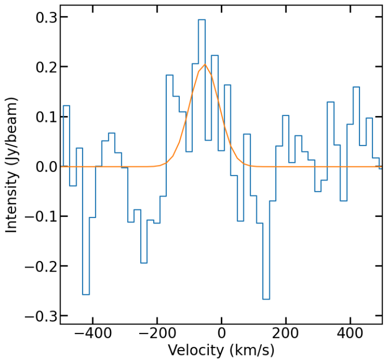

Figure 3.6: Stacked spectra of the CS (7-6) line in HE1108-2813. The orange line shows the best-fitting Gaussian profile.

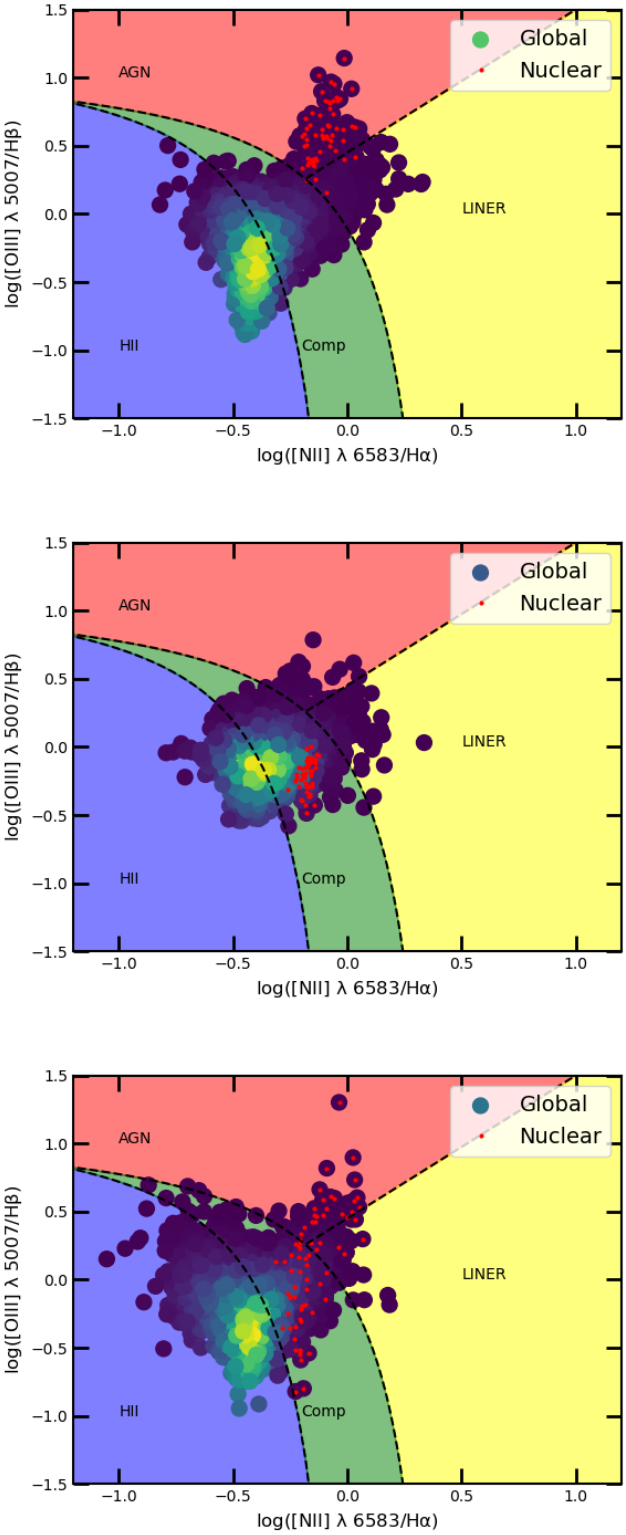

Figure 3.7: Global BPT diagrams of HE0433-1028 (top), HE1029-1831 (middle) and HE1108-2813 (bottom). The red points show the results obtained for the nuclear regions of each object, assumed to be within one ALMA beam size.

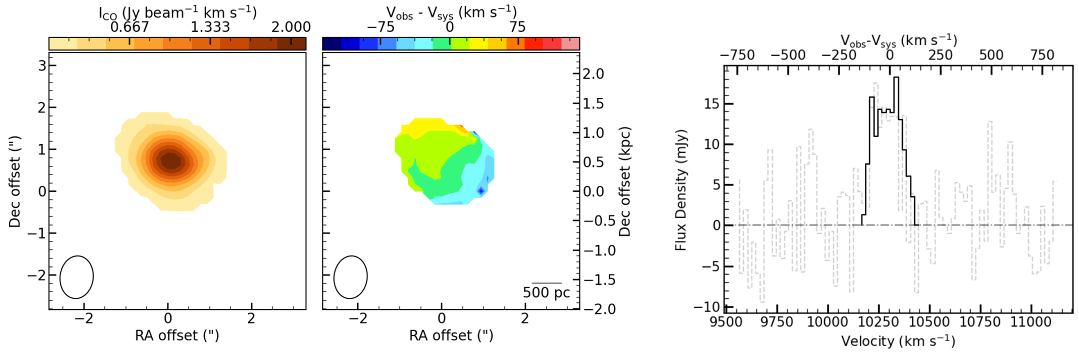

Figure 3.8: HCN moment 0 (left), moment 1 (middle) and integrated spectrum (right) obtained from the ALMA observations of HE0433-1028. The synthesised beam is shown in the bottom-left corners of each map and a scale bar is shown in the bottom-right corner of the moment 1 map. The bar above each map illustrates the colour scale. The spectrum has been extracted within a box of $3.0'' \times 2.5''$. Coordinates are with respect to the image phase centre; East is to the left and North to the top.

2011), as implemented in the Pymakeplots routine[†]. In this procedure, a copy of the cleaned data cube is first Gaussian-smoothed spatially with a FWHM equal to 1.5 times that of the synthesised beam, and then smoothed in the velocity dimension with a boxcar kernel FWHM of 4 channels. A three-dimensional mask is then created by selecting all the pixels above a fixed flux-density threshold (chosen by the user) in the smoothed data cube. The moment maps are then constructed using the original, un-smoothed cubes within the masked regions only. In the majority of the cases, I adopted a flux-density threshold for the mask of 5σ, to ensure that only real, high-significance gas emission is included. Major-axis position velocity diagrams (PVDs) of the line detections were then constructed by summing the pixels in the masked cube within a pseudo-slit whose long axis is oriented along the position angle of gas distribution. Integrated spectra were created from the observed data cubes by summing over both spatial dimensions within boxes enclosing all the detected line emission. The obtained data products are illustrated in Figures 3.2 and 3.3 for the CO(1-0) detections in HE0433-1028 and HE1108-2813, respectively (the data products for HE1353-1917 have already been presented in Husemann et al., 2019 and thus not reproduced here), and in Figures 3.8-3.13 for all the HCN(4-3) and HCO$^+$(4-3) detections.

The CO(1-0) emission in HE0433-1028 and HE1108-2813 is well resolved. In particular, the integrated intensity maps (top-left panels of Figures 3.2 and 3.3) shows that in both cases the CO gas is distributed along the bar of the galaxy and extends $\approx 22''(\sim 16.4\mathrm{kpc})$ and $\approx 13.5''(\sim 6.7\mathrm{kpc})$, respectively, along its major axis. The integrated flux densities of the two CO(1-0) detections are listed in Table 3.4. These were estimated by numerically

---

[†] `https://github.com/TimothyADavis/pymakeplots`

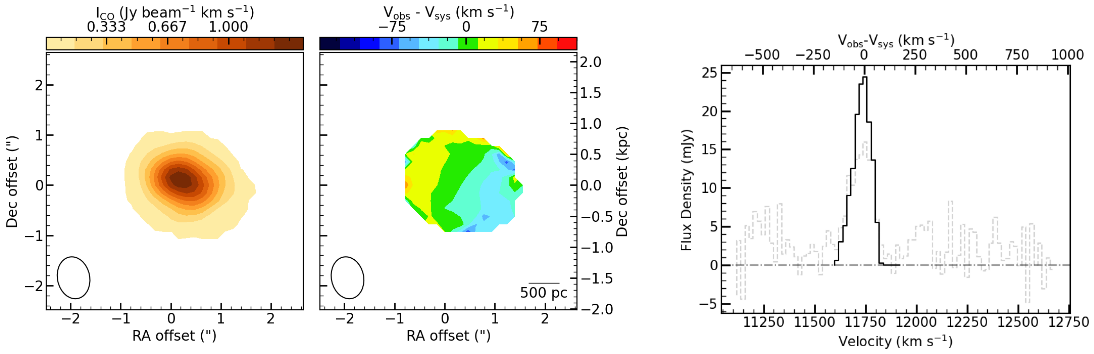

Figure 3.9: As in Figure 3.8, but for HE1029-1831. The spectrum has been extracted within a box of $2.0'' \times 1.5''$.

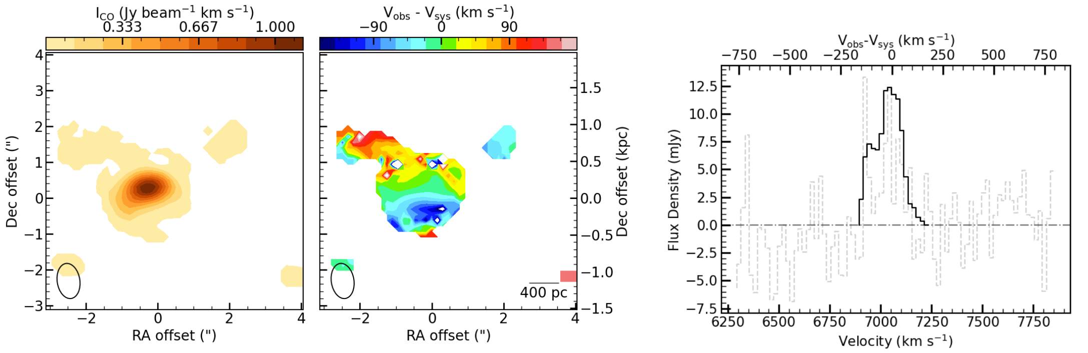

Figure 3.10: As in Figure 3.8, but for HE1108-2813. The spectrum has been extracted within a box of $5.25'' \times 3.75''$.

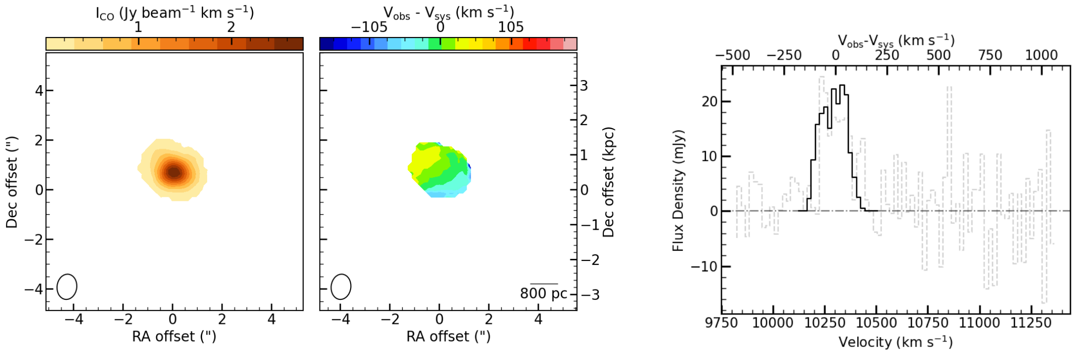

Figure 3.11: As in Figure 3.8, but for the HCO$^+$ detection of HE0433-1028. The spectrum has been extracted within a box of $1.0'' \times 2.5''$.

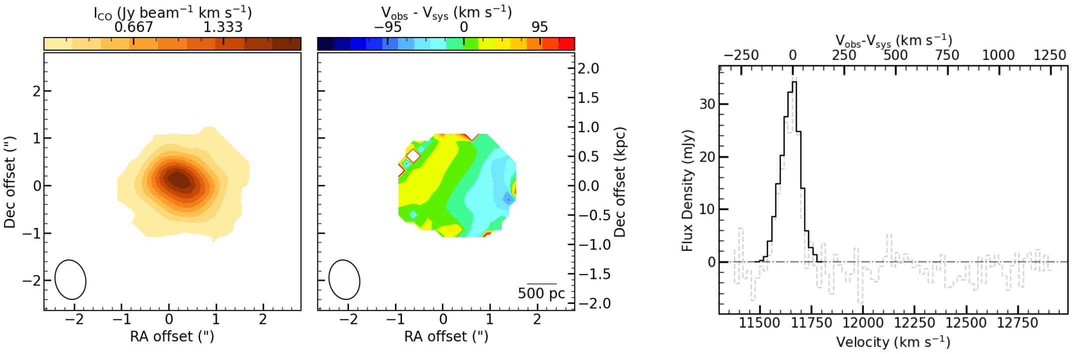

Figure 3.12: As in Figure 3.8, but for the HCO$^+$ detection of HE1029-1831. The spectrum has been extracted within a box of $3.75'' \times 2.40''$.

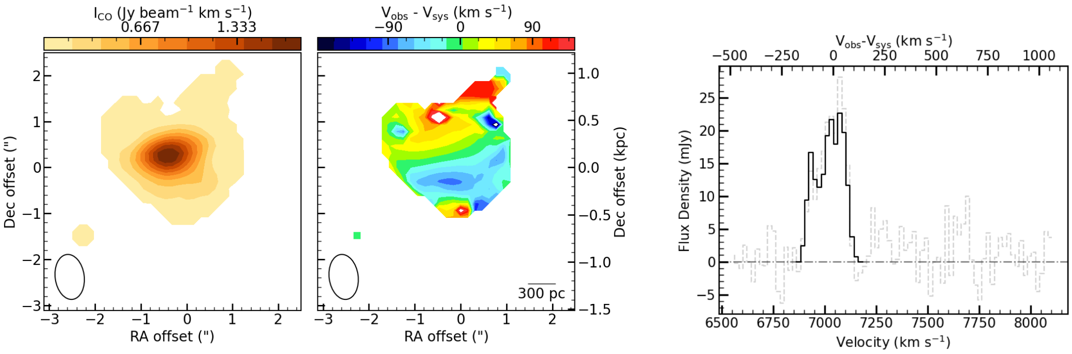

Figure 3.13: As in Figure 3.8, but for the HCO$^+$ detection of HE1108-2813. The spectrum has been extracted within a box of $3.75'' \times 3.60''$.

integrating over the channels defining the corresponding line profiles (illustrated in the bottom-right panels of Figures 3.2 and 3.3). The intensity-weighted mean line-of-sight velocity maps (top-middle panels of Figures 3.2 and 3.3) and intensity-weighted line-of-sight velocity dispersion maps (top-right panels of Figures 3.2 and 3.3) suggest signs of shocks as the molecular gas flows along the x1 orbits of the bar in both sources, and also along the x2 orbit in HE1108-2813. This can be inferred as regions of high mean velocity and velocity dispersion are clearly visible in both cases along the leading edge of the bar and in the central regions, where the transition from x1 to x2 orbits occurs. The major-axis PVDs (bottom-left panels of Figures 3.2 and 3.3) show that the CO gas disk is regularly rotating in both of these sources. There is also an symmetric increase in the velocity in both of these sources which may be associated with non-circular motions in the elliptical x2 orbits at the centre of each system.

As visible in Figures 3.8-3.13, the HCN(4-3) and HCO$^+$(4-3) emission is unresolved in all the three targets in which these lines have been detected, and thus their moment maps do not yield much information. However, from these moment maps it is clear that the dense gas is concentrated in the nuclear regions of the galaxies where it co-exists with the molecular gas.

3.3.2 STACKING METHODOLOGY

To attempt the detection of the weaker lines (and improve the signal-to-noise of those already detected), I performed a stacking analysis using the STACKARATOR tool [‡] of Davis et al. (submitted). This routine allows to stack the datacubes of extended sources to extract weak lines by means of the velocity field (i.e. moment 1 map) of a bright line detection of the same source. For my targets, I used the velocity information of the ^{12}CO(1-0) when available, the MUSE stellar velocity maps otherwise. For each pixel of the input data cube, the velocity centre is determined using the velocity information of the moment 1 map, and a spectrum extracted and adjusted so that its centre aligns with such velocity reference. The adjusted spectra of each pixel are then co-added with appropriate rebinning to create a single, stacked spectrum. This procedure allows me to improve the average signal-to-noise ratio (S/N) of the HCN(4-3) and HCO$^+$(4-3) detections in HE0433-1028, HE1029-1831 and HE1108-2813 from ~ 3.7 to ~ 4.1 (see Figures 3.4–3.6), whereas the other two targets remain undetected in these lines. The stacking of the CS datacubes allows me to pull out a faint detection in HE1108-2813 (as visible in Figure 3.6). All of the other targets remain undetected in CS(7-6). $^{13}\mathrm{CO}$ is not detected in any of the stacked datacubes. This

---

[‡] `https://github.com/TimothyADavis/stackarator`

Table 3.4: Main properties of the detected lines

Galaxy (1)	$I_{\mathrm{HCN(4-3)}}$ $(\mathrm{Jy\,km\,s^{-1}})$ (2)	$FWHM_{\mathrm{HCN(4-3)}}$ $(\mathrm{km\,s^{-1}})$ (3)	$I_{\mathrm{HCO^+(4-3)}}$ $(\mathrm{Jy\,km\,s^{-1}})$ (4)	$FWHM_{\mathrm{HCO^+(4-3)}}$ $(\mathrm{km\,s^{-1}})$ (5)	$I_{\mathrm{CS(7-6)}}$ $(\mathrm{Jy\,km\,s^{-1}})$ (6)	$FWHM_{\mathrm{CS(7-6)}}$ $(\mathrm{km\,s^{-1}})$	$I_{\mathrm{CO(1-0)}}$ $(\mathrm{Jy\,km\,s^{-1}})$	$I_{\mathrm{CO13(1-0)}}$ $(\mathrm{Jy\,km\,s^{-1}})$
HE0108-4743	<0.93	-	<1.09	-	<1.17	-	-	-
HE0433-1028	2.25 ± 0.11	114	2.39 ± 0.12	111	<1.58	-	56.5 ± 0.03	<1.96
HE1029-1831	0.60 ± 0.09	20.5	2.48 ± 0.16	113	<1.23	-	-	-
HE1108-2813	0.78 ± 0.06	106	1.53 ± 0.06	115	0.42 ± 0.06	108	25.2 ± 0.05	<2.99
HE1353-1917	<0.38	-	<0.50	-	<0.51	-	-	<2.05

Notes: (1) Galaxy name. (2)-(6) HCN(4-3), HCO$^+$(4-3), CS(7-6), CO(1-0) and $^{13}\mathrm{CO}$(1-0) line intensities and associated uncertainties. All but CO(1-0) values are those obtained after stacking (see Section 3.3.2).

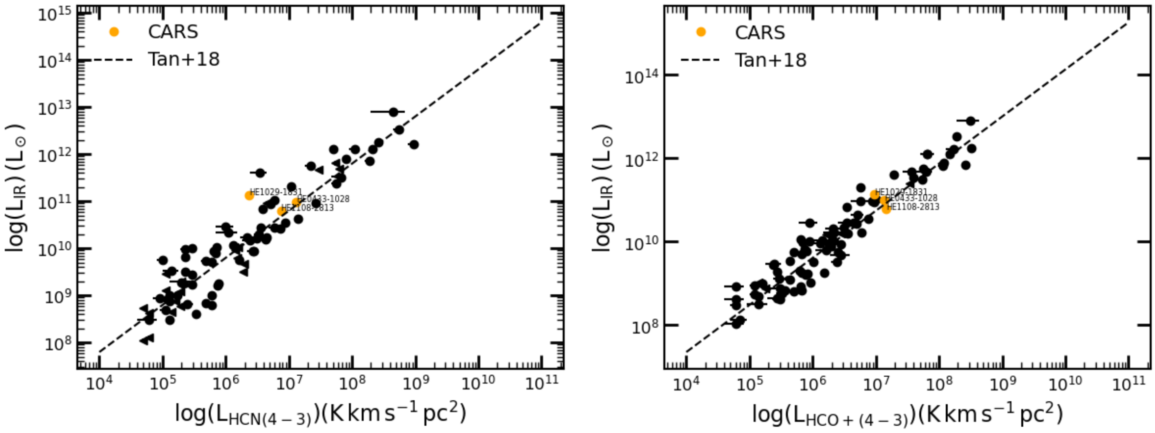

Figure 3.14: Relation between the HCN(4-3) (left) and HCO$^+$(4-3) (right) luminosity and the IR luminosity from star formation. I additionally plot the points and relation from Tan et al. (2018).

is not surprising, as the ALMA band 3 observations were tailored to detect $^{12}\mathrm{CO}$ (which is typically $\gtrsim 10-20$ times brighter than its isotopologue). The integrated flux densities and full width half maxima (FWHM) of the detected HCN(4-3), HCO^+(4-3) and CS(7-6) lines were obtained by performing a single Gaussian fit on their stacked spectra using the Markov chain Monte Carlo (MCMC) code GASTIMATOR[§]. The upper-limits for non-detections were estimated using the relation from Koay et al. (2016):

$$I \leq 3\sigma\Delta v_{\mathrm{FWHM}}\sqrt{\frac{\Delta v}{\Delta v_{\mathrm{FWHM}}}}. \tag{3.1}$$

Where σ is the rms noise level, Δv is the channel width and Δv_{FWHM} is the expected FWHM of the emission line. In Table 3.4 I list the obtained values for all the targets.

3.3.3 GAO-SOLOMON RELATION

In Figure 3.14 I relate the HCN(4-3) and HCO$^+$(4-3) luminosities of HE0433-1028, HE1029-1831 and HE1108-2813 with the infrared luminosities derived from their star

---

[§] `https://github.com/TimothyADavis/GAStimator` formation rates, using the revised version of the Gao and Solomon relation from Tan et al. (2018). I estimated the infrared luminosities of my targets by inverting the relation (Gao & Solomon, 2004b)

$$\mathrm{SFR} \approx 2 \times 10^{-10} (L_{\mathrm{IR}}/\mathrm{L}_{\odot}) \mathrm{M}_{\odot} yr^{-1}. \tag{3.2}$$

The star formation rates are taken from Smirnova-Pinchukova et al. (2022) and are listed in Table 3.1. Despite the potential impact of the AGN on these line-fluxes, I find that all the three CARS targets are consistent with following the Gao and Solomon relations. This will be discussed further in Section 3.4.

3.3.4 GAS EXCITATION CLASSIFICATION

Optical BPT diagrams

To understand the dominant ionisation mechanism(s) of the warm ionised medium (WIM) in the 3 targets with corresponding ALMA data, I produced BPT diagrams using the available MUSE IFU CARS data (see Section 3.2.3 for details).

In a classic BPT diagram (Baldwin et al., 1981), the $[\mathrm{NII}]\lambda 6583/\mathrm{H}\alpha$ and $[\mathrm{OIII}]\lambda 5007/\mathrm{H}\beta$ ratios are used as proxies to classify objects as either star formation (HII), composites, low-ionisation nuclear emission region (LINER) or AGN dominated. In particular, to discriminate between star formation-dominated and composite regions, I used the following equation (derived from the observations presented in Kauffmann et al., 2003):

$$\log([\mathrm{OIII}]/\mathrm{H}\beta = 0.61/(\log([\mathrm{NII}]/\mathrm{H}\alpha) - 0.05) + 1.3. \tag{3.3}$$

On the other hand, to separate between composite and AGN/LINER regions, I adopted the following relation (defined from photoionization and stellar population synthesis modeling in Kewley et al., 2001):

$$\log([\mathrm{OIII}]/\mathrm{H}\beta = 0.61/(\log([\mathrm{NII}]/\mathrm{H}\alpha) - 0.47) + 1.19. \tag{3.4}$$

I then used the equation presented in Schawinski et al. (2007) to distinguish between AGN and LINER regions:

$$\log([\mathrm{OIII}]/\mathrm{H}\beta = 1.05 \log([\mathrm{NII}]/\mathrm{H}\alpha) + 0.45. \tag{3.5}$$

Global BPT diagrams of the targets were produced using the definitions illustrated above. In addition, I also produced the same diagnostic diagrams for the nuclear regions, which were obtained by including only the area of the IFU data cubes within one ALMA beam. This was done to probe the scales that are most likely to be impacted by the AGN, ensuring also a comparison on similar scales both in the optical and the sub-mm. The obtained global and nuclear BPT diagrams are shown in Figure 3.7, where each point represents one pixel in the MUSE maps. The colours of the global BPTs indicate the density of points in an area, with brighter points for denser areas.

The BPT diagnosis identifies the AGN as the dominant ionisation mechanism in the nuclear regions of HE0433-1028, and a combination of star formation and AGN (i.e. composite) in those of HE1029-1831 and HE1108-2813. This thus suggests that, in these latter sources, the optical ionisation has large contributions from star formation alongside the impact of the bright AGN. This is not especially surprising, as these objects are highly star forming, with SFRs of 10-30 $M_{\odot}$ yr^{-1} (see Table 3.1).

Additionally, I studied the AGN diagnostic diagrams proposed in Veilleux & Osterbrock (1987), the so-called VO87-OI and VO87-SII. These use the $[\mathrm{OI}]\lambda6300/\mathrm{H}\alpha$, $[\mathrm{OIII}]\lambda5007/\mathrm{H}\beta$ or $[\mathrm{SII}]\lambda67177/\mathrm{H}\alpha$ ratios to classify objects as either star forming, LINER or Seyfert-dominated. I find that the VO87-OI and VO87-SII diagrams are in good agreement with the BPT classification illustrated in Figure 3.7, thus I do not show or further discuss them here.

sub-mm HCN diagram

To make a comparison with the optical classification, I produce the submm-HCN diagnostic diagram using the HCN(4-3)/CS(7-6) and HCN(4-3)/HCO+(4-3) ratios. As described in Section 3.3.1, I detect all these three lines only in HE1108-2813, as CS(7-6) is not detected in HE0433-1028 and HE1029-1831. For these latter sources, I used upper limits on the CS(7-6) line to place lower limits on the HCN(4-3)/CS(7-6) ratio.

The submm-HCN diagram with these three targets included is shown in Figure 3.15, with the points coloured based on their BPT classification. I additionally plot also the data from Zhang et al. (2014) and Izumi et al. (2016a). I find all three of my sources fall in the starburst region of the diagram though the two lower limits could move upwards. In HE1108-2813, the galaxy in which I detect all the required lines, the two diagrams agree on the excitation mechanism, as both predict star formation excitation to be important. My other two systems only have lower limits on the HCN/CS axis, making it harder to judge agreement between the two diagrams. Both sources have lower HCN/HCO^{+} ratios than any of the AGN sources from Izumi et al. (2016a). HE0433-1028 my source which is classified as AGN dominated in the optical BPT diagram is, however, the most similar to

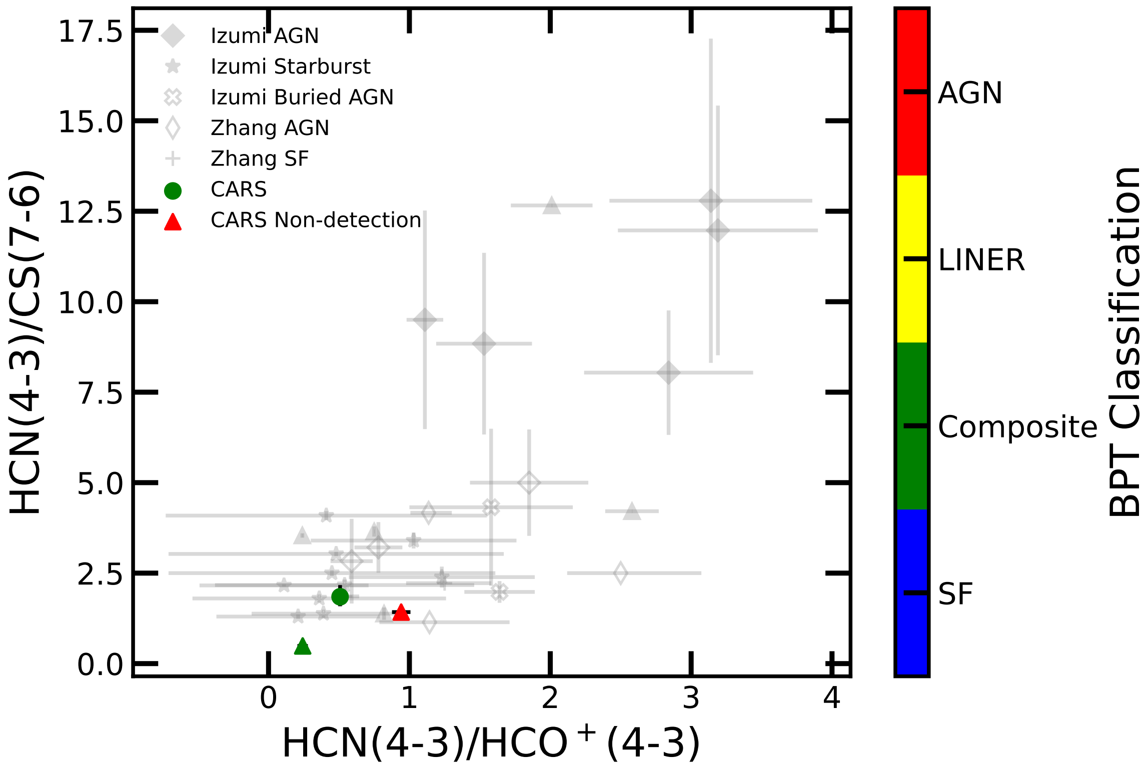

Figure 3.15: Submm-HCN diagnostic diagram. The three CARS targets for which this analysis has been carried out are plotted in green and red, as labelled by the colour bar on the right (and based on their BPT classification). I also plot on the background the data from Izumi et al. (2016a) and Zhang et al. (2014). Triangles represent lower limits and open symbols lower resolution observations

the AGN in this ratio. If its true HCN/CS line ratio were significantly higher than my lower limit, then within error it would be fully consistent with AGN excitation dominating also in the dense gas. These results will be further discussed in Section 3.4.

3.4 DISCUSSION

In this work I present observations of the CO, HCN, HCO$^+$ and CS emission from 5 AGN from CARS.

The large scale molecular discs of these systems show a variety of different morphologies, with bars being important in several cases. The denser gas tracers are only detected towards the nuclei, close to the AGN where the gas density is highest.

In Section 3.3.3 I found that the 3 sources with HCN(4-3) and HCO$^+$(4-3) detections follow known star formation relations. This indicates that if the HCN abundance has been enhanced due to the presence of an AGN, as speculated by Izumi et al. (2016a), it has not been enhanced enough to effect global scaling relations in log-log space.

In Sections 3.3.4 and 3.3.4 I compared the BPT and sub-mm diagnostics to identify the excitation mechanism of the optical ionised and molecular gas lines. I find all three of my sources fall in the starburst region of the diagram though the two lower limits could move upwards. HE1108-2813, the galaxy in which I detect all the required lines, the two diagrams agree on the excitation mechanism, as both predict star formation excitation to be important. My other two systems only have lower limits on the HCN/CS axis, making it harder to judge agreement between the two diagrams. If the true HCN/CS ratio of HE0433-1028 my source which is classified as AGN dominated in the optical BPT diagram were significantly higher than my lower limit, then within error it would be fully consistent with AGN excitation dominating also in the dense gas. This would then mean the optical BPT diagram and sub-mm HCN diagram are in good agreement with each other. I stress that this cross check has only been performed on a very small sample of three sources and this, along with the non-detection of some lines, makes it hard to draw solid general conclusions. Further comparisons with deeper observations on larger samples are needed to study this further.

In optical classifications like the BPT the difference in ionised gas line ratios in star-forming and active galaxies is due to the conditions of the ISM, the gas-phase abundance and the different ionization processes. In star-forming galaxies the line ratios are reproduced by photoionzation models that have O and B stars as the main sources of ionization (Kewley et al., 2001; Nagao et al., 2006; Stasińska et al., 2006; Levesque et al., 2010; Sánchez et al., 2015). AGN typically have higher ratios because the accretion processes can produce higher-energy photons which can in turn induce more heating in the narrow line region (NLR), thus causing an increase in the collisionally excited lines (Stasińska et al., 2006). This explains why my three sources, which are all type 1 AGN (selected via the presence of broad lines, not using these line ratios), show signs of AGN ionisation in their BPT diagrams (see Figure 3.7).

By using non local thermodynamic equilibrium (LTE) radiative transfer models, Izumi et al. (2016a) found that the high HCN to HCO^{+} and HCN to CS dense molecular line ratios of AGN are likely due to their enhanced HCN abundance compared to star forming galaxies. This also indicates a higher gas density in AGN with respect to star forming galaxies. The exact mechanism that causes this HCN abundance in AGN is not clear with Izumi et al. (2016a) suggesting that high temperature chemistry, the effects of metallicity and chemical abundances, IR pumping or time dependent chemistry as potential solutions.

My findings are consistent with the idea that AGN can be an important excitation mechanism at sub-mm wavelength. It indicates that the AGN radiation can penetrate both the low density ionised gas (as probed by the BPT classification) and the high density molecular gas (as probed by the sub-mm HCN classification). It seems that the hard X-ray photons produced by nuclear activity can both ionize the diffuse gas and penetrate deep into the denser molecular gas clouds, heating them. This heating could then induce high temperature chemistry that leads to the increase in HCN abundance as discussed in Izumi et al. (2016a).

Esposito et al. (2022) studied the CO emission in a sample of 35 local active galaxies to investigate the main source of molecular gas heating in these sources. In their study they found that on the scales of $\approx$250pc a combination of star formation and AGN ionisation is needed to reproduce the CO emission observed, in agreement with what I find here.

On the other hand, some works have shown that AGN radiation is absorbed by the outer layers of dense gas clouds which prevents the AGN radiation from penetrating deep into the molecular cloud (Roos et al., 2015; Bieri et al., 2017; Meenakshi et al., 2022). If this remains true in my sources then perhaps the AGN could be heating the gas by inducing shocks in the clouds that can excite the dense gas (Namekata et al., 2014; Meenakshi et al., 2022). However, I caution that these shocks would need to be affecting the dense and ionized gas simultaneously, which seems less likely given that the dense and ionized gas may not co-spatial.

Finally, the AGN could potentially be driving turbulence or producing cosmic rays which have both been shown to impact molecular clouds (Federrath & Klessen, 2012, 2013;

Crocker et al., 2021).

My results are consistent with the idea that AGN may be able to directly or indirectly excite the gas in dense molecular clouds. However, when strong star formation is present this can easily dominate the excitation, of both gas phases, even close to a luminous AGN.

3.5 CONCLUSIONS

Using CARS ALMA data I have observed dense and molecular gas tracers in 5 nearby type 1 (unobscured) AGN. I have found that the large scale molecular discs of these systems show a variety of different morphologies, with bars being important in several cases. The denser gas is only detected towards the nuclei, close to the AGN where the gas density is highest.

I have used the observations of the dense gas tracers to study their use as an AGN diagnostic tool. It has been reported in previous studies that the HCN/HCO+ and HCN/CS ratios can be used to separate AGN from star forming galaxies using a *sub-mm HCN diagram*, as HCN can be enriched by chemical pathways at high temperatures.

I find that all three of the sources where the dense gas tracers were detected follow known relations between the amount of dense gas and star-formation. This indicates that if the HCN abundance has been enriched it has not been enhanced enough to effect global scaling relation.

When studying the *sub-mm HCN diagram* I am limited by the lack of detection of CS(7-6) in many of my sources, but in those that I could study I find general agreement between optical and sub-mm classification gas excitation mechanisms.

This suggests that that AGN can contribute to the excitation of both the low density gas in the WIM and high density molecular gas clouds simultaneously, perhaps through X-ray, cosmic ray or shock heating mechanisms.

Further observations of dense gas around AGN are clearly needed to further populate the sub-mm HCN diagram and to allow further cross-comparisons with other AGN classification schemes and studies of AGN excitation at different wavelengths.

CHAPTER 4

Fundamental plane of black hole accretion

> *"It's a great time to be alive. I guess."*
>
> -Holly Davies

The so-called "fundamental plane of BH accretion" (heareafter FP) is an empirical correlation between the SMBH masses (M_{BH}), 5 GHz radio ($L_{5\ \mathrm{GHz}}$) and 2 - 10 keV X-ray ($L_{\mathrm{X,2\text{-}10}}$) luminosities, which was initially reported by Merloni et al. (2003) and Falcke et al. (2004). The origin of the FP is still debated, but it is widely believed to carry information on the physics of SMBH accretion (see e.g. Gültekin et al., 2019). However, the scatter around this correlation varies significantly depending on the sample and the method used to fit the plane, reaching values up to 0.88 dex (e.g. Merloni et al., 2003; Gültekin et al., 2009; Plotkin et al., 2012; Saikia et al., 2015; Gültekin et al., 2019, and references therein). Furthermore, the nature of the radio emission in the FP is not yet well understood (potentially arising from compact jets or complex shock dynamics). All the above somehow limit the diagnostic power of the FP. The radio FP is shown in Figure 4.1.

The origin of the mm/sub-mm emission from AGN is still not clear with a number of different mechanisms potentially given rise to the emission. These include dust heated by the AGN, outflow-driven shocks or jets. With the high resolution observation being provided by ALMA we can now start to disentangle the AGN mm emission from the mm emission of the wider galaxy to start to understand the underlying emission process.

In this chapter, I report the discovery of a FP at millimetre wavelengths, namely the existence of a tight correlation between the nuclear (i.e. $\ll 100$ pc) mm luminosities ($L_{\nu,\mathrm{mm}}$), M_{BH} and intrinsic $L_{\mathrm{X,2\text{-}10}}$, which is found to hold for both high- and low-luminosity AGN (within $z \lesssim 0.05$). I also present the analysis of the physics underlying such correlation,

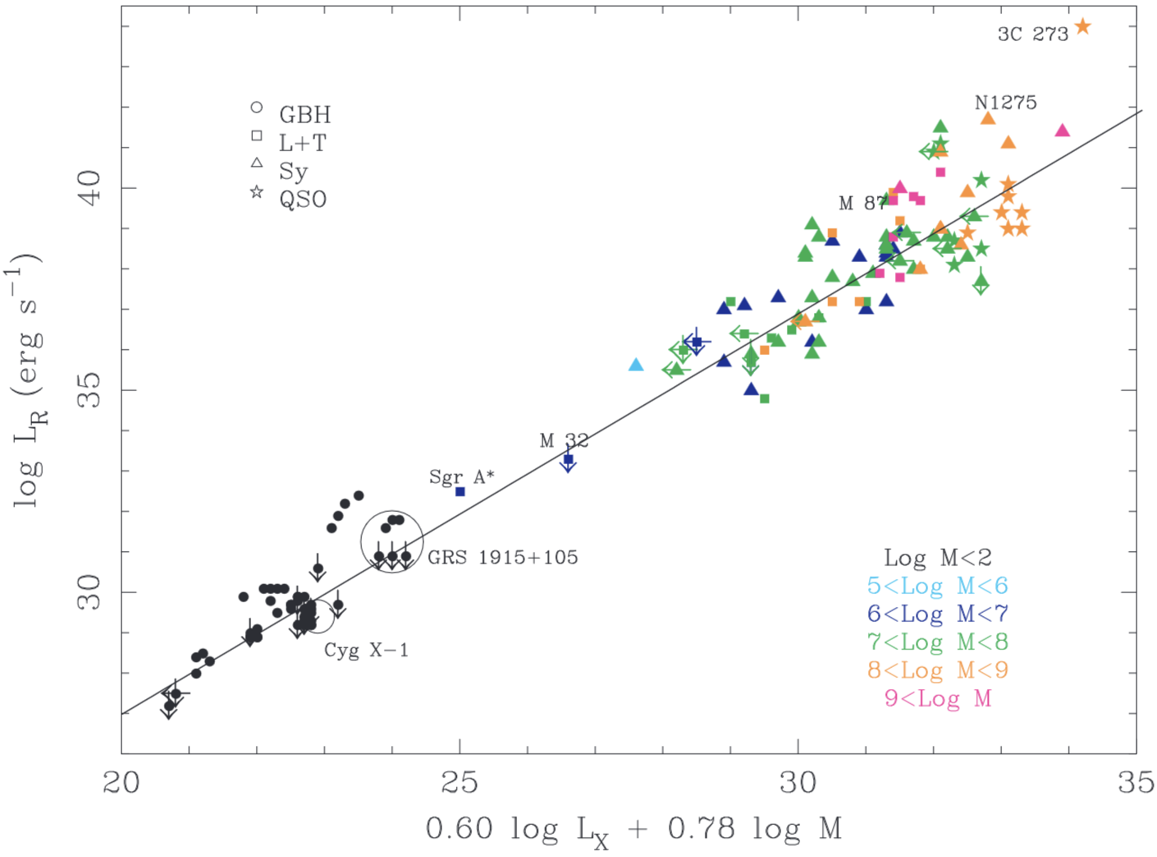

Figure 4.1: Edge on view of the radio fundamental plane with the solid line being the best fitting function. Taken from Merloni et al. (2003)

and discuss how these results may have profound implications for our understanding of BH accretion in different AGN types.

4.1 PRIMARY SAMPLE AND DATA

The sample was primarily drawn from the mm-Wave Interferometric Survey of Dark Object Masses (WISDOM) project, which mainly exploits high-resolution Atacama Large Millimeter/submillimeter Array (ALMA) CO observations to dynamically estimate SMBH masses in a varied sample of galaxies (e.g. Davis et al., 2017). It included 31 WISDOM galaxies (see Table 4.1) at $z \lesssim 0.03$, spanning a range of AGN bolometric luminosities ($L_{\rm bol} = 10^{41}$ – 10^{46} erg s^{-1}) and mostly (but not exclusively) having very low rates of accretion onto their central SMBHs ($\dot{M} \lesssim 10^{-3}\ \dot{M}_{\rm Edd}$; Elford et al., 2024). As such, most of these objects are classified as low-luminosity AGN (LLAGN; Ho et al., 2008). To increase the statistics, this is supplemented with a further 17 galaxies (see Table 4.1), selected from the literature to have dynamical SMBH masses, existing high-resolution ALMA 1 mm and high-quality X-ray data. The majority of these are nearby ellipticals and span ranges of $L_{\rm bol}$ and $\dot{M}$ similar to those of the WISDOM sources. Hereafter, these 31 WISDOM plus 17 literature sources are referred to as the *primary sample*.

The 1 mm luminosities of the primary sample sources were derived from high-angular-resolution ALMA Band 6 continuum observations, taken between 2013 and 2021 as part of a large number of projects. All data were reduced using the Common Astronomy Software Applications (CASA) pipeline (McMullin et al., 2007), adopting a version appropriate for each dataset and a standard calibration strategy. For more details on the data reduction see Davis et al. (2022).

For each dataset, continuum images were produced by combining the continuum spectral windows (SPWs) and the line-free channels of the line SPW (when included) using the CASA task TCLEAN in multi-frequency synthesis (MFS) mode. The resulting continuum maps have synthesised beams ranging from $0\farcs042$ to $0\farcs723$, corresponding to 6 – 330 pc (average spatial resolution ≈ 25 pc). For each source, the continuum flux density $f_{\rm mm}$ from the innermost synthesised beam is measured, coincident with the galaxy core. The mm luminosities were then estimated as $L_{\nu,{\rm mm}} = 4\pi D_{\rm L}^2 f_{\rm mm} \nu_{\rm obs}$, where $D_{\rm L}$ is the luminosity distance and $\nu_{\rm obs}$ the observed frequency (between 231 and 239 GHz). As all the data were obtained with long-baseline configurations, extended dust emission is resolved out. Typically only a point-like source at each galaxy centre is detected, arising from unresolved core emission. In 3 (out of 48) galaxies, the emission is slightly resolved, making the

Table 4.1: Full list and main parameters of the galaxies in the primary sample.

Sample (1)	Galaxy (2)	D (Mpc) (3)	log$M_{\rm BH}$ (M$_\odot$) (4)	Δlog$M_{\rm BH}$ (dex) (5)	Method (6)	log$L_{\nu,{\rm mm}}$ (erg s^{-1}) (7)	ALMA project (8)	log$L_{\rm X,2\text{-}10}$ (erg s^{-1}) (9)	Δlog$L_{\rm X,2\text{-}10}$ (dex) (10)
WISDOM	FRL49	85.7	8.20	0.2	Dyn	39.28	a	43.27	0.04
	FRL1146	136.7	7.85	0.30	$\sigma_\star$	< 38.76	a	43.41	0.04
	MRK567	140.6	7.48	0.30	$\sigma_\star$	39.39	a	–	–
	NGC0404	3.0	5.74	0.30	Dyn	35.99	b	37.20	0.04
	NGC0449	66.3	8.77	0.30	$\sigma_\star$	38.87	c	40.58	0.04
	NGC0524	23.3	8.60	0.32	Dyn	38.94	d	38.55	0.04
	NGC0708	58.3	8.30	0.30	Dyn	39.10	d	39.39	0.04
	NGC1194	53.2	7.85	0.10	Dyn	39.09	e	41.54	0.04
	NGC1387	19.9	6.90	0.20	Dyn	38.07	c	39.33	0.04
	NGC1574	19.3	8.05	0.20	Dyn	38.55	f	–	–
	NGC2110	35.6	8.77	0.30	$\sigma_\star$	39.89	g	42.71	0.04
	NGC3169	18.7	7.85	0.30	$\sigma_\star$	38.53	h	41.53	0.04
	NGC3351	10.0	5.85	0.30	$\sigma_\star$	< 37.25	i	38.74	0.04
	NGC3368	18.0	6.87	0.10	Dyn	< 37.73	g	39.30	0.05
	NGC3607	22.2	8.14	0.15	Dyn	38.58	h	39.16	0.04
	NGC4061	94.1	9.30	0.30	Dyn	39.78	j	–	–
	NGC4429	16.5	8.17	0.10	Dyn	38.08	i	39.12	0.10
	NGC4435	16.5	7.40	0.20	Dyn	37.76	h	39.47	0.04
	NGC4438	16.5	7.70	0.30	$\sigma_\star$	37.61	h	39.08	0.04
	NGC4501	14.0	6.79	0.30	$\sigma_\star$	37.90	k	40.09	0.04
	NGC4697	11.4	7.20	0.10	Dyn	37.25	h	38.52	0.04
	NGC4826	7.4	6.20	0.11	Dyn	36.99	i	37.96	0.11
	NGC5064	34.0	8.39	0.30	$\sigma_\star$	37.96	k	–	–
	NGC5765b	114.0	7.32	0.30	$\sigma_\star$	39.06	e	40.73	0.05
	NGC5806	21.4	6.95	0.30	$\sigma_\star$	< 37.26	c	–	–
	NGC5995	107.5	8.55	0.30	$\sigma_\star$	39.51	a	43.39	0.04
	NGC6753	42.0	8.42	0.30	$\sigma_\star$	< 37.82	k	–	–
	NGC6958	30.6	7.89	0.30	$\sigma_\star$	39.47	k	–	–
	NGC7052	51.6	8.91	0.30	$\sigma_\star$	40.13	j	40.02	0.05
	NGC7172	33.9	8.05	0.30	$\sigma_\star$	39.44	l	43.00	0.05
	PGC043387	95.8	8.42	0.30	$\sigma_\star$	38.90	h	–	–
Literature	**Circinus**	4.2	6.23	0.08	Dyn	37.57	m	42.20	0.04
	IC1459	25.9	9.45	0.30	Dyn	40.60	n	40.91	0.10
	M87	16.5	9.81	0.04	Dyn	40.75	o	40.56	0.05
	NGC1316	19.9	8.23	0.08	Dyn	38.73	p	39.65	0.04
	NGC1332	22.3	8.82	0.04	Dyn	38.91	q	39.15	0.08
	NGC1380	17.1	8.17	0.17	Dyn	38.53	r	39.07	0.04
	NGC3227	17.0	7.18	0.17	Dyn	37.70	s	41.95	0.09
	NGC3245	21.5	8.32	0.10	Dyn	38.42	t	38.88	0.09
	NGC3393	53.6	7.52	0.03	Dyn	38.34	e	40.92	0.09
	NGC3489	12.0	6.78	0.07	Dyn	36.77	u	39.07	0.09
	NGC3504	13.6	7.00	0.07	Dyn	38.38	v	41.05	0.09
	NGC3585	20.6	8.52	0.13	Dyn	37.89	t	38.85	0.04
	NGC4374	18.5	8.96	0.05	Dyn	39.84	w	39.95	0.04
	NGC4388	19.8	6.94	0.01	Dyn	38.88	x	42.33	0.05
	NGC4395	4.4	5.60	0.31	Dyn	35.85	y	39.91	0.05
	NGC6861	27.3	9.30	0.22	Dyn	39.52	r	39.29	0.04
	UGC2698	91.0	9.39	0.12	Dyn	39.53	z	40.46	0.09

Notes: (1) Sub-sample. (2) Galaxy name. (3) Most accurate galaxy distance. (4), (5) and (6) SMBH mass, uncertainty, and measurement method. "Dyn" refers to dynamical measurements, "$\sigma_\star$" to estimates from the $M_{\rm BH} - \sigma_\star$ relation of van den Bosch (2016). (7) Millimetre luminosity. Errors are not reported because they are simply dominated by flux calibration uncertainties, which are ≈10% for ALMA Band 6. (8) Project code of the ALMA continuum observations, where a: 2017.1.00904.S, b: 2017.1.00572.S, c: 2016.1.00437.S, d: 2017.1.00391.S, e: 2016.1.01553.S, f: 2015.1.00419.S, g: 2016.1.00839.S, h: 2015.1.00598.S, i: 2013.1.0049.S, j: 2018.1.00397.S, k: 2015.1.00466.S, l: 2019.1.00363.S, m: 2018.1.01321.S, n: 2015.1.01572.S, o: 2015.1.01352.S, p: 2017.1.01140.S, q: 2015.1.00896.S, r: 2013.1.00229.S, s: 2016.1.00254.S, t: 2017.1.00301.S, u: 2017.1.00766.S, v: 2017.1.00964.S, w: 2013.1.00828.S, x: 2012.1.00139.S, y: 2015.1.00597.S, z: 2016.1.01010.S. (9) and (10) intrinsic (absorption-corrected) $2-10$ keV X-ray luminosity, and associated uncertainty. Galaxies highlighted in bold have their $L_{\rm X,2\text{-}10}$ taken from the catalogue of Bi et al. (2020).

measurements more uncertain. Removing these 3 objects, however, does not affect the results in any way.

The obtained $L_{\nu,\mathrm{mm}}$ are listed in Table 4.1.

The intrinsic (absorption-corrected) 2–10 keV luminosities ($L_{\mathrm{X,2\text{-}10}}$) of the primary sample sources were retrieved from the literature, as detailed in Elford et al. (2024). In short, eight of these galaxies have no X-ray data available and were thus not considered in the parts of the analysis where $L_{\mathrm{X,2\text{-}10}}$ was required. For the vast majority of the objects with X-ray data (33/40), the adopted $L_{\mathrm{X,2\text{-}10}}$ was derived from *Chandra* observations, including only emission from the unresolved AGN core. For most of the *Chandra*-observed objects (26/33), accurate (intrinsic) nuclear $L_{\mathrm{X,2\text{-}10}}$ were retrieved from the catalogue of Bi et al. (2020, see also Table 4.1).

Dynamically-determined SMBH masses (from stellar, ionised gas, molecular gas and/or maser kinematics) are available for a total of 31 primary sample sources (see Table 4.1). For the remaining 17 galaxies, M_{BH} were estimated using the M_{BH} – $\sigma_\star$ relation of van den Bosch (2016), where $\sigma_\star$ is the stellar velocity dispersion within one effective radius. This was retrieved from the compilations of van den Bosch (2016) and Cappellari et al. (2013a) when available, from the HyperLeda database otherwise (`http://leda.univ-lyon1.fr`). Crucially, although constructed based on data availability only (and thus not meant to be complete in any statistical sense), the primary sample spans four orders of magnitude in SMBH mass.

4.2 THE MM FUNDAMENTAL PLANE

As illustrated in Fig. 4.2 (left panel), the SMBH masses of the primary sample galaxies strongly correlate with their $L_{\nu,\mathrm{mm}}$. A power law was fitted to the observed trend, using the LTS_LINEFIT routine (Cappellari et al., 2013a). This combines the least-trimmed-squares (LTS) robust regression technique (Rousseeuw, 1984) with a least-squares fitting algorithm, and allows for intrinsic scatter and uncertainties in all coordinates. The resulting best-fitting power law is:

$$\log_{10}\left(\frac{M_{\mathrm{BH}}}{M_\odot}\right) = (0.79 \pm 0.08)\left[\log_{10}\left(\frac{L_{\nu,\mathrm{mm}}}{\mathrm{erg\,s^{-1}}}\right) - 39\right] + (8.2 \pm 0.1)\,, \tag{4.1}$$

with an observed scatter (σ_{obs}) of 0.55 dex and an estimated intrinsic scatter (σ_{int}) of 0.51 ± 0.08 dex. When including $L_{\mathrm{X,2\text{-}10}}$, the existence of a tighter correlation is discovered (Fig. 4.2, right panel). In this case, the LTS_PLANEFIT routine (Cappellari et al., 2013a) is used to find the best-fitting plane in the $(\log M_{\mathrm{BH}}, \log L_{\mathrm{X,2\text{-}10}}, \log L_{\nu,\mathrm{mm}})$ space:

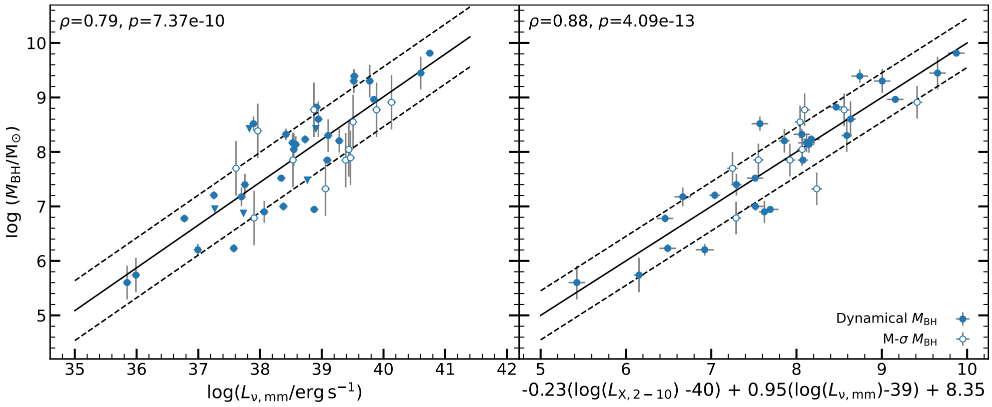

Figure 4.2: Correlation between $M_{\rm BH}$ and $L_{\nu,{\rm mm}}$ (left panel) and edge-on view of the $M_{\rm\ BH}$-$L_{\rm X,2\text{-}10}$-$L_{\nu,{\rm mm}}$ correlation (right panel) for the primary sample galaxies. In both panels, filled blue circles show sources with dynamical $M_{\rm BH}$ measurements, open circles sources with $M_{\rm BH}$ from the $M_{\rm BH} - \sigma_\star$ relation of van den Bosch (2016). Error bars are plotted for all points but some are smaller than the symbol used. The best-fitting power-laws (Section 4.2) are overlaid as a black solid lines, the observed scatter as black dashed lines. The correlation coefficients ρ and p-values of the performed Spearman rank analysis are reported in the top-left corner of each panel.

$$\log_{10}\left(\frac{M_{\rm BH}}{M_\odot}\right) = (-0.23 \pm 0.05)\left[\log_{10}\left(\frac{L_{\rm X,2\text{-}10}}{\rm erg\,s^{-1}}\right) - 40\right]$$
$$+(0.95 \pm 0.07)\left[\log_{10}\left(\frac{L_{\nu,{\rm mm}}}{\rm erg\,s^{-1}}\right) - 39\right] + (8.35 \pm 0.08)\,, \tag{4.2}$$

with $\sigma_{\rm obs} = 0.45$ dex and $\sigma_{\rm int} = 0.40 \pm 0.07$ dex. it has been verified that this multi-variate plane fit provides a significantly better predictor for $M_{\rm BH}$ than the simple line fit, having a $\Delta_{\rm BIC} >>$10 (where $\Delta_{\rm BIC}$ is the difference in the Bayesian information criterion between the line and plane fits). For both correlations, a Spearman rank analysis was also performed to quantify their statistical significance, and show the resulting correlation coefficients in the top-left corner of each panel of Fig. 4.2. Since the nuclear mm and X-ray emission from AGN is known to be time variable (typically by a factor of $2-3$ over year timescales; Prieto et al., 2016; Fernández-Ontiveros et al., 2019; Behar et al., 2020), variability likely dominates the observed scatters (and thus the underlying correlations may be tighter). By analogy with the previous FP, the correlation in the right panel of Fig. 4.2 is dubbed as the "mm fundamental plane of BH accretion" (hereafter mmFP).

It should be noted that the error budget of the derived $L_{\nu,\ {\rm mm}}$ is dominated by the ALMA flux calibration uncertainties (≈10% for Band 6 data). These are, however, much smaller than the estimated intrinsic scatters of the correlations in Fig. 4.2 (see above), and thus have a negligible impact on my results. It should also be noted that the $L_{\mathrm{X,2\text{-}10}}$ of the five X-ray observed sources without available *Chandra* data could be slightly overestimated, due to contamination from diffuse hot gas in the galactic and circum-galactic medium (CGM; although this mainly emits in the $0.3 - 2$ keV range) and/or X-ray binaries. While it has been verified that any such contamination should be minimal (based on the scaling laws of Grimm et al., 2003, Kim & Fabbiano, 2004 and Boroson et al., 2011), it cannot be ruled out entirely. In any case, removing these five sources does not make any relevant change in the best-fitting parameters of the mmFP. The same applies when removing the sources without a robust, dynamical M_{BH} estimate (the best-fitting line and planes are identical, within their respective errors, and the observed scatters become only slightly smaller).

4.2.1 BASS GALAXIES

Although the majority of the primary sample galaxies are LLAGN, a handful are more luminous systems (see Elford et al., 2024), which still follow the mmFP. To investigate whether this result holds more generally, a comparison sample is built from the *Swift*-BAT AGN Spectroscopic Survey (BASS), comprising AGN with median $z = 0.05$, $L_{\mathrm{bol}} = 10^{44}$ erg s^{-1} and $\dot{M} = 0.01 - 0.1\ \dot{M}_{\mathrm{Edd}}$ (Koss et al., 2017). Only the BASS sources for which both ALMA 1 mm observations (with spatial resolutions similar to those of the primary sample) and nuclear intrinsic $L_{\mathrm{X,2\text{-}10}}$ were available were included (88 sources; Kawamuro et al., 2022). The SMBH masses of these objects were taken from the compilation of Koss et al. (2022). The BASS galaxies are typically more distant than those in the primary sample, so their M_{BH} have been estimated with a variety of methods (see Fig. 4.3). However, most of the sources ($50/88$) have their M_{BH} from the $M_{\mathrm{BH}} - \sigma_\star$ relation of Kormendy & Ho (2013). These measurements were re-calibrated using the $M_{\mathrm{BH}} - \sigma_\star$ relation of van den Bosch (2016), for consistency with the 17 primary sample sources without a dynamical SMBH mass estimate.

As illustrated in Fig. 4.4b, the BASS sources are in agreement with the best-fitting mmFP, albeit with a larger observed scatter. A Spearman rank analysis was performed to quantify the statistical significance of this relation for the BASS points alone, and verified that they do show a significant correlation ($p = 0.002$), but with a correlation coefficient (ρ=0.32) smaller than that of the primary sample. Fig. 4.3 suggests that the larger scatter in this population is (at least partly) driven by the M_{BH} uncertainties, as the position of a BASS galaxy with respect to the best-fitting mmFP depends on the method used to estimate its M_{BH}. For instance, sources with M_{BH} from reverberation mapping or broad-line methods are located systematically below the best-fitting line, likely reflecting the different biases in

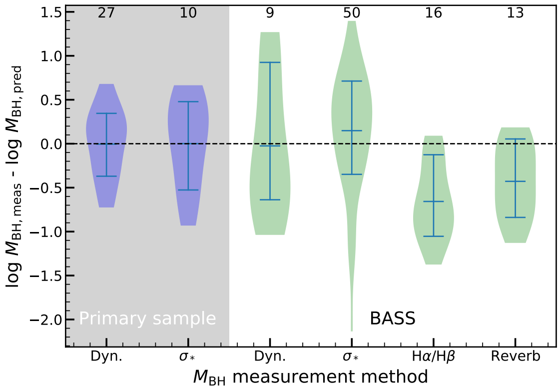

Figure 4.3: Residuals of the primary sample (grey shaded region) and BASS sources (white region) from the best-fitting mmFP, plotted as a function of the SMBH mass measurement method. “Dyn” refers to dynamical mass measurements, “$\sigma_\star$” to estimates from the $M_{\mathrm{BH}} - \sigma_\star$ relation of van den Bosch (2016), “Hα/Hβ” to the broad-line method and “Reverb” to reverberation mapping. Each set of data points is represented by a violin describing the underlying distribution. The number of sources in the mmFP whose M_{BH} has been estimated using that particular method is indicated above each violin. In each case, the blue horizontal lines denote the $18^{\text{ th}}$, 50^{th} and 85^{th} percentiles of the distribution.

place when using such techniques (e.g. Farrah et al., 2023).

4.3 PHYSICAL DRIVERS

The fact that the BASS galaxies are consistent with a relation mainly defined by LLAGN is surprising. To determine the underlying physics, the observed nuclear mm and X-ray luminosities was compared for both the primary sample and BASS sources to those extracted from mock nuclear SEDs arising from both “classic” and radiatively-inefficient (ADAF-like) accretion flows, and from compact radio jets.

4.3.1 TORUS MODEL

AGN in the BASS sample (and a few in the primary sample) have *estimated* accretion rates in the range $\dot{M} \sim 0.01 - 0.1\ \dot{M}_{\mathrm{Edd}}$. According to the standard paradigm, in this type of systems the accretion should occur through the classic geometrically-thin and optically-thick accretion disk surrounded by a dusty torus (e.g. Heckman & Best, 2014). In this scenario, both the mm and the $2 - 10$ keV emission arise from the accretion disc, reprocessed by dust in the torus in the mm and Compton-up scattered by the hot corona in X-rays. To check if this type of model can reproduce the observed mm and X-ray luminosities, the SKIRTOR library was used (Stalevski et al., 2012, 2016). The SED models were retrieved from the SKIRTOR webpage (`https://sites.google.com/site/skirtorus/`), but their spectral coverage (from 300 GHz to 1.24 keV) is slightly shorter than that required for this work. The models were thus expanded to the full range of wavelengths probed here, treating the emission mechanisms self-consistently as prescribed in the original version of the code (i.e. using the same grey-body curve for millimetre emission, and a power-law in the X-ray regime; Yang et al., 2020). The prescriptions of Stalevski et al. (2012, 2016) were followed to scale the models for different $L_{\rm bol}$, in the range $10^{7.5} - 10^{12.5}$ $L_\odot$ (i.e. the range covered by the primary and BASS sources; the torus is expected to disappear at low accretion rates, but the resulting model predictions are nevertheless instructive). For each SKIRTOR SED model, the predicted 1 mm (specifically, the luminosity at 237.5 GHz, that is the median ALMA continuum frequency for both the primary and BASS sources) and intrinsic 2-10 keV luminosities were extracted, and compared them with the measured ones. The resulting predictions are shown in Fig. 4.4a as a hexagonally binned histogram (coloured by mean $L_{\rm bol}$). The luminosities extracted from the torus models reasonably reproduces the slope of the $L_{\rm X,2\text{-}10} - L_{\nu,\rm mm}$ relation of the BASS sources, but with an offset of about two orders of magnitude at a given $L_{\rm bol}$. On the other hand, to explain $L_{\nu,\rm mm}$ of the lower accretion rate galaxies, the mm luminosities in the SKIRTOR models would need to be at least four orders of magnitude larger at a given accretion rate (and thus X-ray luminosity).

4.3.2 ADAF MODEL

To build model SEDs arising from radiatively-inefficient accretion flows around SMBHs, The "LLAGN" model of Pesce et al. (2021, itself a development of previous models by Narayan & Yi 1995a and Mahadevan 1997) were used. In typical LLAGN and some (low-accretion-rate) Seyferts, the classic accretion disk is either absent or truncated at some inner radius (the transition usually happens beyond a few tens of Schwarzschild radii), and replaced by a geometrically-thick two-temperature structure in which the ion temperature is greater than the electron temperature and the accretion occurs at rates well below the Eddington limit (i.e. $\ll 0.01\ \dot{M}_{\rm Edd}$; Narayan & Yi, 1995b; Ho et al., 2008). The electrons in such radiatively-inefficient flows (such as advection-dominated accretion flows; ADAFs) cool down via a combination of self-absorbed synchrotron, bremsstrahlung and inverse Compton radiation, which together give rise to the nuclear SED from the mm to the X-rays. The LLAGN model adopted here solves for the energy balance between the heating and cooling of the electrons in the flow. A set of model SEDs were generated for a grid of SMBH masses (10^6 – 10^{10} M$_\odot$) and Eddington ratios (10^{-7} – 10^{-2}), while all the other free parameters were kept at the defaults discussed in Appendix A of Pesce et al. (2021). The predicted 237.5 GHz and $2-10$ keV luminosities were extracted, as described above. As illustrated by the shape of the model grid in Fig. 4.4a, the mm and X-ray luminosities of all the sources (and thus the observed correlations) are well explained if they arise from an ADAF-like accretion mechanism. The grid is almost aligned with the axes, thus predicting that the mm luminosity primarily depends on $M_{\rm BH}$, while $L_{\rm X,2\text{-}10}$ primarily traces the Eddington ratio. The tighter correlation obtained when including $L_{\rm X,2\text{-}10}$ can be explained by the fact that the slight tilt of the grid is then taken into account, especially at higher Eddington ratios. In Fig. 4.4b, the projection of the ADAF model grid onto the best-fitting mmFP is shown. This latter seems to arise naturally from these models, as an (almost) edge-on view of the 3D ($M_{\rm BH}$, $L_{\rm X,2\text{-}10}$, $L_{\nu,\rm mm}$) relation. It should be noted, however, that keeping the default model parameters from Pesce et al. (2021), the model well predicts the gradient of the mmFP, but is offset by a small amount (i.e. the model overpredicts $L_{\nu,\rm mm}$ at a given SMBH mass by ≈ 0.5 dex). Tweaking the model parameters to reduce the effective radiative efficiency easily removes this offset (e.g. by changing some combination of the effective viscosity, ratio of gas to magnetic pressure, fraction of viscous heating going directly to the electrons, outer radius of the ADAF, and/or power-law index of the mass accretion rate as a function of radius). However, as the correct values of these parameters is not well constrained, the model grid is offset by a constant 0.5 dex in SMBH mass to align it with the observed correlation. It should be stressed that this scaling factor is significantly smaller than the one required for torus models to reproduce the observed trend (see Section 4.3.1), and is well within the uncertainties for the adopted model parameters (see Pesce et al., 2021). Future work exploring the parameters of ADAF-like models in sources with more extensive (sub-)mm coverage will allow to better understand the observed correlation, the small offset, and the physics of accretion onto these SMBHs. This is discussed further in Section 4.4.

4.3.3 COMPACT JET MODEL

Unlike extended jets (where the synchrotron emission is optically-thin), compact radio jets have self-absorbed synchrotron spectra (similar to those from ADAFs) and have been argued to dominate the nuclear SEDs of LLAGN. In some cases, they are preferred over a pure ADAF solution, as this would be overly luminous at near-infrared and optical wavelengths (e.g. Fernández-Ontiveros et al., 2023). To determine if compact jets can explain the observed trends, the BHJET model of Lucchini et al. (2022) is used. Most of the model

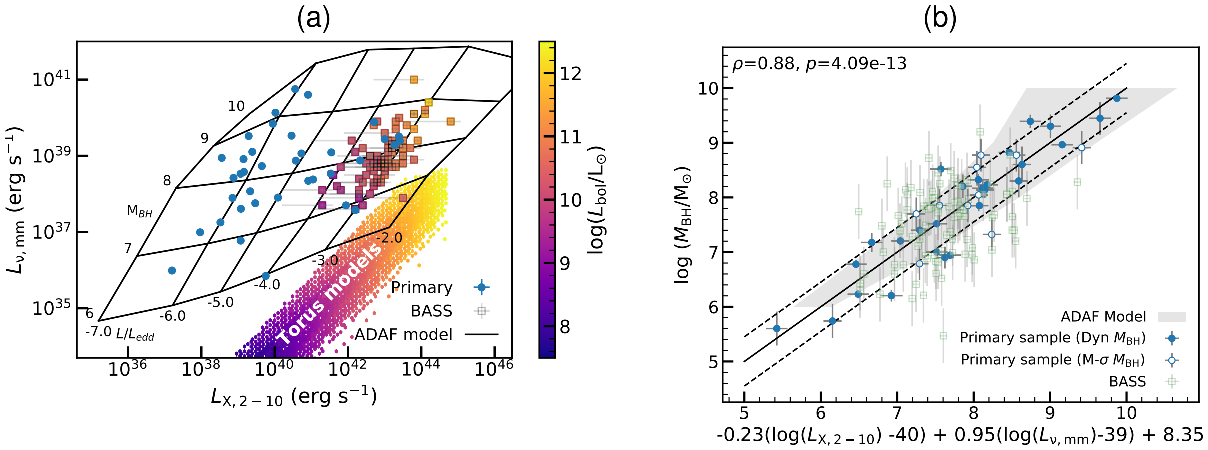

Figure 4.4: **Left**: Correlation between $L_{\mathrm{X,2\text{-}10}}$ and $L_{\nu,\mathrm{mm}}$ for the primary sample (blue circles) and the BASS (square symbols, coloured by their $L_{\,\mathrm{bol}}$) sources. Error bars are plotted for all points but some are smaller than the symbol used. The black grid illustrates the area covered by the ADAF model solutions as a function of M_{BH} and the Eddington ratio L/L_{Edd} (Section 4.3.2). The purple–yellow coloured bins indicate the region covered by the extrapolated SKIRTOR torus models (Section 4.3.1), where each hexagonal bin is coloured by the mean $L_{\,\mathrm{bol}}$ of the sources within that bin. **Right**: As the right panel of Figure 4.2, but with the BASS galaxies overlaid as green squares and the grid of ADAF models from Figure 4.4a projected onto the plane as a grey shaded area (including a small offset for clarity; see Section 4.3.2).

parameters are fixed to the values found for M81, a prototypical AGN with compact jets (Model B in Table 3 of Lucchini et al. 2022), and generated a grid of models varying the SMBH mass ($10^6 - 10^{10}$ M$_\odot$), jet power ($10^{-5.5} - 10^{-0.5}$ L$_{\mathrm{Edd}}$) and jet inclination to the line-of-sight (2.5° – 90°). The predicted $L_{\nu,\mathrm{mm}}$ and $L_{\mathrm{X,2\text{-}10}}$ (as above) are extracted from the resulting model SEDs, and compared with the observed ones. In Fig. 4.5 the $L_{\mathrm{X,2\text{-}10}} - L_{\nu,\mathrm{mm}}$ relation is shown overlaid the resulting model grids for the extremes in jet inclination (2.5° and 90°). Jets at intermediate inclinations lie between these two extremes (but evolve quickly towards the i=90° solution once the line-of-sight is no longer aligned along the jet cone). The model grids encompass the majority of the LLAGN and some BASS sources, but they have significant curvature in the 3D M_{BH}-$L_{\mathrm{X,2\text{-}10}}$-$L_{\nu,\mathrm{mm}}$ space. The correlations in Fig. 4.2 do not seem to occur naturally within this model (as projections of the higher-order surface onto the axes). The luminosities of high-accretion-rate AGN from the primary and the BASS samples are harder to explain with these models, and would require additional X-ray emitting components. This is perhaps unsurprising, as compact jet models are substantially more complex than ADAFs (see also Section 4.4).

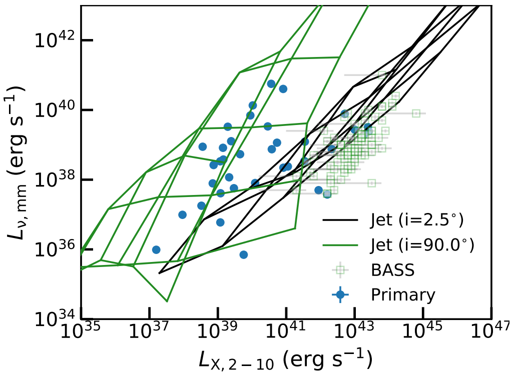

Figure 4.5: As Figure 4.4, but with slightly expanded axis ranges. In this case, the grids overlaid in black and green illustrate the areas covered by the compact jet model solutions as a function of $M_{\rm BH}$ and the jet power (Section 4.3.3), for jet inclinations of 2.5° and 90°, respectively. Solutions with intermediate inclinations lie in-between these two extremes (see Section 4.3.3).

4.3.4 DISTANCE UNCERTAINTIES

Both $M_{\rm BH}$ and luminosity measurements are systematically affected by the assumed galaxy distance D, with $M_{\rm BH} \propto D$ and $L \propto D^2$. Large distance errors can thus introduce large uncertainties on $M_{\rm BH}$ and L, and the difference in how these quantities scale with distance can give rise to spurious correlations. To test that this is not affecting these results, a simple Monte Carlo simulation is performed, drawing $M_{\rm BH}$ and the luminosities from independent Gaussian distributions that are truly uncorrelated, forcing a correlation to arise due to distance errors alone. The magnitude of the distance errors required to reproduce the Spearman rank correlation coefficients in Fig. 4.2 turned out to be $\geq$1.5 dex, much higher than that of the primary sample sources and - more in general - expected for real distance measurements. In addition, the slope of relations purely due to distance uncertainties would be substantially flatter than those observed (gradients of 0.5 for the $M_{\rm BH}$- $L_{\nu,\rm mm}$ correlation and 0.25 for the mmFP, as opposed to the observed $\approx$0.8 and $\approx$1, respectively).

To further check for any systematic distance bias, a simple quality-checking exercise is carried out for the primary sample. The analysis is restricted to only those sources with the most accurate (redshift-independent) distances (26/48), i.e. derived from surface brightness fluctuations, tip of the red giant branch methods, supernovae, Cepheids, masers, the planetary nebula luminosity function and the globular cluster luminosity function. This led me to obtain much tighter correlations, with an intrinsic scatter of 0.19 dex for the $M_{\rm BH} - L_{\nu,\rm mm}$ relation and only 0.11 dex for the mmFP. The corresponding Spearman rank coefficients are $\rho = 0.84$ ($p = 5.05 \times 10^{-7}$) and $\rho = 0.93$ ($p = 2.67 \times 10^{-9}$), respectively. It is thus concluded that the results are not biased due to distance uncertainties.

4.4 DISCUSSION AND CONCLUSIONS

I report here the finding of tight $M_{\mathrm{BH}} - L_{\nu,\mathrm{mm}}$ and $M_{\mathrm{BH}} - L_{\mathrm{X,2\text{-}10}} - L_{\nu,\mathrm{mm}}$ correlations (Fig. 4.2). The latter is dubbed the “mm fundamental plane of BH accretion" and find it to hold for both low- (mostly WISDOM) and high- (mostly BASS) luminosity AGN. To understand the physics underlying the mmFP, the observed trends are compared with models predicting the emission from different nuclear mechanisms. It is found that the results for both the primary sample and the BASS sources are best explained if their emission in the mm and X-rays primarily arises from an ADAF-like process, but cannot be explained by a classic torus model (see Fig. 4.4). This suggests that some kind of radiatively-inefficient accretion process may play a role in both low- and high-luminosity AGN, at least in the range of luminosities and accretion rates probed by the sources included in this work. While torii are known to exist in many of these AGN, some regions around their SMBHs may be radiatively-inefficient. For instance, some accretion disk solutions allow discs to transition from ADAF-like to geometrically-thin (and vice versa at different radii), and ADAFs could also exist above and below classic accretion discs (Mahadevan, 1997). Although the exact conditions under which this applies are still to be investigated, it is clear that - if confirmed - these results will have profound implications for our understanding of BH accretion in many different types of AGN.

The possibility that both the mm and X-ray emissions arise from compact (and thus probably young; O’Dea & Saikia, 2020) radio jets is also explored (Section 4.3.3). These have been argued to dominate the whole SEDs of LLAGN (e.g. Fernández-Ontiveros et al., 2023) and have spectral properties similar to those of an ADAF at the wavelengths probed here. This is also consistent with one of the most popular scenarios for the origin of the radio FP of LLAGN, suggesting that the correlation arises from strongly sub-Eddington jet-dominated emission (e.g. Falcke et al., 2004; Plotkin et al., 2012). The contribution of compact jets to the nuclear SEDs of radiatively-efficient, quasar-like AGN is instead still hotly debated (e.g. Fawcett et al., 2020; Girdhar et al., 2022). These results are marginally consistent with these scenarios, as it is found that compact jet models can explain the correlations for most of the LLAGN, but additional X-ray emitting components are required in the higher-luminosity systems.

In short, it has been demonstrated that ADAF-like models convincingly predict the mmFP. Compact jets are also a plausible explanation (at least for LLAGN), but the corresponding models do not reproduce the correlation as naturally as the ADAF-like ones. It should be cautioned, however, that the plasma physics underlying both the ADAF and compact jet models is not well constrained, and significant uncertainties are present in all the model parameters and how they interact. It is thus concluded that, while “classic” torus models seem to be ruled out, either ADAF-like or compact jet emission have the potential to explain the observed trend. The presence of one (or more) of these mechanisms could even help explaining the increased far-infrared/sub-mm contribution attributed to AGN in some empirical SED models (e.g. Symeonidis, 2022). The tight $L_{\rm X,2\text{-}10}$-$L_{\nu,\rm mm}$ correlation observed in Fig. 4.4a for the BASS sources is also consistent with the one reported by Ricci et al. (2023) between the 100 GHz and 14-150 keV luminosities (see also Behar et al., 2018), and these results add interesting clues onto its origin. Determining with certainty the relevant mechanism(s) giving rise to the observed correlations is beyond the scope of this work, but is crucial to further our understanding of the SMBH accretion/ejection processes in different AGN types.

Beyond carrying information on the nuclear physics, the correlations presented here provide new rapid methods to indirectly estimate the mass of SMBHs (or their accretion rates, if one has alternative, robust estimates of $M_{\rm BH}$ and $L_{\nu,\rm mm}$; see e.g. Ricci et al., 2023). Although direct $M_{\rm BH}$ estimates can be obtained using a variety of techniques (e.g. stellar or gas kinematics, reverberation mapping), these typically require very time-consuming observational campaigns and currently have limited application beyond the local Universe. The ability to use nuclear mm and (optionally) X-ray luminosities allows $M_{\rm BH}$ estimates when dynamical measurements are not possible and/or the standard scaling relations are unusable (such as in dwarf or disturbed galaxies). It also allows $M_{\rm BH}$ predictions over a wider range of redshifts. At the high-mass end of the correlations, ALMA can allow us to constrain $M_{\rm BH}$ up to $z \approx 0.3$ (and is limited more by angular resolution and frequency coverage than sensitivity). Proposed new interferometers (such as the next-generation Very Large Array, ngVLA) should be able to push this to $z = 1$ and beyond. Large X-ray surveys that can provide complementary X-ray data are also ongoing (e.g. eROSITA), and next-generation satellites (such as the Advanced Telescope for High ENergy Astrophysics, *Athena*) will extend these to higher-z. It should be noted that the intrinsic scatter of the $M_{\rm BH} - L_{\nu,\rm mm}$ relation is comparable to that of the $M_{\rm BH} - \sigma_\star$ relation (e.g. van den Bosch, 2016), and $\sigma_{\rm int}$ of the mmFP in Fig. 4.2 is comparable or even lower than that of its radio counterpart (depending on the sample used to fit the plane; see e.g. Merloni et al., 2003; Falcke et al., 2004; Plotkin et al., 2012; Gültekin et al., 2019). When restricting this analysis to only those primary sample sources with the most accurate (redshift-independent) distances, a much tighter correlation is obtained (see Section 4.3.4), with $\sigma_{\rm int}$ comparable to that of the tightest scaling relations in Astronomy (such as the Baryonic Tully-Fisher relation; e.g. Lelli et al., 2016, 2019). This technique - if sufficiently verified - is thus well suited to constrain the details of SMBH-host galaxy co-evolution in regimes that have been difficult to access up to now (Williams et al., 2023).

CHAPTER 5

Extending the mm fundamental plane

“A circle is like a square."

-Helena Faustino Vieira

5.1 INTRODUCTION

In chapter 4 I presented the newly discovered mm fundamental plane (Ruffa et al., 2024). The intrinsic scatter of this plane (≈ 0.4 dex) is comparable to that of the $M_{\rm BH}-\sigma_\star$ relation (e.g. van den Bosch, 2016), and can be even lower than that of its radio counterpart (depending on the sample used to fit the plane; see e.g. Merloni et al., 2003; Falcke et al., 2004; Gültekin et al., 2009; Plotkin et al., 2012; Gültekin et al., 2019). When restricting the analysis to only those primary sample sources with the most accurate (redshift-independent) distances, a even tighter correlation is obtained, with an intrinsic scatter comparable to that of some of the tightest scaling relations in Astronomy (such as the Baryonic Tully-Fisher relation; e.g. Lelli et al., 2016, 2019). Surprisingly, the observed correlation is found to hold for both low-luminosity AGN (LLAGN) and sources from the *Swift*-BAT AGN Spectroscopic Survey (BASS), comprising some of the brightest and most powerful nearby AGN (with median $L_{\rm bol}\approx 10^{44}$ erg s^{-1} and $\dot{M}\approx 0.01-0.1\ \dot{M}_{\rm Edd}$; Koss et al., 2017), hinting at a greater AGN homogeneity than previously thought.

Models of advection-dominated accretion flows (ADAFs) or compact radio jets seem to be able to explain this observed relationship, while classical torus models can not. This new mm fundamental plane thus provides both a proxy (i.e. indirect estimate) of SMBH mass and crucial new insights into SMBH accretion physics. Whether stellar-mass BHs

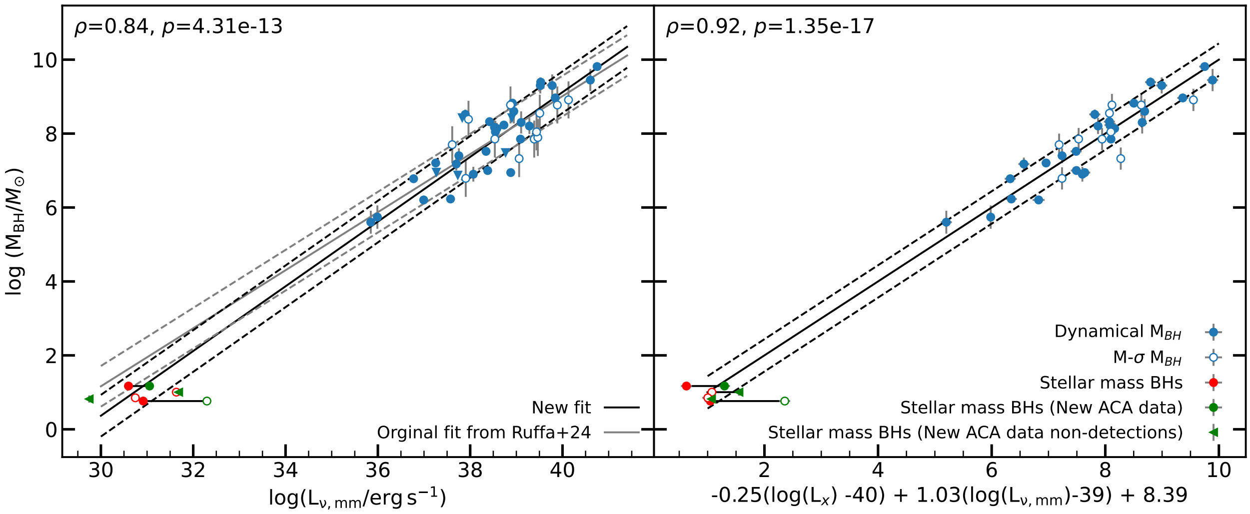

Figure 5.1: Correlation between $M_{\rm BH}$ and $L_{\nu,\rm mm}$ (left panel) and edge-on view of the $M_{\rm BH}$-$L_{\rm X,2\text{-}10}$-$L_{\nu,\rm mm}$ correlation (right panel) as from Chapter 4. The four quasi-persistent hard state stellar mass black holes with available archival data are included as red points. Archival data for the four quasi-persistent hard state stellar mass black holes is shown as red points, while new ACA and Swift data are included as green points. A black line connects the original archival data points and the updated data points where applicable. In both panels, filled blue circles are for SMBHs with dynamical $M_{\rm BH}$ measurements, open circles for those with $M_{\rm BH}$ from the $M_{\rm BH} - \sigma_\star$ relation of van den Bosch (2016). Error bars are plotted for all points but some are smaller than the symbol used. The best-fitting power-laws are overlaid as a black solid lines, the observed scatter as black dashed lines. The grey solid is the original best fitting power-law with the scatter of this original fit being the dashed grey line. The correlation coefficients ρ and p-values of the performed Spearman rank analysis are reported in the top-left corner of each panel.

in accreting systems (i.e. X-ray binaries, XRBs) also follow the mm plane (as they do the radio plane), which would hint at an even greater universality of accretion mechanisms, is however as yet unclear.

In this chapter I present an analysis of the mm fundamental plane for stellar mass black holes, by using available data of all known quasi-persistent, hard-state transients (i.e. LLAGN equivalent; 5 XRBs). The main aim is to establish whether this newly-discovered plane holds also for accreting stellar mass black holes and - if yes - whether ADAF models also explain the correlation for these type of sources, as they seem to do for AGN of all accretion rates.

5.2 THE MM FUNDAMENTAL PLANE FOR STELLAR MASS BLACK HOLES

Only a few tens of XRBs have confirmed stellar mass black holes. Most of these are truly transients, with a range of $\geq 10^8$ in X-ray luminosity from quiescence to outburst. Very few among the confirmed accreting stellar systems are quasi-persistent sources, varying by only a factor of ~ 10 over decades of study. Strikingly, such transient and persistent sources follow the same XRB radio – X-ray correlation, that becomes the radio fundamental plane with the addition of a mass term. Crucially, and unlike SMBHs, an individual XRB can be tracked as it moves back and forth along the plane, demonstrating the plane to be both an intrinsic and global effect. These correlations are exhibited during the so-called “hard state”, when a strong (accretion disk) coronal X-ray emitting component causes the correlation with the radio jet. Accreting stellar-mass black holes in this phase are considered scaled-down equivalents of LLAGN. At high luminosities, XRBs (and likely also AGN) may enter a “soft” accretion state, when the jet is suppressed and sources lie well below the correlation (i.e. at lower luminosities; see Fender et al., 2004 for a summary of these behaviours). I also note that the range of BH masses for the sample of known XRBs is very small, with a mean of ≈ 7 M$_\odot$ and a standard deviation of ≈ 3 M$_\odot$.

5.2.1 NEW ACA OBSERVATIONS

Currently, there are five known quasi-persistent transients that are always in the hard state. These are Cygnus X-1, GRS 1915+105, GX 339-4, XTEJ1118+480 and A0620-00. Using the Atacama Compact Array (ACA) new observations were acquired for four of the five hard state XRBs (Cygnus X-1, GRS1016+105, GX 339-4 and A0620-00; Project Code: 2023.1.00887). These objects were observed at 230 GHz (∼1mm) to match the previous continuum observations of the primary sample that defined the mmFP. The ACA was chosen as XRBs do not have extended emission and so the angular resolution of the observations is irrelevant. The data was reduced using the Common Astronomy Software Applications (CASA) pipeline (McMullin et al., 2007), adopting a version appropriate for each dataset and a standard calibration strategy. The data was reduced in same way as the AGN galaxy sample with the full details on the data reduction being found in Davis et al. (2022).

The continuum images were produced by combining the continuum spectral windows (SPWs) using the CASA task TCLEAN in multi-frequency synthesis (MFS) mode. The continuum images had noise levels ranging from 0.42–0.60 $\mathrm{mJy\,beam^{-1}}$. The new ACA luminosites are listed in Table 5.1.

I additionally gather X-ray observations of these sources from the *Swift*[*] catalogue. I chose *Swift* observations that were taken as close to the ACA observations as possible to reduce the impact of variability. These observations are taken in the 0.3-10 keV band so I scale these luminosities to the 2-10 keV band using a spectral index of -0.8 (the mean value reported by Reeves & Turner (2000). For GX 339-4 there was observation by *Swift* three days after the ACA observation. For Cygnus X-1 the nearest *Swift* observation was just over a month before the ACA observation. For GRS 1915+105 the nearest *Swift* observation was just over 9 months before the ACA observations. For A0620-00 the nearest *Swift* observation was in 2010 meaning that the impact of variability could be important in this source.

5.2.2 ARCHIVAL OBSERVATIONS

In order to study how flux variability affects their position on the mmFP I additionally gather the archival mm and X-ray luminosities for four of the five persistent transients from a variety of telescopes. I estimated the mm luminosity of Cygnus X-1, GRS 1915+105 and GX 339-4 from archival ALMA continuum observations at 230 GHz (for Cygnus X-1 and GX 339-4) and 104 GHz (for GRS 1915+105; from programs #2016.1.00496.S, #2019.1.01324.T and #2017.1.00051.S, respectively), following the same procedure described in Chapter 4. The mm luminosity of XTEJ1118+480 was estimated from JCMT continuum observations at 350 GHz presented in Fender et al. (2001).

Where these observations were not taken at 230 GHz I was forced to scale the fluxes to this band assuming a flat spectral index ($\alpha = 0$). This unavoidably introduces additional uncertainties in the comparison. I primarily use the new homogeneous observations of these sources (presented in Section 5.2.1) when performing the fits presented in this work.

I gathered X-ray observations from *Swift* that best matches the date of the archival mm observations. XTEJ1118+480 did not have Swift X-ray observations so its $2-10$ keV X-ray flux was instead taken from Gültekin et al. (2019). The properties of these four objects used are presented in Table 5.1.

---

[*] `https://www.swift.ac.uk/`

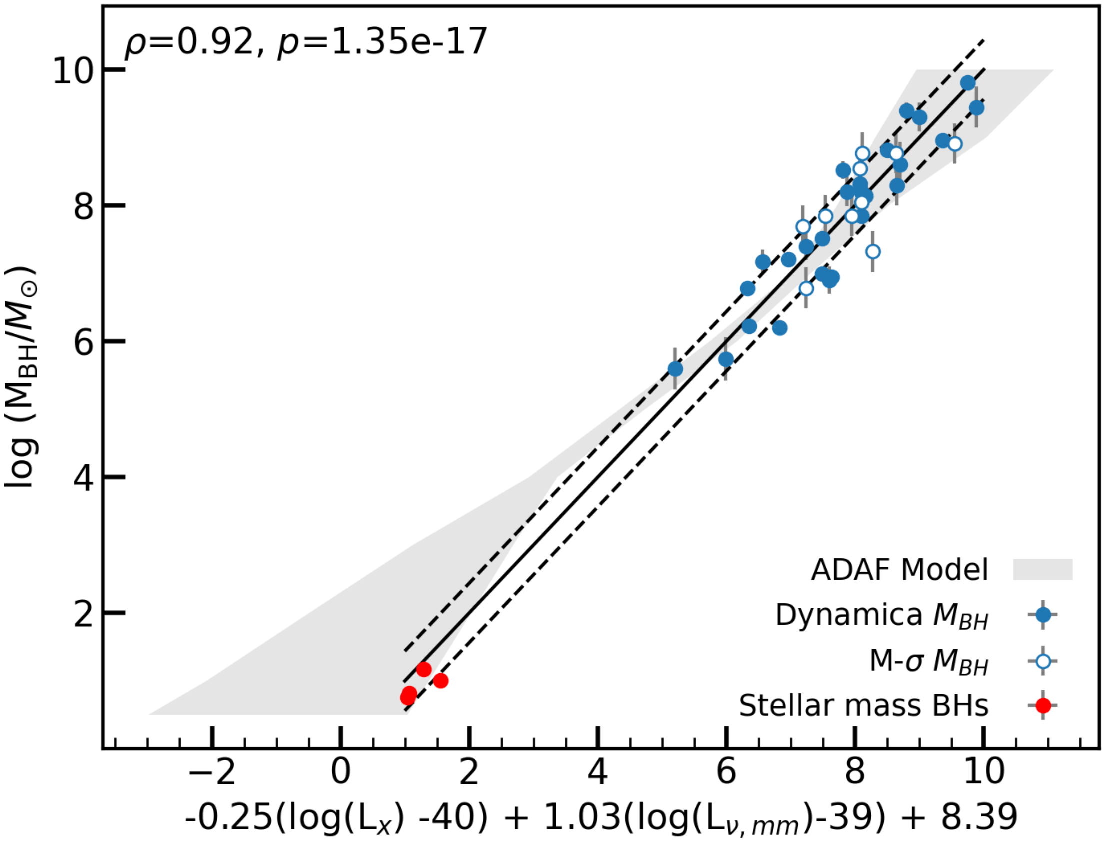

Figure 5.2: Same as the right panel of Figure 5.1 with the grey shaded region representing the ADAF model.

Table 5.1: Stellar mass black hole properties

Object (1)	Distance (kpc) (2)	$\log M_{\rm BH}$ ($\rm M_\odot$) (3)	$\log L_{\nu,\rm mm}$ ($\rm erg\,s^{-1}$) (4)	$\nu_{\rm mm,obs}$ (GHz) (5)	mm Observation date (6)	$\log L_{\rm X,\ 2\text{-}10}$ ($\rm erg\,s^{-1}$) (7)	X-ray Observation date (8)
Cygnus X-1 (ACA)	1.86	1.17	31.1 ± 0.04	230	11-05-2024	35.6 ± 0.08	08-04-2024
Cygnus X-1 (Archival)			30.6 ± 0.04	230	06-11-2016	36.4 ± 0.08	23-11-2016
GRS 1915+105 (ACA)	11	1.00	< 31.7	230	26-05-2024	37.2 ± 0.08	16-08-2023
GRS 1915+105 (Archival)			31.6 ± 0.04	104	13-10-2017	38.9 ± 0.08	18-10-2017
GX 339-4 (ACA)	10	0.76	32.3 ± 0.04	230	13-06-2024	36.5 ± 0.08	16-06-2024
GX 339-4 (Archival)			30.9 ± 0.04	230	13-10-2017	36.0 ± 0.08	18-10-2017
XTEJ1118+480 (Archival)	1.8	0.85	30.7 ± 0.04	350	30-05-2000	35.5 ± 0.08	29-03-2000
A0620-00 (ACA)	10	6.6	< 29.7	230	5-12-2023	31.1 ± 0.08	25-03-2010

Notes: (1) object name and whether is is new ACA or archival data with its distance in (2). (3) black hole mass. (4) mm luminosity with the observed frequency in (5). (6) mm observation data (7) 2-10 keV X-ray luminosity with the observation date in (8). The distance and black hole masses of these sources were taken from Gültekin et al. (2019), apart from for GX 339-4, where they were taken from Tremou et al. (2020).

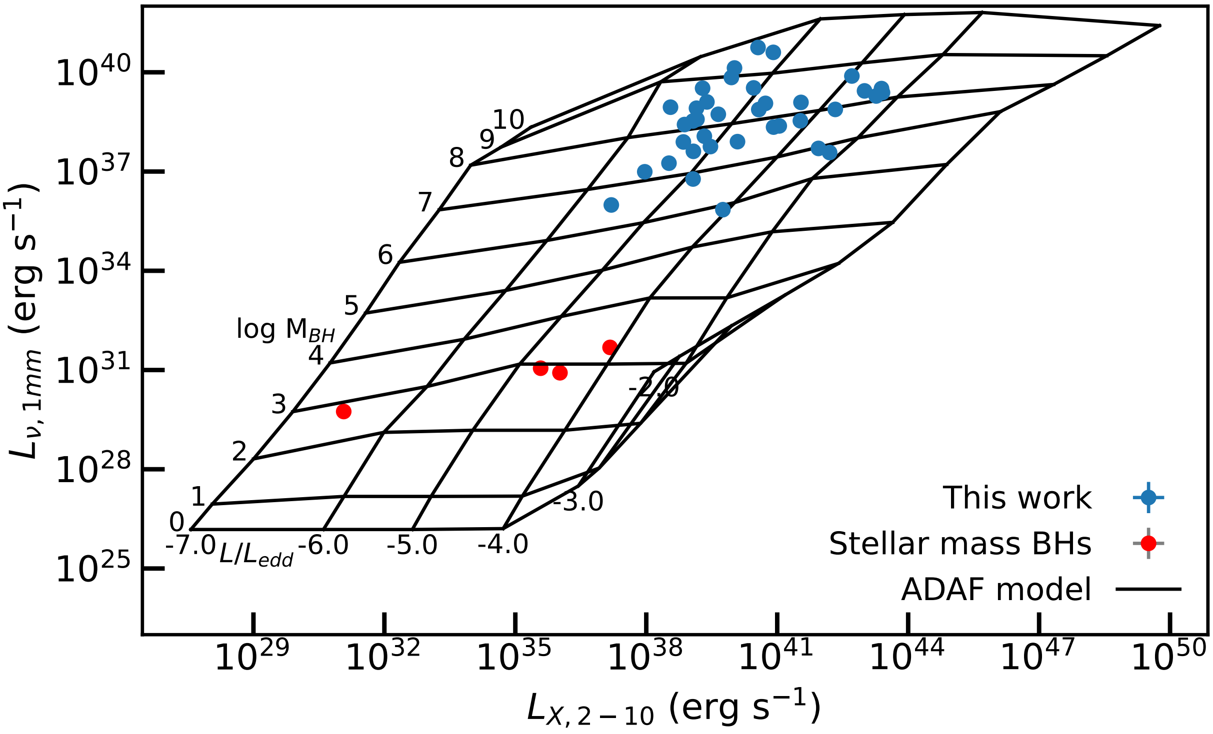

Figure 5.3: Correlation between $L_{\nu,\mathrm{mm}}$ and $L_{\mathrm{X,2\text{-}10}}$. The black grid represents the ADAF model as a function of M_{BH} and Eddington ratio.

5.3 RESULTS

In Figure 5.1 I show the four transients with ACA data as green points on the $M_{\mathrm{BH}} - L_{\nu,\mathrm{mm}}$ and the mmFP correlations. One object, GX339-4, has greatly increased its mm luminosity which moves it away from the mmFP. The point is shown as an unfilled circle in Figure 5.1. The cause of this change in GX339-4 will be discussed further in Section 5.4. I also include the four transients with archival data as red points on the mmFP. The two sources (GRS 1915+105 and XTEJ1118+480) which do not have archival 230 GHz observations are shown as unfilled circles. I re-run the same LTS_PLANEFIT (Cappellari et al., 2013b) fitting algorithm as in Chapter 4 and find that these sources lie in the same plane. When including the XRBs I obtain plane coefficients that agree well with those found when fitting SMBHs alone. The resulting best-fitting power law is:

$$\log_{10}\left(\frac{M_{\mathrm{BH}}}{M_{\odot}}\right) = (0.88 \pm 0.03)\left[\log_{10}\left(\frac{L_{\nu,\mathrm{mm}}}{\mathrm{erg\,s^{-1}}}\right) - 39\right] + (7.8 \pm 0.08)\,, \tag{5.1}$$

and the best-fitting plane in the $(\log M_{\mathrm{BH}},\, \log L_{\mathrm{X,2\text{-}10}},\, \log L_{\nu,\mathrm{mm}})$ space:

$$\begin{aligned}\log_{10}\left(\frac{M_{\mathrm{BH}}}{M_{\odot}}\right) &= (-0.25 \pm 0.05)\left[\log_{10}\left(\frac{L_{\mathrm{X,2\text{-}10}}}{\mathrm{erg\,s^{-1}}}\right) - 40\right] \\ &+ (1.03 \pm 0.05)\left[\log_{10}\left(\frac{L_{\nu,\mathrm{mm}}}{\mathrm{erg\,s^{-1}}}\right) - 39\right] + (8.39 \pm 0.08)\,,\end{aligned} \tag{5.2}$$

When performing this fit and the following analysis I only use the ACA observations except for GX339-4 where I instead use the archival data as this source appears to have changed.

5.3.1 PHYSICAL DRIVERS

As shown in Figure 5.1, the four persistent XRBs included in this analysis are in good agreement with the M_{BH} – $L_{\nu,\mathrm{mm}}$ correlation and the mm fundamental plane of BH accretion defined by active galaxies, extending both by ≈ 5 orders of magnitude. This suggests that the dominant mechanism giving rise to the nuclear mm continuum (and its correlation with that producing the 2 – 10 keV emission) may be similar to the one in LLAGN. To determine if the underlying mechanisms considered to be potentially powering the galaxy-scale correlation can apply here too, I compared the observed nuclear mm and X-ray luminosities of the four XRBs included in my analysis to those extracted from mock SEDs

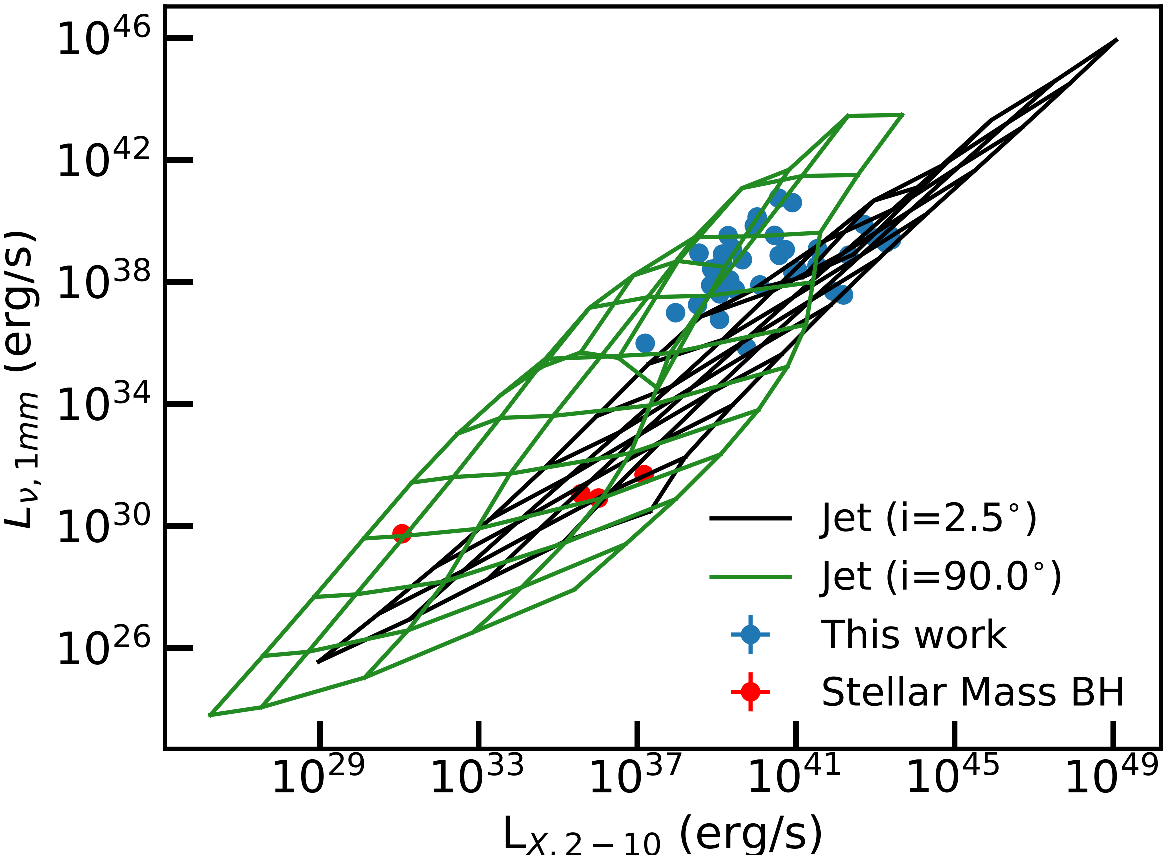

Figure 5.4: Same as Figure 5.3 however the black and the green grids represent jet models with 2.5° and 90° inclination respectively.

arising from radiatively-inefficient (ADAF-like) and from compact radio jets. As there is no evidence for a torus in XRBs I do not consider such a model here.

ADAF model

To test whether ADAFs can explain existence of a millimetre fundamental plane down to these low masses I built model SEDs using the LLAGN model of Pesce et al. (2021). In typical LLAGN and some (low-accretion-rate) Seyferts, the classic accretion disk is either absent or truncated at some inner radius, usually beyond a few tens of Schwarzschild radii, and is replaced by a geometrically-thick two-temperature structure in which the ion temperature is greater then the electron temperature and the accretion rate occurs at rates well below the Eddington limit (i.e $<<\ 0.01\,\dot{M}_{\rm Edd}$; Narayan & Yi, 1995a; Ho et al., 2008).

The electrons in these radiatively-inefficient flows cool down via a combination of self-absorbed synchrotron, Bremsstrahlung and inverse Compton radiation, which together gives rise to the nuclear emission from the mm to the X-rays.

ADAFs have been predicted to be present in XRBs (Esin et al., 1997) which could explain why I am seeing stellar mass black holes also following the mmFP. In Figure 5.2 I extend the ADAF model used in Chapter 4 and extend it to stellar mass black hole regime. I find that the ADAF model can be extended down to the stellar mass regime and reasonably well predicts the position of these sources on the relation. This could suggest that ADAFs are the physical mechanisms behind the fundamental plane across the entire mass regime. However, as can be seen in Figure 5.3 the ADAF model does predict that the stellar mass BH would have masses of $\sim 10^3\,M_{\odot}$ which is around 2 orders of magnitude higher then their true BH masses. These models contain many free parameters describing e.g. the unknown plasma physics within ADAFs. Here I have left all of these fixed to their default values as in Pesce et al. (2021), which were calibrated for massive SMBH. As such although this discrepancy is concerning, if the emission truly arises from an ADAF these observations could potentially be used to help tune those unknown parameters.

Compact jet model

Unlike extended jets, where the synchrotron emission is optically-thin, compact radio jets have self-absorbed synchrotron spectra (similar to those from ADAFs) and have been argued to dominate the nuclear SEDs of LLAGN. In some cases they are preferred over a pure ADAF solution, as this would be overly luminous at near-infrared and optical wavelengths (e.g Fernández-Ontiveros et al., 2023). To determine if compact jets can explain the observed trends, I used the `BHJET` model of Lucchini et al. (2022).

If a compact radio jet was the physical driver behind the fundamental plane this could potentially explain why stellar mass black holes also appear to follow the fundamental plane as XRBs are expected to have jets (Fender et al., 2004). To test whether radio jets are the physical driver behind the emission in XRBs I extend the jet models used in Chapter 4 to the stellar mass regime. As was the case in Chapter 4 I find the emission from stellar mass black holes may be explained by compact radio jets. However, the edge on radio jets $(i = 90^{\circ})$ overpredicts the $M_{\rm BH}$ for the stellar mass black holes with predicted masses of $\sim 10^2 - 10^3\,M_{\odot}$ whilst the face on jets $(i = 2.5^{\circ})$ predict more realistic $M_{\rm BH}$ of $\sim 10^1\,M_{\odot}$. Again these models have many free parameters, and so I do not draw strong conclusions from these mismatches. Clearly future work will be required to help constrain these free parameters and if these mismatches can be resolved.

5.4 DISCUSSION AND CONCLUSIONS

In chapter 4 I reported the presence of a tight $M_{\rm BH} - L_{\rm X,2\text{-}10} - L_{\nu,\rm mm}$ relationship, dubbed the "mm fundamental plane of BH accretion", that holds for both high and low luminosity AGN. In that work I investigated three potential physical drivers behind the newly discovered fundamental plane. In the standard paradigm this correlation should be driven by the torus surrounding the AGN (at least for the higher accretion rates sources). In lower accretion rate sources radiatively-inefficient ADAF-like processes could be driving this correlation. In some accretion disc solutions discs can transform to and from ADAF-like and geometrically-thin structures, with ADAFs potentially existing above and below the classic accretion discs (Mahadevan, 1997). Finally, this correlation could be driven by compact and probably young (O'Dea & Saikia, 2020) radio jets. These may dominate the whole SEDs of LLAGN (e.g. Fernández-Ontiveros et al., 2023) and have spectral properties of ADAF at the same wavelength. This is also consistent with origin scenarios of the radio FP of LLAGN, suggesting that the correlation arises from strongly sub-Eddington jet-dominated emission (e.g. Falcke et al., 2004; Plotkin et al., 2012). However, the contribution to the nuclear SEDs of radiatively-efficient, quasar-like AGN is still hotly debated (e.g. Fawcett et al., 2020; Girdhar et al., 2022)

In Chapter 4 it was found that ADAFs seem to be the best fit to the mm fundamental plane with the torus model under predicting the $L_{\nu,\rm mm}$ and the compact jet model being only marginally consistent.

In this chapter I aimed to see if stellar mass BH in XRBs also follow the mm fundamental plane, as they do the radio fundamental plane. In Figure 5.1 I have found that the stellar mass BHs in XRBs do fall on the mmFP, using new ACA and archival observations. This could suggest that the same physical processes are important, not only in high and low accretion rate SMBH systems but also in lower mass objects. One source, GX339-4, has increased greatly in its mm luminosity which takes it away from the mm fundamental plane. I speculate that this source may have shifted to a soft accretion state and so falls below the mm fundamental plane, as is also seen when XRBs change state and no longer follow the radio fundamental plane. This should be investigated further. I note that not having simultaneous X-ray observations of all these sources may be driving further scatter.

I extended the ADAF and compact radio jet models used in Chapter 4 down to the stellar mass regime. I find that the ADAF and compact jets models can potentially explain the emission from stellar mass black holes. However, the ADAF model and the edge on jet model overpredict the $M_{\rm BH}$ for the millimetre luminosities of these stellar mass BH by around 2 orders of magnitude.

It is clear that further observational work needs to be done to fully constrain where stellar mass black holes fall on the mm fundamental plane, and how variability affects this. Further theoretical work is also critical to fully understand what mechanism is driving this relation. Such work will be highly valuable, shedding light on the physics of accretion across mass scales, and revealing the common processes that apply both within our galaxy and for extragalactic systems.

CHAPTER 6

Conclusion

“It’s a good skulking hole."

-Michael Norman

6.1 THESIS OVERVIEW

Active galactic nuclei are incredibly important in the evolution of a galaxy and may play a key role in quenching the star formation of galaxies. Our understanding of AGN and their role in galaxy evolution is growing but more work needs to be done to fully understand the physical structure and processes taken place in AGN to fully understand the connection between AGN and their host galaxy.

This thesis combines high resolution observations of the gas in nearby galaxies with multi-wavelength data from the AGN that are being hosted to probe the interplay between AGN and their host galaxies. This thesis studies how AGN can impact the gas reservoir around them whilst also studying how host galaxy can fuel the activity from the AGN.

6.2 KEY RESULTS

6.2.1 CIRCUMNUCLEAR AGN FUELLING

In this chapter (Chapter 2) I utilise the WISDOM sample of nearby galaxies to search for correlations between the circumnuclear gas reservoir and the activity from the AGN that are being hosted to better understand the AGN fuelling/feedback picture. I searched for correlations between the cold molecular gas masses on the circumnuclear regions of a sample of 35 nearby galaxies and AGN activity tracers at radio, X-ray, optical and sub-mm wavelengths. I found that the molecular gas masses of my sample sources, measured within a range of elliptical apertures with radii from 50 to 100 pc, do not correlate with any of the adopted tracers.

The sample analysed in this study includes galaxies with a range of nuclear activities and global properties, and I was not able to reproduce any of the results found for other AGN-specific sub-samples. This suggests the level of nuclear activity in a given galaxy cannot purely be due the amount of cold gas fuel reservoir around the central SMBH. The fuelling mechanism of active galaxies is not ubiquitous and may vary between AGN types, and timescale variations are likely very important.

I also probed the molecular concentration of the circumnuclear gas discs in my sample of galaxies to assess whether they had been impacted by AGN feedback. There is no evidence of a relation between structure on circumnuclear scales and current accretion rate, in contrast to results found for some nearby Seyfert galaxies selected to be in an active phase and despite my objects spanning the same range in circumnuclear properties. This could indicate that these galaxies were previously in a more active phase that impacted the circumnuclear gas, or that these molecular concentrations arise naturally within circumnuclear gas discs and are not related to AGN processes.

Further observations and theoretical studies are clearly needed to make further progress to determine the link between circumnuclear gas reservoirs and nuclear activity. For instance, dense gas may be better linked to the direct reservoirs for accretion, and expanded sample sizes may help to overcome timescale issues.

6.2.2 A COMPARISON BETWEEN AGN DIAGNOSTIC DIAGRAMS

In this chapter (Chapter 3) I compare the AGN classification mechanisms at optical and sub-millimetre wavelengths to better understand the AGN excitation mechanism and to investigate where AGN can excite both low and high density gas. Using CARS ALMA data I have observed dense and molecular gas tracers in 5 nearby type 1 (unobscured) AGN. I have found that the large scale molecular discs of these systems show a variety of different morphologies, with bars being important in several cases. The denser gas is only detected towards the nuclei, close to the AGN where the gas density is highest. I have used the observations of the dense gas tracers to study their use as an AGN diagnostic tool. It has been reported in previous studies that the HCN/HCO+ and HCN/CS ratios can be used to separate AGN from star forming galaxies using a *sub-mm HCN diagram*, as HCN can be enriched by chemical pathways at high temperatures. I find that all three of the sources where the dense gas tracers where detected follow known relations between the amount of dense gas and star-formation. This indicates that if the HCN abundance has been enriched it has not been enhanced enough to effect global scaling relation. When studying the *sub-mm HCN diagram* I am limited by the lack of detection of CS(7-6) in many of my sources, but in those that I could study I find general agreement between optical and sub-mm classification gas excitation mechanisms. This suggests that that AGN can contribute to the excitation of both the low density gas in the WIM and high density molecular gas clouds simultaneously, perhaps through X-ray, cosmic ray or shock heating mechanisms.

Further observations of dense gas around AGN are clearly needed to further populate the sub-mm HCN diagram and to allow further cross-comparisons with other AGN classification schemes and studies of AGN excitation at different wavelengths.

6.2.3 FUNDAMENTAL PLANE OF BLACK HOLE ACCRETION

In this chapter (Chapter 4 and Ruffa et al., 2024) I present the mm fundamental plane (mmFP) which is a correlation between the AGN X-ray and mm luminosities and the SMBH mass. It has been demonstrated that ADAF-like models convincingly predict the mmFP. Compact jets are also a plausible explanation (at least for LLAGN), but the corresponding models do not reproduce the correlation as naturally as the ADAF-like ones. It should be cautioned, however, that the plasma physics underlying both the ADAF and compact jet models is not well constrained, and significant uncertainties are present in all the model parameters and how they interact. It is concluded that, while “classic” torus models seem to be ruled out, either ADAF-like or compact jet emission have the potential to explain the observed trend. The presence of one (or more) of these mechanisms could even help explaining the increased far-infrared/sub-mm contribution attributed to AGN in some empirical SED models (e.g. Symeonidis, 2022). The tight $L_{\rm X,2\text{-}10}$-$L_{\nu,\rm mm}$ correlation observed in Fig. 4.4a for the BASS sources is also consistent with the one reported by Ricci et al. (2023) between the 100 GHz and 14-150 keV luminosities (see also Behar et al., 2018), and these results add interesting clues onto its origin. Determining with certainty the relevant mechanism(s) giving rise to the observed correlations is beyond the scope of this work, but is crucial to further our understanding of the SMBH accretion/ejection processes in different AGN types.

Beyond carrying information on the nuclear physics, the correlations presented here provide new rapid methods to indirectly estimate the mass of SMBHs (or their accretion rates, if one has alternative, robust estimates of $M_{\rm BH}$ and $L_{\nu,\rm mm}$; see e.g. Ricci et al., 2023). Although direct $M_{\rm BH}$ estimates can be obtained using a variety of techniques (e.g. stellar or gas kinematics, reverberation mapping), these typically require very time-consuming observational campaigns and currently have limited application beyond the local Universe. The ability to use nuclear mm and (optionally) X-ray luminosities allows $M_{\rm BH}$ estimates when dynamical measurements are not possible and/or the standard scaling relations are unusable (such as in dwarf or disturbed galaxies). It also allows $M_{\rm BH}$ predictions over a wider range of redshifts. At the high-mass end of the correlations, ALMA can be used to constrain $M_{\rm BH}$ up to $z \approx 0.3$ (and is limited more by angular resolution and frequency coverage than sensitivity). Proposed new interferometers (such as the next-generation Very Large Array, ngVLA) should be able to push this to $z = 1$ and beyond. Large X-ray surveys that can provide complementary X-ray data are also ongoing (e.g. eROSITA), and next-generation satellites (such as the Advanced Telescope for High ENergy Astrophysics, *Athena*) will extend these to higher-z. It should also be noted that the intrinsic scatter of the $M_{\rm BH} - L_{\nu,\rm mm}$ relation is comparable to that of the $M_{\rm BH} - \sigma_\star$ relation (e.g. van den Bosch, 2016), and $\sigma_{\rm int}$ of the mmFP in Fig. 4.2 is comparable or even lower than that of its radio counterpart (depending on the sample used to fit the plane; see e.g. Merloni et al., 2003; Falcke et al., 2004; Plotkin et al., 2012; Gültekin et al., 2019). When restricting this analysis to only those primary sample sources with the most accurate (redshift-independent) distances, a much tighter correlations is obtained (see Section 4.3.4), with $\sigma_{\rm int}$ comparable to that of the tightest scaling relations in Astronomy (such as the Baryonic Tully-Fisher relation; e.g. Lelli et al., 2016, 2019). This technique - if sufficiently verified - is thus well suited to constrain the details of SMBH-host galaxy co-evolution in regimes that have been difficult to access up to now (Williams et al., 2023).

6.2.4 EXTENDING THE MM FUNDAMENTAL PLANE

In this chapter (Chapter 5) I aimed to see if stellar mass BH in XRBs also follow the mm fundamental plane (see Chapter 4), as they do the radio fundamental plane. In Figure 5.1 I have found that the stellar mass BHs in XRBs do fall on the mmFP, using new ACA and archival observations. This could suggest that the same physical processes are important, not only in high and low accretion rate SMBH systems but also in lower mass objects. One source, GX339-4, has increased greatly in its mm luminosity which takes it away from the mm fundamental plane. I speculate that this source may have shifted to a soft accretion state and so falls below the mm fundamental plane, as is also seen when XRBs change state and no longer follow the radio fundamental plane. This should be investigated further. I note that not having simultaneous X-ray observations of all these sources may be driving further scatter.

I extended the ADAF and compact radio jet models used in Chapter 4 down to the stellar mass regime. I find that the ADAF and compact jets models can potentially explain the emission from stellar mass black holes. However, the ADAF model and the edge on jet model overpredict the M_{BH} for the millimetre luminosities of these stellar mass BH by around 2 orders of magnitude.

It is clear that further observational work needs to be done to fully constrain where stellar mass black holes fall on the mm fundamental plane, and how variability affects this. Further theoretical work is also critical to fully understand what mechanism is driving this relation. Such work will be highly valuable, shedding light on the physics of accretion across mass scales, and revealing the common processes that apply both within our galaxy and for extragalactic systems.

6.3 FUTURE WORK

In chapter 2 I used high resolution ALMA data to study whether the AGN in this sample of galaxies are being fuelled by the circumnuclear gas that is surrounding the AGN. I found a lack of correlations between the gas in the circumnuclear region and the activity from the AGN which may suggest that AGN fuelling is not a ubiquitous process. To better understand the fuelling process in these source I could use the high resolution ALMA data and codes such as KINMS (Davis et al., 2013) to search for the non-radial motion of inflowing gas in these galaxies and try to connect these inflows to the activity from the AGN. I could also investigate whether the AGN activity correlates with the amount of dense gas surrounding it as previous authors have found a correlation between the circumnuclear dense gas mass and activity from the AGN. Finally, performing this study with an expanded sample containing many different types of AGN would help to understand the AGN fuelling mechanism accross the population.

In chapter 4 I present the newly discovered *mm fundamental plane of black hole accretion*. This relation was discovered using the 1mm nuclear continuum luminosity, the 2-10 keV X-ray luminosity and the SMBH mass. It was then found that either advection dominated accretion flows (ADAFs) or compact jets could be physical driving mechanism behind this relation. To fully understand the underlying accretion mechanism in these sources and the physical driver behind this mm fundamental plane further multi-wavelength data is needed. Searching for parallel fundamental planes at other wavelengths (i.e. infrared) may give important insights into the underlying accretion mechanisms and by gathering more high resolution data at radio wavelengths may allow for connections with the existing radio fundamental plane.

In chapter 5 I extended the mm fundamental plane to the stellar mass black hole regime and in general accreting stellar mass black holes in X-ray binaries (XRBs) also follow the mm fundamental plane. It is now important to test the limits of the mm fundamental plane. Future work would include placing quasars onto the mm fundamental plane so see if they also follow the relation. Quasars are the most luminous class of AGN with the highest accretion rates so if it is found they also follow the mm fundamental plane would have a profound impact on our understanding of the underlying accretion process in AGN. It is also important to expand the sample of galaxies used to define the mm fundamental plane to include galaxies that are gas poor or do not have a regularly rotating CO disk. The sample that defined the mm fundamental plane was initially collected to measure SMBH masses so all the galaxies are gas rich with regularly rotating CO disk which could introduce biases into the sample. If it is found that gas poor or disturbed systems do not follow the mm fundamental plane it could indicate a connection between the larger scale galaxy morphology and underlying accretion structure in AGN.

6.4 SYNTHESIS AND CONCLUDING REMARKS

In this thesis I have studied the AGN in nearby galaxies to study the connection between AGN and their host galaxies. In synthesis the results from this thesis show that there is a close connection between AGN and their host galaxy but many details of this connection are complicated and there are still many unanswered questions regarding this connection.

AGN may have the ability to impact the ISM in their host galaxies as can be seen in Chapter 2 where I showed that AGN may have the ability to cause molecular gas deficits and in Chapter 3 where it seems that AGN can excite both the low density and high density gas in the ISM. It is also not clear exactly how the AGN is impacted by the gas in their host galaxy. In Chapter 2 it seems that the large scale fuelling mechanism is different in different types of AGN whilst in Chapter 4 and Chapter 5 it seems that despite the larger scale fuelling mechanism the underlying nuclear structure and accretion mechanism may be the same. This thesis emphasises the need for further study in the fuelling/feedback picture and the underlying accretion mechanism in AGN.

Bibliography

Aird J., Coil A. L., Georgakakis A., Nandra K., Barro G., Pérez-González P. G., 2015, *MNRAS*, 451, 1892

Aird J., Coil A. L., Georgakakis A., 2018, *MNRAS*, 474, 1225

Alexander D. M., Hickox R. C., 2012, New Astronomy Reviews, 56, 93

Allen S. W., Dunn R. J. H., Fabian A. C., Taylor G. B., Reynolds C. S., 2006, *MNRAS*, 372, 21

Antonucci R., 1993, *ARAA*, 31, 473

Antonucci R. R. J., Miller J. S., 1985, *ApJ*, 297, 621

Astropy Collaboration et al., 2013, *A&A*, 558, A33

Astropy Collaboration et al., 2018, *AJ*, 156, 123

Astropy Collaboration et al., 2022, *ApJ*, 935, 167

Baan W. A., Henkel C., Loenen A. F., Baudry A., Wiklind T., 2008, *A&A*, 477, 747

Babyk I. V., McNamara B. R., Tamhane P. D., Nulsen P. E. J., Russell H. R., Edge A. C., 2019, *ApJ*, 887, 149

Bacon R., et al., 2010, in McLean I. S., Ramsay S. K., Takami H., eds, Society of Photo-Optical Instrumentation Engineers (SPIE) Conference Series Vol. 7735, Ground-based and Airborne Instrumentation for Astronomy III. p. 773508 (`arXiv:2211.16795`), doi:10.1117/12.856027

Bacon R., et al., 2014, The Messenger, 157, 13

Baldwin J. A., Phillips M. M., Terlevich R., 1981, *PASP*, 93, 5

Balmaverde B., Baldi R. D., Capetti A., 2008, *A&A*, 486, 119

Barvainis R., 1987, *ApJ*, 320, 537

Baugh C. M., 2006, Reports on Progress in Physics, 69, 3101

Baum W. A., 1959, *PASP*, 71, 106

Becker R. H., White R. L., Helfand D. J., 1994, in Crabtree D. R., Hanisch R. J., Barnes J., eds, Astronomical Society of the Pacific Conference Series Vol. 61, Astronomical Data Analysis Software and Systems III. p. 165

Beckmann V., Shrader C. R., 2012, Active Galactic Nuclei. John Wiley & Sons

Begelman M. C., Blandford R. D., Rees M. J., 1984, Reviews of Modern Physics, 56, 255

Behar E., Baldi R. D., Laor A., Horesh A., Stevens J., Tzioumis T., 2015, *MNRAS*, 451, 517

Behar E., Vogel S., Baldi R. D., Smith K. L., Mushotzky R. F., 2018, *MNRAS*, 478, 399

Behar E., et al., 2020, *MNRAS*, 491, 3523

Bell E. F., et al., 2004, *ApJ*, 608, 752

Bennert N., Falcke H., Shchekinov Y., Wilson A. S., 2004, in Storchi-Bergmann T., Ho L. C., Schmitt H. R., eds, IAU Symp Vol. 222, The Interplay Among Black Holes, Stars and ISM in Galactic Nuclei. pp 307–308 (`arXiv:astro-ph/0404278`), doi:10.1017/S1743921304002340

Bennert N., Jungwiert B., Komossa S., Haas M., Chini R., 2006, *A&A*, 459, 55

Benson A. J., 2010, *Phys. Repts.*, 495, 33

Bentz M. C., et al., 2013, *ApJ*, 767, 149

Bertram T., Eckart A., Fischer S., Zuther J., Straubmeier C., Wisotzki L., Krips M., 2007, *A&A*, 470, 571

Best P. N., Heckman T. M., 2012, *MNRAS*, 421, 1569

Best P. N., Kauffmann G., Heckman T. M., Brinchmann J., Charlot S., Ivezić Ž., White S. D. M., 2005, *MNRAS*, 362, 25

Bi S., Feng H., Ho L. C., 2020, *ApJ*, 900, 124

Bieri R., Dubois Y., Rosdahl J., Wagner A., Silk J., Mamon G. A., 2017, *MNRAS*, 464, 1854

Blandford R. D., 2001, Progress of Theoretical Physics Supplement, 143, 182

Blundell K. M., Fabian A. C., Crawford C. S., Erlund M. C., Celotti A., 2006, *ApJ*, 644, L13

Bohlin R. C., Savage B. D., Drake J. F., 1978, *ApJ*, 224, 132

Bolatto A. D., Wolfire M., Leroy A. K., 2013, *ARAA*, 51, 207

Bonatto C. J., Pastoriza M. G., 1997, *ApJ*, 486, 132

Bondi H., 1952, *MNRAS*, 112, 195

Bonning E. W., Cheng L., Shields G. A., Salviander S., Gebhardt K., 2007, *ApJ*, 659, 211

Boroson B., Kim D.-W., Fabbiano G., 2011, ApJ, 729, 12

Boselli A., Lequeux J., Gavazzi G., 2002, *Astrophys. Space Science*, 281, 127

Boselli A., Fossati M., Sun M., 2022, A&A Rev., 30, 3

Bower R. G., Benson A. J., Malbon R., Helly J. C., Frenk C. S., Baugh C. M., Cole S., Lacey C. G., 2006, *MNRAS*, 370, 645

Buttiglione S., Capetti A., Celotti A., Axon D. J., Chiaberge M., Macchetto F. D., Sparks W. B., 2009, *A&A*, 495, 1033

Cappellari M., 2013, *ApJ*, 778, L2

Cappellari M., et al., 2013a, MNRAS, 432, 1709

Cappellari M., et al., 2013b, *MNRAS*, 432, 1862

Cavagnolo K. W., McNamara B. R., Nulsen P. E. J., Carilli C. L., Jones C., Bîrzan L., 2010, *ApJ*, 720, 1066

Ciotti L., Ostriker J. P., 1997, *ApJ*, 487, L105

Clark C. J. R., Roman-Duval J. C., Gordon K. D., Bot C., Smith M. W. L., Hagen L. M. Z., 2023, *ApJ*, 946, 42

Clarke T. E., Blanton E. L., Sarazin C. L., Anderson L. D., Gopal-Krishna Douglass E. M., Kassim N. E., 2009, *ApJ*, 697, 1481

Combes F., 2001, in Funes J. G., Corsini E. M., eds, Astronomical Society of the Pacific Conference Series Vol. 230, Galaxy Disks and Disk Galaxies. pp 213–220 (`arXiv:astro-ph/0008341`), doi:10.48550/arXiv.astro-ph/0008341

Combes F., et al., 2013, *A&A*, 558, A124

Comrie A., et al., 2021, CARTA: Cube Analysis and Rendering Tool for Astronomy, Astrophysics Source Code Library, record ascl:2103.031

Condon J. J., Cotton W. D., Greisen E. W., Yin Q. F., Perley R. A., Taylor G. B., Broderick J. J., 1998, *AJ*, 115, 1693

Cook D. O., van Sistine A., Singer L., Kasliwal M. M., Kaplan D., Iptf Collaboration Growth Collaboration 2017, GRB Coordinates Network, 21707, 1

Crawford C. S., Allen S. W., Ebeling H., Edge A. C., Fabian A. C., 1999, *MNRAS*, 306, 857

Crocker R. M., Krumholz M. R., Thompson T. A., 2021, *MNRAS*, 503, 2651

Croton D. J., et al., 2006, *MNRAS*, 365, 11

Dame T. M., 2011, arXiv e-prints, p. arXiv:1101.1499

Davidson K., Netzer H., 1979, Reviews of Modern Physics, 51, 715

Davies R., Mark D., Sternberg A., 2012, *A&A*, 537, A133

Davis T. A., Bayet E., Crocker A., Topal S., Bureau M., 2013, *MNRAS*, 433, 1659

Davis T. A., Bureau M., Onishi K., Cappellari M., Iguchi S., Sarzi M., 2017, *MNRAS*, 468, 4675

Davis T. A., et al., 2018, *MNRAS*, 473, 3818

Davis T. A., et al., 2020, *MNRAS*, 496, 4061

Davis T. A., et al., 2022, *MNRAS*, 512, 1522

De Robertis M. M., Osterbrock D. E., 1986, *ApJ*, 301, 727

Delvecchio I., et al., 2014, *MNRAS*, 439, 2736

Di Matteo T., Springel V., Hernquist L., 2005, *Nature*, 433, 604

Dieter N. H., Goss W. M., 1966, Reviews of Modern Physics, 38, 256

Djorgovski S., Davis M., 1987, *ApJ*, 313, 59

Doi A., Inoue Y., 2016, *Pub. Astron. Soc. Japan*, 68, 56

Dressler A., 1980, *ApJ*, 236, 351

Dressler A., 1989, in Osterbrock D. E., Miller J. S., eds, IAU Symp Vol. 134, Active Galactic Nuclei. p. 217

Dressler A., Richstone D. O., 1988, *ApJ*, 324, 701

Eales S., et al., 2012, *ApJ*, 761, 168

Edge A. C., 2001, *MNRAS*, 328, 762

Edge A. C., Frayer D. T., 2003, *ApJ*, 594, L13

Eggen O. J., Lynden-Bell D., Sandage A. R., 1962, *ApJ*, 136, 748

Elford J. S., et al., 2024, *MNRAS*, 528, 319

Ellison S. L., Brown T., Catinella B., Cortese L., 2019, *MNRAS*, 482, 5694

Emsellem E., 2003, in Collin S., Combes F., Shlosman I., eds, Astronomical Society of the Pacific Conference Series Vol. 290, Active Galactic Nuclei: From Central Engine to Host Galaxy. p. 441

Emsellem E., 2004, in Storchi-Bergmann T., Ho L. C., Schmitt H. R., eds, Proc IAU Symp. Vol. 222, The Interplay Among Black Holes, Stars and ISM in Galactic Nuclei. pp 419–422 (`arXiv:astro-ph/0404475`), doi:10.1017/S1743921304002777

Esin A. A., McClintock J. E., Narayan R., 1997, *ApJ*, 489, 865

Esposito F., Vallini L., Pozzi F., Casasola V., Mingozzi M., Vignali C., Gruppioni C., Salvestrini F., 2022, *MNRAS*, 512, 686

Fabello S., Kauffmann G., Catinella B., Giovanelli R., Haynes M. P., Heckman T. M., Schiminovich D., 2011, *MNRAS*, 416, 1739

Fabian A. C., 1994, *ARAA*, 32, 277

Fabian A. C., 1999, *MNRAS*, 308, L39

Fabian A. C., 2012, *ARAA*, 50, 455

Falcke H., Körding E., Markoff S., 2004, A&A, 414, 895

Fanaroff B. L., Riley J. M., 1974, *MNRAS*, 167, 31P

Farrah D., et al., 2023, ApJ, 943, 133

Faustino Vieira H., Duarte-Cabral A., Davis T. A., Peretto N., Smith M. W. L., Querejeta M., Colombo D., Anderson M., 2024, *MNRAS*, 527, 3639

Fawcett V. A., Alexander D. M., Rosario D. J., Klindt L., Fotopoulou S., Lusso E., Morabito L. K., Calistro Rivera G., 2020, *MNRAS*, 494, 4802

Federrath C., Klessen R. S., 2012, *ApJ*, 761, 156

Federrath C., Klessen R. S., 2013, *ApJ*, 763, 51

Fender R. P., Hjellming R. M., Tilanus R. P. J., Pooley G. G., Deane J. R., Ogley R. N., Spencer R. E., 2001, *MNRAS*, 322, L23

Fender R. P., Belloni T. M., Gallo E., 2004, *MNRAS*, 355, 1105

Fernández-Ontiveros J. A., López-Gonzaga N., Prieto M. A., Acosta-Pulido J. A., Lopez-Rodriguez E., Asmus D., Tristram K. R. W., 2019, MNRAS, 485, 5377

Fernández-Ontiveros J. A., López-López X., Prieto A., 2023, A&A, 670, A22

Ferrarese L., Merritt D., 2000, *ApJ*, 539, L9

Fujita Y., Izumi T., Kawakatu N., Nagai H., Hirasawa R., Ikeda Y., 2023, *Pub. Astron. Soc. Japan*, 75, 925

Fujita Y., Izumi T., Nagai H., Kawakatu N., Kawanaka N., 2024, *ApJ*, 964, 29

Galeev A. A., Rosner R., Vaiana G. S., 1979, *ApJ*, 229, 318

Gao Y., Solomon P. M., 2004a, *ApJS*, 152, 63

Gao Y., Solomon P. M., 2004b, *ApJ*, 606, 271

García-Burillo S., et al., 2014, *A&A*, 567, A125

García-Burillo S., et al., 2021, *A&A*, 652, A98

Gaspari M., Ruszkowski M., Oh S. P., 2013, *MNRAS*, 432, 3401

Gaspari M., Brighenti F., Temi P., 2015, *A&A*, 579, A62

Gaspari M., Temi P., Brighenti F., 2017, *MNRAS*, 466, 677

Gebhardt K., et al., 2000, *ApJ*, 539, L13

Girdhar A., et al., 2022, *MNRAS*, 512, 1608

Gleisinger R. C., O'Dea C. P., Gallimore J. F., Wykes S., Baum S. A., 2020, *ApJ*, 905, 42

Granato G. L., De Zotti G., Silva L., Bressan A., Danese L., 2004, *ApJ*, 600, 580

Greene J. E., Ho L. C., Barth A. J., 2008, *ApJ*, 688, 159

Greene J. E., et al., 2010, *ApJ*, 721, 26

Grimm H. J., Gilfanov M., Sunyaev R., 2003, *MNRAS*, 339, 793

Gültekin K., et al., 2009, *ApJ*, 698, 198

Gültekin K., King A. L., Cackett E. M., Nyland K., Miller J. M., Di Matteo T., Markoff S., Rupen M. P., 2019, ApJ, 871, 80

Gunn J. E., Gott J. Richard I., 1972, *ApJ*, 176, 1

Haardt F., Maraschi L., 1993, *ApJ*, 413, 507

Hardcastle M. J., Evans D. A., Croston J. H., 2007, *MNRAS*, 376, 1849

Häring N., Rix H.-W., 2004, *ApJ*, 604, L89

Harris C. R., et al., 2020, Nature, 585, 357

Harrison C. M. C., 2014, PhD thesis, Durham University, UK

Hawkins M. R. S., 2007, *A&A*, 462, 581

Haynes M. P., Giovanelli R., Chincarini G. L., 1984, *ARAA*, 22, 445

Heckman T. M., Best P. N., 2014, *ARAA*, 52, 589

Heckman T. M., Kauffmann G., Brinchmann J., Charlot S., Tremonti C., White S. D. M., 2004, *ApJ*, 613, 109

Heinis S., et al., 2016, *ApJ*, 826, 62

Henriques B. M. B., White S. D. M., Thomas P. A., Angulo R., Guo Q., Lemson G., Springel V., Overzier R., 2015, *MNRAS*, 451, 2663

Hildebrand R. H., 1983, *Quarterly Journal of the Royal Astronomical Society*, 24, 267

Ho L. C., 2008, *ARAA*, 46, 475

Ho L. C., Filippenko A. V., Sargent W. L., 1995, *ApJS*, 98, 477

Ho L. C., Darling J., Greene J. E., 2008, *ApJ*, 681, 128

Hopkins P. F., Hernquist L., Cox T. J., Di Matteo T., Robertson B., Springel V., 2006, *ApJS*, 163, 1

Hoyle F., 1953, *ApJ*, 118, 513

Hu J., 2008, *MNRAS*, 386, 2242

Hubble E. P., 1926, *ApJ*, 64, 321

Hunter J. D., 2007, Computing in Science & Engineering, 9, 90

Husemann B., et al., 2017, The Messenger, 169, 42

Husemann B., et al., 2019, *A&A*, 627, A53

Husemann B., et al., 2022, *A&A*, 659, A124

Imanishi M., Nakanishi K., Tamura Y., Oi N., Kohno K., 2007, *AJ*, 134, 2366

Imanishi M., et al., 2020, *ApJ*, 902, 99

Inoue Y., Doi A., 2018, *ApJ*, 869, 114

Izumi T., et al., 2013, *Pub. Astron. Soc. Japan*, 65, 100

Izumi T., et al., 2016a, *ApJ*, 818, 42

Izumi T., Kawakatu N., Kohno K., 2016b, *ApJ*, 827, 81

Jackson J. M., Paglione T. A. D., Ishizuki S., Nguyen-Q-Rieu 1993, *ApJ*, 418, L13

Jarrett T. H., Chester T., Cutri R., Schneider S. E., Huchra J. P., 2003, *AJ*, 125, 525

Jeans J. H., 1902, Philosophical Transactions of the Royal Society of London Series A, 199, 1

Jiang Y.-F., Ciotti L., Ostriker J. P., Spitkovsky A., 2010, *ApJ*, 711, 125

Jiménez-Donaire M. J., et al., 2019, *ApJ*, 880, 127

Juneau S., Narayanan D. T., Moustakas J., Shirley Y. L., Bussmann R. S., Kennicutt R. C. J., Vanden Bout P. A., 2009, *ApJ*, 707, 1217

Kaspi S., Smith P. S., Netzer H., Maoz D., Jannuzi B. T., Giveon U., 2000, *ApJ*, 533, 631

Kaspi S., Maoz D., Netzer H., Peterson B. M., Vestergaard M., Jannuzi B. T., 2005, *ApJ*, 629, 61

Kauffmann G., Haehnelt M., 2000, *MNRAS*, 311, 576

Kauffmann G., et al., 2003, *MNRAS*, 346, 1055

Kauffmann G., White S. D. M., Heckman T. M., Ménard B., Brinchmann J., Charlot S., Tremonti C., Brinkmann J., 2004, *MNRAS*, 353, 713

Kawamuro T., et al., 2022, *ApJ*, 938, 87

Kennicutt Robert C. J., 1989, *ApJ*, 344, 685

Kennicutt Robert C. J., 1998, *ARAA*, 36, 189

Kewley L. J., Dopita M. A., Sutherland R. S., Heisler C. A., Trevena J., 2001, *ApJ*, 556, 121

Kewley L. J., Groves B., Kauffmann G., Heckman T., 2006, *MNRAS*, 372, 961

Kim D.-W., Fabbiano G., 2004, *ApJ*, 611, 846

King A., 2003, *ApJ*, 596, L27

King A., Nixon C., 2015, *MNRAS*, 453, L46

King A. R., Pringle J. E., 2007, *MNRAS*, 377, L25

Kishimoto M., Hönig S. F., Beckert T., Weigelt G., 2007, *A&A*, 476, 713

Koay J. Y., Vestergaard M., Casasola V., Lawther D., Peterson B. M., 2016, *MNRAS*, 455, 2745

Kohno K., 2005, in Hüttmeister S., Manthey E., Bomans D., Weis K., eds, American Institute of Physics Conference Series Vol. 783, The Evolution of Starbursts. pp 203–208 (`arXiv:astro-ph/0508420`), doi:10.1063/1.2034987

Kohno K., Matsushita S., Vila-Vilaró B., Okumura S. K., Shibatsuka T., Okiura M., Ishizuki S., Kawabe R., 2001, in Knapen J. H., Beckman J. E., Shlosman I., Mahoney T. J., eds, Astronomical Society of the Pacific Conference Series Vol. 249, The Central Kiloparsec of Starbursts and AGN: The La Palma Connection. p. 672 (`arXiv:astro-ph/0206398`), doi:10.48550/arXiv.astro-ph/0206398

Komissarov S. S., Gubanov A. G., 1994, *A&A*, 285, 27

Kormendy J., 1979, *ApJ*, 227, 714

Kormendy J., 1993, in Beckmann J. Colina L., Netzer P., eds, The Nearest Active Galaxies.

Kormendy J., 2013, in Falcón-Barroso J., Knapen J. H., eds, , Secular Evolution of Galaxies. Cambridge University Press, p. 1, doi:10.48550/arXiv.1311.2609

Kormendy J., Gebhardt K., 2001, in Wheeler J. C., Martel H., eds, American Institute of Physics Conference Series Vol. 586, 20th Texas Symposium on relativistic astrophysics. AIP, pp 363–381 (`arXiv:astro-ph/0105230`), doi:10.1063/1.1419581

Kormendy J., Ho L. C., 2013, *ARAA*, 51, 511

Kormendy J., Kennicutt Robert C. J., 2004, *ARAA*, 42, 603

Kormendy J., Bender R., Cornell M. E., 2011, *Nature*, 469, 374

Koss M., et al., 2017, ApJ, 850, 74

Koss M. J., et al., 2021, *ApJS*, 252, 29

Koss M. J., et al., 2022, ApJS, 261, 2

Krips M., Neri R., García-Burillo S., Martín S., Combes F., Graciá-Carpio J., Eckart A., 2008, *ApJ*, 677, 262

LaMassa S. M., et al., 2015, *ApJ*, 800, 144

Laing R. A., Bridle A. H., 2013, *MNRAS*, 432, 1114

Laing R. A., Jenkins C. R., Wall J. V., Unger S. W., 1994, in Bicknell G. V., Dopita M. A., Quinn P. J., eds, Astronomical Society of the Pacific Conference Series Vol. 54, The Physics of Active Galaxies. p. 201

Larson R. B., 1975, *MNRAS*, 173, 671

Lelli F., McGaugh S. S., Schombert J. M., 2016, *ApJ*, 816, L14

Lelli F., McGaugh S. S., Schombert J. M., Desmond H., Katz H., 2019, *MNRAS*, 484, 3267

Lelli F., Davis T. A., Bureau M., Cappellari M., Liu L., Ruffa I., Smith M. D., Williams T. G., 2022, *MNRAS*, 516, 4066

Leroy A. K., Walter F., Brinks E., Bigiel F., de Blok W. J. G., Madore B., Thornley M. D., 2008, *AJ*, 136, 2782

Leroy A. K., et al., 2011, *ApJ*, 737, 12

Leroy A. K., et al., 2019, *ApJS*, 244, 24

Leroy A. K., et al., 2022, *ApJ*, 927, 149

Levesque E. M., Kewley L. J., Larson K. L., 2010, *AJ*, 139, 712

Li F., et al., 2021, *MNRAS*, 503, 4508

Liu Y., Jiang D. R., Gu M. F., 2006, *ApJ*, 637, 669

Lucchini M., et al., 2022, *MNRAS*, 517, 5853

Maccagni F. M., et al., 2023, *A&A*, 675, A59

Madau P., Dickinson M., 2014, *ARAA*, 52, 415

Magorrian J., et al., 1998, *AJ*, 115, 2285

Mahadevan R., 1997, ApJ, 477, 585

Malkan M. A., Sargent W. L. W., 1982, *ApJ*, 254, 22

Maraschi L., Ghisellini G., Celotti A., 1992, *ApJ*, 397, L5

Marconi A., Hunt L. K., 2003, *ApJ*, 589, L21

Marconi A., Risaliti G., Gilli R., Hunt L. K., Maiolino R., Salvati M., 2004, MNRAS, 351, 169

Martig M., Bournaud F., Teyssier R., Dekel A., 2009, *ApJ*, 707, 250

Martini P., 2004, in Storchi-Bergmann T., Ho L. C., Schmitt H. R., eds, Proc IAU Symp. Vol. 222, The Interplay Among Black Holes, Stars and ISM in Galactic Nuclei. pp 235–241 (`arXiv:astro-ph/0404426`), doi:10.1017/S1743921304002170

Martini P., Regan M. W., Mulchaey J. S., Pogge R. W., 2003, *ApJ*, 589, 774

Masters K. L., et al., 2019, *MNRAS*, 487, 1808

McConnell N. J., Ma C.-P., 2013, *ApJ*, 764, 184

McKee C. F., Ostriker J. P., 1977, *ApJ*, 218, 148

McKinney J., Hayward C. C., Rosenthal L. J., Martínez-Galarza J. R., Pope A., Sajina A., Smith H. A., 2021, *ApJ*, 921, 55

McLure R. J., Dunlop J. S., 2002, *MNRAS*, 331, 795

McMullin J. P., Waters B., Schiebel D., Young W., Golap K., 2007, in Shaw R. A., Hill F., Bell D. J., eds, Astronomical Society of the Pacific Conference Series Vol. 376, Astronomical Data Analysis Software and Systems XVI. p. 127

McNamara B. R., Nulsen P. E. J., 2007, *ARAA*, 45, 117

McNamara B. R., Nulsen P. E. J., 2012, New Journal of Physics, 14, 055023

McNamara B. R., Nulsen P. E. J., Wise M. W., Rafferty D. A., Carilli C., Sarazin C. L., Blanton E. L., 2005, *Nature*, 433, 45

McNamara B. R., Russell H. R., Nulsen P. E. J., Hogan M. T., Fabian A. C., Pulido F., Edge A. C., 2016, *ApJ*, 830, 79

Meenakshi M., Mukherjee D., Wagner A. Y., Nesvadba N. P. H., Morganti R., Janssen R. M. J., Bicknell G. V., 2022, *MNRAS*, 511, 1622

Merloni A., Heinz S., 2008, *MNRAS*, 388, 1011

Merloni A., Heinz S., di Matteo T., 2003, MNRAS, 345, 1057

Merloni A., et al., 2010, *ApJ*, 708, 137

Molina J., Shangguan J., Wang R., Ho L. C., Bauer F. E., Treister E., 2023, *ApJ*, 950, 60

Moore B., Katz N., Lake G., Dressler A., Oemler A., 1996, *Nature*, 379, 613

Moser L., et al., 2016, *A&A*, 587, A137

Moustakas J., Kennicutt Robert C. J., Tremonti C. A., Dale D. A., Smith J.-D. T., Calzetti D., 2010, *ApJS*, 190, 233

Muñoz-Mateos J. C., et al., 2009, *ApJ*, 701, 1965

Murphy E. J., et al., 2011, *ApJ*, 737, 67

Nagao T., Maiolino R., Marconi A., 2006, *A&A*, 459, 85

Namekata D., Umemura M., Hasegawa K., 2014, *MNRAS*, 443, 2018

Narayan R., Yi I., 1995a, ApJ, 444, 231

Narayan R., Yi I., 1995b, *ApJ*, 452, 710

Nayakshin S., Power C., King A. R., 2012, *ApJ*, 753, 15

Negri A., Posacki S., Pellegrini S., Ciotti L., 2014, MNRAS, 445, 1351

Nenkova M., Sirocky M. M., Ivezić Ž., Elitzur M., 2008, *ApJ*, 685, 147

Netzer H., Trakhtenbrot B., 2014, *MNRAS*, 438, 672

Nims J., Quataert E., Faucher-Giguère C.-A., 2015, *MNRAS*, 447, 3612

North E. V., et al., 2019, *MNRAS*, 490, 319

North E. V., et al., 2021, *MNRAS*, 503, 5179

O'Dea C. P., Saikia D. J., 2020, arXiv e-prints, p. arXiv:2009.02750

Ocaña Flaquer B., Leon S., Combes F., Lim J., 2010, *A&A*, 518, A9

Oemler Augustus J., 1974, *ApJ*, 194, 1

Onishi K., Iguchi S., Davis T. A., Bureau M., Cappellari M., Sarzi M., Blitz L., 2017, *MNRAS*, 468, 4663

Oosterloo T., Raymond Oonk J. B., Morganti R., Combes F., Dasyra K., Salomé P., Vlahakis N., Tadhunter C., 2017, *A&A*, 608, A38

Panessa F., Baldi R. D., Laor A., Padovani P., Behar E., McHardy I., 2019, Nature Astronomy, 3, 387

Papastergis E., Giovanelli R., Haynes M. P., Rodríguez-Puebla A., Jones M. G., 2013, *ApJ*, 776, 43

Partridge R. B., Peebles P. J. E., 1967, *ApJ*, 147, 868

Paulino-Afonso A., et al., 2019, *A&A*, 630, A57

Pedregosa F., et al., 2011, Journal of Machine Learning Research, 12, 2825

Peng Y., Maiolino R., Cochrane R., 2015, *Nature*, 521, 192

Pesce D. W., et al., 2021, *ApJ*, 923, 260

Peterson B. M., 1993, *PASP*, 105, 247

Peterson B. M., et al., 2004, *ApJ*, 613, 682

Peterson B. M., et al., 2013, *ApJ*, 779, 109

Pfenniger D., Norman C., 1990, *ApJ*, 363, 391

Pier E. A., Krolik J. H., 1992, *ApJ*, 401, 99

Pizzolato F., Soker N., 2005, *ApJ*, 632, 821

Pizzolato F., Soker N., 2010, *MNRAS*, 408, 961

Plotkin R. M., Markoff S., Kelly B. C., Körding E., Anderson S. F., 2012, MNRAS, 419, 267

Prandini E., Ghisellini G., 2022, Galaxies, 10, 35

Prandoni I., Laing R. A., de Ruiter H. R., Parma P., 2010, *A&A*, 523, A38

Prieto M. A., Fernández-Ontiveros J. A., Markoff S., Espada D., González-Martín O., 2016, MNRAS, 457, 3801

Reeves J. N., Turner M. J. L., 2000, *MNRAS*, 316, 234

Rémy-Ruyer A., et al., 2014, *A&A*, 563, A31

Reynolds R. J., 1984, *ApJ*, 282, 191

Reynolds C. S., Di Matteo T., Fabian A. C., Hwang U., Canizares C. R., 1996, *MNRAS*, 283, L111

Ricci C., et al., 2023, arXiv e-prints, p. arXiv:2306.04679

Rodríguez-Ardila A., Pastoriza M. G., Donzelli C. J., 2000, *ApJS*, 126, 63

Roman-Duval J., Bot C., Chastenet J., Gordon K., 2017, *ApJ*, 841, 72

Roman-Duval J., et al., 2022, *ApJ*, 928, 90

Roos O., Juneau S., Bournaud F., Gabor J. M., 2015, *ApJ*, 800, 19

Rosario D. J., et al., 2013, *ApJ*, 771, 63

Rosario D. J., et al., 2018, *MNRAS*, 473, 5658

Rousseeuw P. J., 1984, Journal of the American Statistical Association., 79

Ruffa I., Vignali C., Mignano A., Paladino R., Iwasawa K., 2018, *A&A*, 616, A127

Ruffa I., et al., 2019a, *MNRAS*, 484, 4239

Ruffa I., et al., 2019b, *MNRAS*, 489, 3739

Ruffa I., Laing R. A., Prandoni I., Paladino R., Parma P., Davis T. A., Bureau M., 2020, *MNRAS*, 499, 5719

Ruffa I., Prandoni I., Davis T. A., Laing R. A., Paladino R., Casasola V., Parma P., Bureau M., 2022, *MNRAS*, 510, 4485

Ruffa I., et al., 2023, *MNRAS*, 522, 6170

Ruffa I., et al., 2024, *MNRAS*, 528, L76

Saikia P., Körding E., Falcke H., 2015, *MNRAS*, 450, 2317

Saintonge A., Catinella B., 2022, *ARAA*, 60, 319

Saintonge A., et al., 2011a, *MNRAS*, 415, 32

Saintonge A., et al., 2011b, *MNRAS*, 415, 61

Saintonge A., et al., 2017, *ApJS*, 233, 22

Sánchez S. F., et al., 2015, *A&A*, 574, A47

Sanders D. B., Soifer B. T., Elias J. H., Madore B. F., Matthews K., Neugebauer G., Scoville N. Z., 1988, *ApJ*, 325, 74

Sandstrom K. M., et al., 2013, *ApJ*, 777, 5

Sani E., Marconi A., Hunt L. K., Risaliti G., 2011, *MNRAS*, 413, 1479

Schawinski K., Thomas D., Sarzi M., Maraston C., Kaviraj S., Joo S.-J., Yi S. K., Silk J., 2007, *MNRAS*, 382, 1415

Schmidt M., 1959, *ApJ*, 129, 243

Schmidt M., 1963, *Nature*, 197, 1040

Serra P., et al., 2012, *MNRAS*, 422, 1835

Seth A. C., et al., 2010, *ApJ*, 714, 713

Shakura N. I., Sunyaev R. A., 1973, *A&A*, 24, 337

Shankar F., Salucci P., Granato G. L., De Zotti G., Danese L., 2004, *MNRAS*, 354, 1020

Shi Y., Rieke G. H., Smith P., Rigby J., Hines D., Donley J., Schmidt G., Diamond-Stanic A. M., 2010, *ApJ*, 714, 115

Shields G. A., 1978, *Nature*, 272, 706

Shlosman I., Frank J., Begelman M. C., 1989, *Nature*, 338, 45

Silk J., Rees M. J., 1998, *A&A*, 331, L1

Smirnova-Pinchukova I., et al., 2022, *A&A*, 659, A125

Smith M. W. L., et al., 2012, *ApJ*, 756, 40

Smith M. D., et al., 2019, *MNRAS*, 485, 4359

Smith M. D., et al., 2021a, *MNRAS*, 500, 1933

Smith M. D., et al., 2021b, *MNRAS*, 503, 5984

Sobolewska M. A., Siemiginowska A., Życki P. T., 2004, *ApJ*, 617, 102

Soltan A., 1982, *MNRAS*, 200, 115

Somerville R. S., Hopkins P. F., Cox T. J., Robertson B. E., Hernquist L., 2008, *MNRAS*, 391, 481

Somerville R. S., Gilmore R. C., Primack J. R., Domínguez A., 2012, *MNRAS*, 423, 1992

Spitzer Lyman J., 1968, in Middlehurst B. M., Aller L. H., eds, , Nebulae and Interstellar Matter. Princeton University, p. 1

Stalevski M., Fritz J., Baes M., Nakos T., Popović L. Č., 2012, *MNRAS*, 420, 2756

Stalevski M., Ricci C., Ueda Y., Lira P., Fritz J., Baes M., 2016, MNRAS, 458, 2288

Stasińska G., Cid Fernandes R., Mateus A., Sodré L., Asari N. V., 2006, *MNRAS*, 371, 972

Steinmetz M., Navarro J. F., 2002, New A, 7, 155

Stemo A., Comerford J. M., Barrows R. S., Stern D., Assef R. J., Griffith R. L., 2020, *ApJ*, 888, 78

Sternberg A., Genzel R., Tacconi L., 1994, *ApJ*, 436, L131

Strateva I., et al., 2001, *AJ*, 122, 1861

Strong A. W., et al., 1988, *A&A*, 207, 1

Sun W.-H., Malkan M. A., 1989, *ApJ*, 346, 68

Suzuki T. L., et al., 2016, *MNRAS*, 462, 181

Symeonidis M., 2022, MNRAS, 509, 3209

Tacconi L. J., Genzel R., Blietz M., Cameron M., Harris A. I., Madden S., 1994, *ApJ*, 426, L77

Tadhunter C. N., Morganti R., di Serego Alighieri S., Fosbury R. A. E., Danziger I. J., 1993, *MNRAS*, 263, 999

Tan Q.-H., et al., 2018, *ApJ*, 860, 165

Toomre A., 1977, in Tinsley B. M., Larson Richard B. Gehret D. C., eds, Evolution of Galaxies and Stellar Populations. p. 401

Tremou E., et al., 2020, *MNRAS*, 493, L132

Urry C. M., Padovani P., 1995, *PASP*, 107, 803

Usero A., García-Burillo S., Fuente A., Martín-Pintado J., Rodríguez-Fernández N. J., 2004, *A&A*, 419, 897

Vaona L., Ciroi S., Di Mille F., Cracco V., La Mura G., Rafanelli P., 2012, *MNRAS*, 427, 1266

Veale M., Ma C.-P., Greene J. E., Thomas J., Blakeslee J. P., McConnell N., Walsh J. L., Ito J., 2017, *MNRAS*, 471, 1428

Veilleux S., Osterbrock D. E., 1987, *ApJS*, 63, 295

Virtanen P., et al., 2020, Nature Methods, 17, 261

Wada K., Papadopoulos P. P., Spaans M., 2009, *ApJ*, 702, 63

Wagner A. Y., Bicknell G. V., Umemura M., 2012, *ApJ*, 757, 136

Ward S. R., Harrison C. M., Costa T., Mainieri V., 2022, *MNRAS*, 514, 2936

Wes McKinney 2010, in Stéfan van der Walt Jarrod Millman eds, Proceedings of the 9th Python in Science Conference. pp 56 – 61, doi:10.25080/Majora-92bf1922-00a

White S. D. M., Rees M. J., 1978, *MNRAS*, 183, 341

Williams J. K., Gliozzi M., Bockwoldt K. A., Shuvo O. I., 2023, MNRAS, 521, 2897

Wilson A. S., Braatz J. A., Heckman T. M., Krolik J. H., Miley G. K., 1993, *ApJ*, 419, L61

Wisotzki L., Christlieb N., Bade N., Beckmann V., Köhler T., Vanelle C., Reimers D., 2000, *A&A*, 358, 77

Wolfire M. G., McKee C. F., Hollenbach D., Tielens A. G. G. M., 2003, *ApJ*, 587, 278

Wu Q., Feng J., Fan X., 2018, *ApJ*, 855, 46

Yang G., et al., 2020, MNRAS, 491, 740

York D. G., et al., 2000, *AJ*, 120, 1579

Zabel N., et al., 2019, *MNRAS*, 483, 2251

Zhang Z.-Y., Gao Y., Henkel C., Zhao Y., Wang J., Menten K. M., Güsten R., 2014, *ApJ*, 784, L31

Zhu G., Zaw I., Blanton M. R., Greenhill L. J., 2011, *ApJ*, 742, 73

pandas development team T., 2020, pandas-dev/pandas: Pandas, doi:10.5281/zenodo.3509134, `https://doi.org/10.5281/zenodo.3509134`

van den Bosch R. C. E., 2016, ApJ, 831, 134